Optical Satellite Networks Performance: Channel Modeling, Mitigation Techniques & Optimization

PhD Thesis

Nikolaos K. Lyras

Electrical & Computer Engineer, NTUA

05/07/2019

Athens, Greece

Επίδοση Οπτικών Δορυφορικών Δικτύων: Μοντελοποίηση Διαύλου, Τεχνικές Άμβλυνσης Διαλείψεων & Βελτιστοποίηση

Διδακτορική Διατριβή

Νικόλαος Κ. Λύρας

Ηλεκτρολόγος Μηχανικός & Μηχανικός Υπολογιστών

ΕΜΠ

Επιβλέπων: Αθανάσιος Δ. Παναγόπουλος

Αναπληρωτής Καθηγητής, ΕΜΠ

05/07/2019

Αθήνα, Ελλάδα

Επίδοση Οπτικών Δορυφορικών Δικτύων: Μοντελοποίηση Διαύλου, Τεχνικές Άμβλυνσης Διαλείψεων & Βελτιστοποίηση

Διδακτορική Διατριβή

Νικόλαος Κ. Λύρας

Τριμελής Συμβουλευτική :   Αθανάσιος Δ. Παναγόπουλος
Επιτροπή   Παναγιώτης Κωττής

                                                Γεώργιος Φικιώρης

Επιτροπή Εξέτασης		
....	....	....
Α. Δ. Παναγόπουλος **Αν. Καθηγητής, ΕΜΠ**	**Π. Κωττής** **Καθηγητής, ΕΜΠ**	**Γ. Φικιώρης** **Καθηγητής, ΕΜΠ**
....	....	....
Ι.Α. Ρουμελιώτης **Καθηγητής, ΕΜΠ**	**Χ. Καψάλης** **Καθηγητής, ΕΜΠ**	**Η. Αβραμόπουλος** **Καθηγητής, ΕΜΠ**
	....	
	Ε. Νισταζάκης **Αν. Καθηγητής, ΕΚΠΑ**	

05/07/2019

Αθήνα, Ελλάδα

Table of Contents

Table of Tables

Table of Figures

Πίνακας Σχημάτων

Γλωσσάριο

Αγγλικά	Ελληνικά
Adaptive Optics	Προσαρμοστικά οπτικά συστήματα
Aperture averaging factor	Παράγοντας μέσης λήψης σήματος
Beam	Δέσμη
Beam Spreading	Εξάπλωση σήματος
Beam wander	Απόκλιση του κέντρου της οπτικής δέσμης
Bit error rate	Ρυθμός λανθασμένων bit
Capacity	Χωρητικότητα
Clouds	Σύννεφα
Cloud free line of sight	Διάδοση οπτικού σήματος χωρίς νέφη
Code rate	Ρυθμός κωδικοποίησης
Cumulative distribution function	Αθροιστική συνάρτηση κατανομής
Data rate	Ρυθμός δεδομένων
Deep Space	Βαθύ Διάστημα
Diffraction	Περίθλαση
Downlink	Κατερχόμενη ζεύξη
Elevation angle	Γωνία ανυψωσης
GEO Satellite	Γεωστατικός Δορυφόρος
Ice clouds	Σύννεφα πάγου
Integrated liquid water content	Κάθετο ολοκήρωμα της περιεκτικότητας σε υγρό νερό των νεφών
Intensity modulation	Σχήμα διαμόρφωσης έντασης
Irradiance	Ακτινοβολία
Link budget	Προϋπολογισμός ισχύος
LEO satellite	Δορυφόρος χαμηλής τροχιάς
Liquid water content	Περιεκτικότητα σε υγρό νερό των νεφών
Lognormal distribution	Λογαριθμοκανονική κατανομή
MEO satellite	Δορυφόρος μέσης τροχιάς
Mitigation Techniques	Τεχνικές άμβλυνσης διαλείψεων
Modulation	Διαμόρφωση
Normal distribution	Κανονική κατανομή
Obscuration	Σκίαση
Optical ground station	Οπτικός σταθμός βάσης
Power	Ισχύς
Pointing error	Σφάλμα Στόχευσης
Probability	Πιθανότητα
Probability density function	Συνάρτηση πυκνότητας πιθανότητας
Propagation	Διάδοση
Pulse position modulation	Διαμόρφωση θέσης παλμού
Receiver	Δέκτης
Refractive index	Δείκτης διάθλασης της ατμόσφαιρας
Satellite	Δορυφόρος
Scintillation	Σπινθηρισμός
Scintillation index	Δείκτης σπινθηρισμού
Serial concatenated convolutional codes	Σειριακοί συνελικτικοί κώδικες
Single photon counting detectors	Ανιχνευτές μέτρησης μεμονωμένων φωτονίων
Slant path	Κεκλιμένος δρόμος διάδοσης

Spatial correlation	Χωρική συσχέτιση
Spatial diversity	Διαφορισμός θέσης
Spectrum	Φάσμα
Stochastic differential equations	Στοχαστικές διαφορικές εξισώσεις
Symbol error rate	Ρυθμός λανθασμένων συμβόλων
Temporal correlation	Χρονική συσχέτιση
Time series	Χρονοσειρές
Transmitter	Πομπός
Transmitter diversity	Διαφορισμός πομπού
Turbulence	Στροβιλισμός
Uplink	Ανερχόμενη ζεύξη
Water clouds	Σύννεφα νερού

Abstract

The scope of this Thesis is the study of satellite communication systems operating at optical frequencies and the development of accurate channel models required for the reliable design and evaluation of the performance of these systems. The growing developments in information and telecommunication technology have led to the everyday increasing usage of high speed internet and multimedia applications, revealing the demand for higher data rates and larger bandwidth. To satisfy these demands, the new designed high throughput satellite communication systems are shifting to higher frequency bands for both Near Earth and Deep Space satellite (for distances greater than Moon) communication systems. A promising solution is the utilization of optical frequencies for satellite communication systems. Free space optical (FSO) satellite communication systems exhibit a great variety of advantages compared to RF satellite systems like the higher data rates, the more spectral bandwidth, the less power consumption, mass and size and the improved security among others.

However, when optical beam propagates through the earth's atmosphere it is mainly affected, but not limited to, by atmospheric turbulence and clouds. Cloud coverage is the dominant prohibitive phenomenon for the operation of optical satellite communication systems. The induced attenuation due to clouds causes the blockage of the link with the presence of clouds. On the other hand, for cloud free line of sight (CFLOS) conditions (no clouds) atmospheric turbulence contains the key attenuation factor. For the mitigation of these phenomena several fade mitigation techniques have been proposed. This Thesis is mostly concentrated on the modeling of cloud coverage and atmospheric turbulence for optical satellite communication links and the mitigation of these phenomena.

Firstly in the first Chapter a state of the art review of optical satellite communication systems is reported. Additionally, a variety of experimental measurement campaigns that have so far been conducted are briefly exhibited. In the second Chapter the propagation phenomena that affect the optical beam are presented and a review of the propagation models is exhibited. In addition, the proposed fade mitigation techniques for each propagation phenomenon are reported.

The Chapters three four and five are devoted to the methodologies developed at the framework of this Thesis for modelling of cloud coverage and cloud attenuation. To begin with, it is described in this Thesis that cloud coverage can be modelled employing Integrated Liquid Water Content (ILWC) statistics while ILWC can be modeled according to lognormal distribution.

In Chapter 3, a methodology for the generation of 2 and 3 Dimensions ILWC time series correlated both on temporal and on spatial domains is proposed. The proposed methodology employs multi-dimensional stochastic differential equations (SDEs) for the time series synthesis and incorporates the temporal and spatial behaviour of ILWC. Additionally, the 3D ILWC space time synthesizer incorporates the vertical extent of clouds.

In Chapter 4, the 2D and 3D synthesizers proposed in Chapter 3 are employed for the estimation of cloud attenuation and cloud free line of sight (CFLOS) probability for single and joint slant paths. Clouds are classified based on the cloud vertical extent and using the microphysical properties of clouds and the well-known Mie scattering theory, a unified space-time model for the prediction of induced attenuation due to clouds for frequencies above Ka [26.5-40 GHz] band up to optical range is presented. To continue, assuming an on/off channel with cloud occurrence a methodology for the generation of CFLOS time series correlated on temporal and spatial domain for both single and joint slant paths is presented. Both synthesizers take into account the elevation angle and the altitude of the station (for high altitude stations) for the estimation of cloud attenuation and CFLOS respectively and are employed for both GEO satellite communication systems and non-GEO satellites i.e. with time dependent elevation angles as space segment. Finally the space time CFLOS generator is employed in order valuable statistics from the system point of view for an OGS network (OGSN), like the average number of OGS switches etc. are derived.

In Chapter 5, a simple physical and mathematical theoretical model for the prediction of CFLOS probability along a single slant path and for separated on spatial domain multiple optical satellite links is presented. For the accurate evaluation of CFLOS the elevation angle of the slant path, the altitude of ground stations and the spatial variability of clouds are considered. In addition, CFLOS probability for simultaneously available optical links for the application of spatial multiplexing transmission techniques is estimated.

The Chapter 6 of this Thesis is devoted on the development of novel optimization algorithms for the selection of OGSs forming an OGSN for mitigation of cloud coverage. These algorithms are aware of the clouds monthly variability and take advantage of the hemisphere differences. Additionally, in this chapter it is proved that ILWC monthly statistics can be sufficiently described by lognormal distribution. Moreover, the methodologies developed in Chapters 4 and 5 are transformed in order the monthly and hemisphere variations of ILWC are incorporated. Finally, an optimization algorithm for the identification of active stations per month in an OGSN is also proposed.

The Chapter 7 is concentrated on modeling of turbulence effects under CFLOS conditions for optical satellite communications. In this chapter a methodology for the estimation of aperture averaging factor for a central obscured aperture is presented. Additionally, a unified methodology for the generation of received irradiance/power time series for an optical uplink GEO satellite feeder link is presented. The proposed methodology takes into account the turbulence and miss-pointing effects among others, while it benefits of the use of Stochastic Differential Equations (SDEs) for the incorporation of the scintillation effects. For the validation of the methodologies proposed in this chapter measurements from the ARTEMIS bi-directional optical satellite link campaign are used.

The Chapter 8 of this Thesis is devoted to the design of a deep space optical link. In this chapter a tool for the estimation of the link budget for deep space missions based on the CCSDS (Consultative

Committee for Space Data Systems) standards is presented. The main elements that are taken into account in the deep space link budget tool are exhibited. Additionally, a practical methodology, for the selection of the main signalling parameters (modulation order, code rate, slot width) without resorting to lengthy coded Bit Error Rate (BER) evaluations is presented. Finally, employing the proposed tool a sensitivity analysis of various hypothetical deep space missions is presented.

In the last Chapter of this Thesis some general and interesting conclusions are drawn and presented and finally some ideas for future work based on the models and the results of this Thesis are presented.

Περίληψη

Η παρούσα Διατριβή επικεντρώνεται στη μελέτη των δορυφορικών συστημάτων επικοινωνιών που λειτουργούν στο φάσμα των οπτικών συχνοτήτων. Πιο συγκεκριμένα, ασχολείται με την μοντελοποίηση του οπτικού διαύλου η οποία απαιτείται για τον αξιόπιστο σχεδιασμό και την αξιολόγηση της απόδοσης των συστημάτων αυτών. Η συνεχής ανάπτυξη στις τεχνολογίες πληροφοριών και τηλεπικοινωνιών έχουν οδηγήσει στην καθημερινά αυξανόμενη χρήση των εφαρμογών διαδικτύου υψηλής ταχύτητας και πολυμέσων, φέρνοντας στην επιφάνεια τη μεγάλη ανάγκη για υψηλότερους ρυθμούς μετάδοσης δεδομένων και μεγαλύτερο εύρος ζώνης. Για την ικανοποίηση των απαιτήσεων αυτών, κρίνεται αναγκαία η μετατόπιση των νέων συστημάτων δορυφορικών επικοινωνιών υψηλής απόδοσης σε υψηλότερες ζώνες συχνοτήτων, τόσο για συστήματα δορυφορικών επικοινωνιών κοντά στη Γη (Near Earth), όσο και για συστήματα δορυφορικών επικοινωνιών βαθέος διαστήματος (Deep Space). Μια πολλά υποσχόμενη λύση είναι η χρησιμοποίηση των οπτικών ασύρματων επικοινωνιών ελευθέρου χώρου (Free Space Optics, FSO) για δορυφορικά συστήματα επικοινωνίας. Τα οπτικά δορυφορικά συστήματα επικοινωνιών ελεύθερου χώρου λειτουργούν στο φάσμα των οπτικών συχνοτήτων και παρουσιάζουν μεγάλη ποικιλία πλεονεκτημάτων έναντι των δορυφορικών συστημάτων που λειτουργούν στην ζώνη ραδιοσυχνοτήτων (Radio Frequency, RF), όπως οι υψηλότεροι ρυθμοί μετάδοσης, το μεγαλύτερο διαθέσιμο φασματικό εύρος ζώνης, η λιγότερη κατανάλωση ενέργειας, η μικρότερη μάζα, ο μικρότερος όγκος και η βελτίωση στον τομέα της ασφάλειας.

Ωστόσο, όταν το οπτικό σήμα διαδίδεται μέσω της ατμόσφαιρας της γης, επηρεάζεται κυρίως αλλά όχι μόνο, από τις ατμοσφαιρικές αναταράξεις και τα σύννεφα. Η νεφοκάλυψη αποτελεί το πλέον περιοριστικό φαινόμενο για τη λειτουργία των συστημάτων οπτικών δορυφορικών επικοινωνιών, καθώς η εξασθένηση που υφίσταται το οπτικό σήμα με την παρουσία των νεφών είναι τόσο μεγάλη, που προκαλείται η διακοπή της ζεύξης. Επιπρόσθετα, σε συνθήκες διάδοσης χωρίς νέφη, τόσο η προς τα πάνω, όσο και η προς τα κάτω οπτική ζεύξη επηρεάζονται από το φαινόμενο των ατμοσφαιρικών στροβιλισμών. Για τον περιορισμό των φαινομένων αυτών έχουν προταθεί διάφορες τεχνικές αντιστάθμισης. Ως εκ τούτου, η παρούσα Διατριβή επικεντρώνεται κυρίως στην μοντελοποίηση των νεφών και των ατμοσφαιρικών στροβιλισμών για οπτικές δορυφορικές ζεύξεις και στους τρόπους αντιμετώπισης των φαινομένων αυτών.

Αρχικά, στο πρώτο Κεφάλαιο της παρούσας Διατριβής, παρουσιάζεται μια επισκόπηση των οπτικών δορυφορικών συστημάτων επικοινωνιών και γίνεται αναφορά, με τη χρήση σύγχρονων παραδειγμάτων στην ανάγκη για υψηλότερους ρυθμούς μετάδοσης δεδομένων και μεγαλύτερο φασματικό εύρος ζώνης. Παράλληλα, παρατίθενται διάφορες πειραματικές μελέτες που έχουν διεξαχθεί ως τώρα σχετικά με τα οπτικά δορυφορικά δίκτυα επικοινωνιών. Στο Κεφάλαιο 2, παρουσιάζονται τα φαινόμενα διάδοσης, τα οποία επηρεάζουν το οπτικό δορυφορικό σήμα, και δίνονται τα κυριότερα μοντέλα διάδοσης που έχουν προταθεί ως τώρα στη βιβλιογραφία. Τέλος, για κάθε φαινόμενο παρουσιάζονται οι τεχνικές άμβλυνσης διαλείψεων που έχουν προταθεί.

Τα Κεφάλαια 3, 4 και 5 εστιάζουν στις μεθοδολογίες που αναπτύχθηκαν στο πλαίσιο της παρούσας έρευνας σχετικά με τη μοντελοποίηση της νεφοκάλυψης και της εξασθένησης του σήματος εξαιτίας των νεφών. Όπως παρουσιάζεται στην παρούσα διατριβή, τα νέφη μπορούν να μοντελοποιηθούν χρησιμοποιώντας στατιστικά στοιχεία του Κάθετου Ολοκληρώματος της Περιεκτικότητας σε Υγρό Νερό των νεφών (Integrated Liquid Water Content, ILWC).

Στο Κεφάλαιο 3, παρουσιάζεται η μεθοδολογία που αναπτύχθηκε για την παραγωγή χρονοσειρών δισδιάστατων και τρισδιάστατων πεδίων του Κάθετου Ολοκληρώματος της Περιεκτικότητας σε Υγρό Νερό (ILWC) των νεφών. Η μεθοδολογία αυτή λαμβάνει υπόψη τόσο την χρονική όσο και χωρική συσχέτιση του ILWC. Για τη δημιουργία των χρονοσειρών η προτεινόμενη μεθοδολογία επωφελείται από τη χρήση πολυδιάστατων στοχαστικών διαφορικών εξισώσεων. Τέλος, στο χωροχρονικό μοντέλο 3 διαστάσεων που προτείνεται η κάθετη έκταση των νεφών λαμβάνεται υπόψη.

Στο Κεφάλαιο 4, τα χωροχρονικά μοντέλα δύο και τριών διαστάσεων, που προτάθηκαν στο Κεφάλαιο 3, χρησιμοποιούνται για τον υπολογισμό και την πρόβλεψη της εξασθένησης του σήματος λόγω νεφών και της πιθανότητας για οπτική ζεύξη χωρίς νέφη (Cloud Free Line of Sight, CFLOS), τόσο για μεμονωμένες όσο και για πολλαπλές ζεύξεις (διαφορισμός θέσης, από κοινού στατιστικά χαρακτηριστικά). Αρχικά, τα σύννεφα κατηγοριοποιούνται με βάση την κάθετη έκταση τους και λαμβάνοντας υπόψη τις μικροφυσικές ιδιότητες των νεφών και τη γνωστή θεωρία σκέδασης Mie, προτείνεται ένα καθολικό χωροχρονικό μοντέλο για τον υπολογισμό και πρόβλεψη της εξασθένησης του σήματος λόγω νεφών για συχνότητες μεγαλύτερες της Ka μπάντας [26,5 - 40GHz] με εφαρμογή έως και τις οπτικές συχνότητες. Η προτεινόμενη μεθοδολογία συγκρίνεται με δεδομένα που λαμβάνονται από τη βιβλιογραφία, παρουσιάζοντας πολύ ενθαρρυντικά αποτελέσματα. Συνεχίζοντας, υποθέτοντας ένα ανοιχτό/κλειστό (on/off) οπτικό κανάλι, με την παρουσία των νεφών, δηλαδή αν υπάρχει σύννεφο, η ζεύξη διακόπτεται, παρουσιάζεται μια νέα μεθοδολογία για τη σύνθεση χρονικά και χωρικά συσχετισμένων CFLOS χρονοσειρών, τόσο για μεμονωμένες, όσο και για πολλαπλές ζεύξεις. Και οι δύο προτεινόμενες μεθοδολογίες λαμβάνουν υπόψη τόσο τη γωνία ανύψωσης της ζεύξης όσο και υψόμετρο των σταθμών βάσης (για σταθμούς βάσης σε μεγάλο υψόμετρο) και εφαρμόζονται τόσο σε συστήματα με γεωστατικούς δορυφόρους όσο και σε συστήματα με μη-γεωστατικούς δορυφόρους, όπου η γωνία ανύψωσης της ζεύξης είναι χρονικά μεταβαλλόμενη. Τέλος, η προτεινόμενη χωροχρονική μεθοδολογία σύνθεσης συσχετισμένων CFLOS χρονοσειρών χρησιμοποιείται για την εξαγωγή χρήσιμων συστημικών στατιστικών χαρακτηριστικών για ένα δίκτυο οπτικών σταθμών βάσεως, όπως ο αριθμός των εναλλαγών (switches) μεταξύ των οπτικών σταθμών βάσεως.

Στο Κεφάλαιο 5 παρουσιάζεται ένα μαθηματικό μοντέλο για τον θεωρητικό υπολογισμό και την πρόβλεψη της πιθανότητας CFLOS, τόσο για μεμονωμένη οπτική δορυφορική ζεύξη όσο και για πολλαπλές χωρικά συσχετισμένες οπτικές δορυφορικές ζεύξεις. Για τον αξιόπιστο υπολογισμό της CFLOS πιθανότητας, η γωνία ανύψωσης της ζεύξης και το υψόμετρο του σταθμού βάσης λαμβάνονται υπόψη.

Επιπλέον, υπολογίζεται η CFLOS από κοινού πιθανότητα για ταυτόχρονα διαθέσιμες οπτικές ζεύξεις για την εφαρμογή τεχνικών μετάδοσης χωρικής πολυπλεξίας

Το Κεφάλαιο 6 της παρούσας Διατριβής επικεντρώνεται στην ανάπτυξη αλγορίθμων βελτιστοποίησης για την επιλογή των οπτικών σταθμών βάσης, που σχηματίζουν ένα συνδεδεμένο δίκτυο για την αντιμετώπιση της νεφοκάλυψης. Αρχικά, σε αυτό το κεφάλαιο αποδεικνύεται ότι τα μηνιαία στατιστικά χαρακτηριστικά του ILWC μπορούν να περιγραφούν επαρκώς με τη λογαριθμική κατανομή. Στη συνέχεια, οι μεθοδολογίες που αναπτύχθηκαν στα Κεφάλαια 4 και 5 μετασχηματίζονται με βάση τα μηνιαία στατιστικά χαρακτηριστικά του ILWC και ως εκ τούτου η μηνιαία διακύμανση της νεφοκάλυψης και οι μηνιαίες διαφορές μεταξύ του βόρειου και του νότιου ημισφαιρίου λαμβάνονται υπόψη. Οι αλγόριθμοι βελτιστοποίησης που προτείνονται λαμβάνουν υπόψη τη μηνιαία διακύμανση της νεφοκάλυψης και εκμεταλλεύονται τις μηνιαίες διαφορές μεταξύ βόρειου και νότιου ημισφαιρίου. Τέλος, προτείνεται ένας αλγόριθμος βελτιστοποίησης για τον υπολογισμό του αναγκαίου αριθμού των ενεργών σταθμών ανά μήνα σε ένα δίκτυο οπτικών σταθμών βάσης.

Το Κεφάλαιο 7 της παρούσας Διατριβής επικεντρώνεται στην ανάπτυξη νέων μοντέλων καναλιού για τη διάδοση του οπτικού σήματος κάτω από συνθήκες διάδοσης χωρίς νέφη, λαμβάνοντας υπόψη το φαινόμενο των ατμοσφαιρικών στροβιλισμών. Για τη μελέτη αυτή γίνεται ανάλυση μετρήσεων από το οπτικό δορυφορικό πείραμα ARTEMIS. Στο κεφάλαιο αυτό παρουσιάζεται μια μεθοδολογία για τον υπολογισμό του παράγοντα μέσης λήψης σήματος (aperture averaging factor) για οπτικούς δέκτες με κεντρική σκίαση για κατερχόμενη ζεύξη. Επιπρόσθετα, προτείνεται μια μεθοδολογία για τη δημιουργία χρονοσειρών λαμβανόμενης ακτινοβολίας/ισχύος για ανερχόμενες οπτικές ζεύξεις γεωστατικών δορυφορικών συστημάτων. Η προτεινόμενη μεθοδολογία λαμβάνει υπόψη τις επιπτώσεις που δημιουργούν στη διάδοση του σήματος οι ατμοσφαιρικοί στροβιλισμοί και τα σφάλματα στόχευσης. Επιπλέον, η παρούσα μεθοδολογία επωφελείται από τη χρήση στοχαστικών διαφορικών εξισώσεων για την παραγωγή χρονοσειρών σπινθηρισμού του πλάτους του σήματος. Τα αποτελέσματα των προτεινόμενων μεθοδολογιών συγκρίνονται με πραγματικά δεδομένα από το οπτικό δορυφορικό πείραμα ARTEMIS, παρουσιάζοντας πολύ ενθαρρυντικά αποτελέσματα.

Το Κεφάλαιο 8 της παρούσας Διατριβής επικεντρώνεται στο σχεδιασμό οπτικών ζεύξεων βαθέος διαστήματος. Στο κεφάλαιο αυτό παρουσιάζεται μια μεθοδολογία για τον υπολογισμό του προϋπολογισμού ισχύος οπτικής ζεύξης, για ζεύξεις βαθέος διαστήματος. Επιπλέον, προτείνεται μια νέα μέθοδος για την επιλογή των παραμέτρων σηματοδότησης (ρυθμός κωδικοποίησης, διάρκεια συμβόλου κ.ά.) της οπτικής ζεύξης. Χρησιμοποιώντας τις προτεινόμενες μεθοδολογίες εξετάζεται η απόδοση των οπτικών ζεύξεων βαθέος διαστήματος.

Τέλος, στο Κεφάλαιο 9, παρουσιάζονται συμπεράσματα και προτάσεις για μελλοντική έρευνα.

Ευχαριστίες

Με την παρούσα ενότητα, θα ήθελα να εκφράσω τις ευχαριστίες μου σε όλα εκείνα τα άτομα τα όποια συνέβαλαν είτε έχοντας συμβουλευτικό ρόλο, είτε μέσω συνεργασιών είτε προσφέροντας ηθική υποστήριξη ώστε να ολοκληρωθεί η παρούσα διατριβή.

Αρχικά, θα ήθελα να ευχαριστήσω θερμά τον επιβλέποντα καθηγητή της παρούσας Διδακτορικής Διατριβής, τον κύριο Αθανάσιο Δ. Παναγόπουλο, τόσο για την αποδοχή μου ως υποψήφιο διδάκτορα της σχολής, οσο και για την εμπιστοσύνη που μου έδειξε όλο αυτό το διάστημα. Ο κύριος Παναγόπουλος, με την εξαίρετη ακαδημαϊκή του γνώση και εμπειρία, με βοήθησε στην περάτωση αυτής μέσω των εύστοχων παρατηρήσεων, συμβουλών και παρακινήσεών του. Επιπρόσθετα, θα ήθελα να τον ευχαριστήσω για την ευκαιρία που μου έδωσε να εργαστώ πάνω σε ιδιαίτερα ενδιαφέροντα ερευνητικά προγράμματα, επιτρέποντάς μου με αυτόν τον τρόπο να εμπλουτίσω τις γνώσεις μου πάνω στο αντικείμενο της διατριβής αλλά και να έχω την απαραίτητη οικονομική υποστήριξη για την ολοκλήρωση της. Παράλληλα, η αίσθηση δικαιοσύνης και το ήθος που τον διακρίνουν, συνέβαλαν καθοριστικά στη δημιουργία ενός κατάλληλου περιβάλλοντος για την εκπόνηση της Διδακτορικής Διατριβής. Τέλος, θα ήθελα να τον ευχαριστήσω θερμά για την έμπρακτη στήριξη και βοήθεια που μου προσέφερε τόσο σε επαγγελματικό όσο και σε προσωπικό επίπεδο.

Επιπρόσθετα, θα ήθελα να ευχαριστήσω τον Δρ. Χαρίλαο Κουρόγιωργα, για τη συνεργασία μας όλα αυτά τα χρόνια, για τις συμβουλές, την καθοδήγηση, την ψυχολογική στήριξη, τόσο σε ηθικό όσο και σε προσωπικό επίπεδο, και την ενθάρρυνση που μου πρόσφερε. Το ήθος και το αίσθημα προσφοράς που τον διακρίνει, τον καθιστούν έναν εξαίρετο συνεργάτη και φίλο. Η βοήθειά του, τόσο σε επαγγελματικό όσο και σε προσωπικό επίπεδο, ήταν ιδιαιτέρα σημαντική.

Θα ήθελα να ευχαριστήσω τους συνεργάτες και φίλους, Δρ. Παντελή Αράπογλου, Δρ. Κωνσταντίνο Λιώλη, Δρ. Γεώργιο Πιτσιλάδη, Δρ. Σταυρούλα Βασσάκη, Δρ. Μάριο Πουλάκη, Δρ. Σταύρο Σαγκριώτη, Αργύρη Ρουμελιώτη, Απόστολο Παπαφραγκάκη και Χρίστο Εφραίμ. Με τη συνεργασία μας σε επαγγελματικό επίπεδο και την υποστήριξη τους κατάφερα να φέρω εις πέρας την έρευνά μου. Τους ευχαριστω για τη συμπαράστασή τους, τη βοήθειά τους και τις ευχάριστες ώρες που περάσαμε μαζί.

Στο σημείο αυτό, θα ήθελα να εκφράσω τις ευχαριστίες μου και στους φίλους μου εκτός εργασίας, με τους οποίους μοιραστήκαμε σκέψεις, ανησυχίες και δυσκολίες, αλλά ταυτόχρονα περάσαμε όμορφες προσωπικές στιγμές κάνοντας ευχάριστη την καθημερινότητα και την πορεία μέχρι εδώ.

Ολοκληρώνοντας, θα ήθελα να πω το πιο μεγάλο ευχαριστώ στην οικογένειά μου για τη στήριξη, την αγάπη και την εμπιστοσύνη τους, από τα πρώτα κιόλας βήματά μου. Η υποστήριξή τους ήταν και είναι καθοριστικής σημασίας για την επίτευξη των στόχων μου. Θέλω να ευχαριστήσω τους γονείς μου, Κωνσταντίνο και Σταυρούλα, για όλες τις θυσίες που έχουν κάνει και για τις βάσεις και τα ψυχικά αποθέματα με τα οποία με έχουν εφοδιάσει, ώστε να συνεχίζω να προσπαθώ μέχρι την επίτευξη των στόχων

23

στη μητέρα μου Σταυρούλα,

στον αδερφό μου Ιωάννη

και στη μνήμη του πατέρα μου

Κωνσταντίνου

Εκτεταμένη Περίληψη

ΚΕΦΆΛΑΙΟ 1   ΕΙΣΑΓΩΓΗ

Η συνεχής ανάπτυξη στην τεχνολογία των πληροφοριών και των ραδιοσυχνοτήτων (Radio Frequencies, RF) έχουν οδηγήσει στην καθημερινά αυξανόμενη χρήση των εφαρμογών διαδικτύου υψηλής ταχύτητας και πολυμέσων. Κάθε χρήστης παράγει και μεταδίδει καθημερινά μεγάλο όγκο δεδομένων (κινητά τηλέφωνα, αισθητήρες κλπ.), ενώ σε λίγα χρόνια προβλέπεται ότι όγκος των δεδομένων αυτών θα αυξηθεί δραματικά, φέρνοντας στην επιφάνεια τη μεγάλη ανάγκη για υψηλότερους ρυθμούς μετάδοσης δεδομένων και μεγαλύτερο εύρος ζώνης. Παράλληλα, στις νέες αρχιτεκτονικές των τηλεπικοινωνιακών δικτύων υπάρχουν απαιτήσεις για ευρυζωνικές και διαδραστικές δορυφορικές υπηρεσίες. Σύμφωνα με την Ευρωπαϊκή ψηφιακή ατζέντα [EU Broadband] που δημοσιεύθηκε το 2010 έχουν τεθεί τρεις στόχοι σχετικά με το ευρυζωνικό διαδίκτυο: α) η κάλυψη του συνόλου του ευρωπαϊκού πληθυσμού με ευρυζωνικές επικοινωνίες με ταχύτητες μέχρι 30Mbps μέχρι το 2013 (υλοποιήθηκε), β) η κάλυψη του συνόλου του ευρωπαϊκού πληθυσμού με ευρυζωνικές επικοινωνίες με ταχύτητες μεγαλύτερες των 30Mbps μέχρι το 2020 και γ) τουλάχιστον το 50% του ευρωπαϊκού πληθυσμού να έχει ευρυζωνικές επικοινωνίες με ταχύτητες μεγαλύτερες των 100Mbps μέχρι το 2020.

Παρότι παρατηρείται πρόοδος σχετικά τους στόχους αυτούς, αναμένεται να μην υπάρχει πλήρης επίτευξη μέχρι το 2020 [EU Broadband]. Για την επίτευξη των στόχων αυτών και ειδικότερα να γίνουν οικονομικά εφικτοί, τα δορυφορικά συστήματα επικοινωνιών θα παίξουν σημαντικό ρόλο και ιδιαίτερα για δυσπρόσιτες και αραιοκατοικημένες περιοχές. Ωστόσο παρόλο που η λύση των δορυφορικών επικοινωνιών πλεονεκτεί στην κάλυψη των αναγκών αυτών σε ευρεία γεωγραφική έκταση, για να παραμείνουν ανταγωνιστικές έναντι των επίγειων δικτύων, κρίνεται αναγκαία η συνεχής αύξηση της προσφερόμενης χωρητικότητας.

Για την ικανοποίηση των απαιτήσεων αυτών, κρίνεται αναγκαία η μετατόπιση των νέων συστημάτων δορυφορικών επικοινωνιών υψηλής απόδοσης σε υψηλότερες ζώνες συχνοτήτων, τόσο για συστήματα δορυφορικών επικοινωνιών κοντά στη Γη (Near Earth), όσο και για για συστήματα δορυφορικών επικοινωνιών βαθέος διαστήματος (Deep Space). Μια πολλά υποσχόμενη λύση είναι η χρησιμοποίηση των οπτικών ασύρματων επικοινωνιών ελευθέρου χώρου (Free Space Optics, FSO) για δορυφορικά συστήματα επικοινωνίας. Τα οπτικά δορυφορικά συστήματα επικοινωνιών ελεύθερου χώρου λειτουργούν στο φάσμα των οπτικών συχνοτήτων και παρουσιάζουν μεγάλη ποικιλία πλεονεκτημάτων έναντι των δορυφορικών συστημάτων που λειτουργούν στην ζώνη ραδιοσυχνοτήτων (RF), όπως οι υψηλότεροι ρυθμοί μετάδοσης, το μεγαλύτερο διαθέσιμο φασματικό εύρος ζώνης, η λιγότερη κατανάλωση ενέργειας, η μικρότερη μάζα και ο μικρότερος όγκος και η βελτίωση στον τομέα της ασφάλειας μεταξύ άλλων [Kaushal17].

Τα δορυφορικά συστήματα επικοινωνιών συμπεριλαμβάνουν αμφίδρομες ζεύξεις μεταξύ Γης και Γεωστατικών Δορυφόρων, Δορυφόρων Μέσης και Χαμηλής τροχιάς, Μίκρο-Δορυφόρων, επανδρωμένων και μη εναέριων οχημάτων καθώς και ζεύξεις είτε μεταξύ των δορυφόρων είτε των δορυφόρων και των επανδρωμένων και μη εναέριων οχημάτων.

Δεδομένου ότι η χρησιμοποίηση του οπτικού φάσματος στα δορυφορικά συστήματα επικοινωνιών αποτελεί μια ελκυστική λύση, έχουν ήδη πραγματοποιηθεί διάφορες πειραματικές μελέτες με στόχο την ανάλυση βιωσιμότητας των συστημάτων αυτών, καθώς και τη μελέτη των ατμοσφαιρικών φαινομένων που επηρεάζει την ασύρματη μετάδοση του οπτικού σήματος [Kaushal17], [Romba04], [Toyoshima08].

Εξαιτίας της αξιοπιστίας και της αυξημένης ασφάλειας που προσφέρουν οι οπτικές δορυφορικές επικοινωνίες, το τελευταίο διάστημα υπάρχει αυξημένο ενδιαφέρον για την έρευνα και υλοποίηση εφαρμογών διανομής κβαντικών κλειδιών (Quantum Key Distribution) από δορυφόρο χαμηλής τροχιάς. Επιπρόσθετα, ήδη κάποιες εταιρείες όπως η Laser Light Communications (www.laserlightcomms.com/) έχουν προδιαγράψει την υλοποίηση παγκόσμιου οπτικού δικτύου επικοινωνιών με τη χρήση δορυφόρων μέσης τροχιάς [Brumley16]. Τέλος, ιδιαίτερο ενδιαφέρον έχει αναπτυχθεί για τη χρήση των ασύρματων οπτικών επικοινωνιών για ζεύξεις βαθέος διαστήματος. Στη βιβλιογραφία γίνεται εκτενής αναφορά σε μελέτες για τη χρήση του οπτικού σήματος σε ζεύξεις βαθέος διαστήματος.

ΚΕΦΑΛΑΙΟ 2   ΑΤΜΟΣΦΑΙΡΙΚΑ ΦΑΙΝΟΜΕΝΑ ΠΟΥ ΕΠΗΡΕΑΖΟΥΝ ΤΗΝ ΟΠΤΙΚΗ ΖΕΥΞΗ

Όταν το οπτικό σήμα διαδίδεται μέσω της ατμόσφαιρας της γης, επηρεάζεται από διάφορα φαινόμενα, όπως τα σωματίδια της ατμόσφαιρας, τα σύννεφα νερού, τα σύννεφα πάγου (cirrus clouds) και τους ατμοσφαιρικούς στροβιλισμούς μεταξύ άλλων [Kaushal17], [CCSDS17a]. Για τον αξιόπιστο σχεδιασμό των συστημάτων οπτικών δορυφορικών επικοινωνιών, η επίδραση αυτών των φαινομένων πρέπει να υπολογιστεί με ακρίβεια. Στο παρόν κεφάλαιο παρουσιάζονται οι κύριοι παράγοντες που επηρεάζουν τη διάδοση του οπτικού σήματος μέσα από την ατμόσφαιρα, καθώς και οι τεχνικές άμβλυνσης διαλείψεων που έχουν προταθεί για κάθε περίπτωση. Επιπρόσθετα, δίνονται τα κυριότερα μοντέλα διάδοσης που έχουν προταθεί ως τώρα στη σχετική διεθνή βιβλιογραφία.

Μεταξύ των φαινομένων αυτών, η νεφοκάλυψη (σύννεφα νερού) αποτελεί το πλέον περιοριστικό φαινόμενο για τη λειτουργία των συστημάτων οπτικών δορυφορικών επικοινωνιών, καθώς η εξασθένηση που υφίσταται το οπτικό σήμα με την παρουσία των νεφών είναι τόσο μεγάλη που προκαλείται η διακοπή της ζεύξης. Για το λόγο αυτό, στα δορυφορικά συστήματα οπτικών επικοινωνιών μπορούμε να θεωρήσουμε ένα ανοιχτό/κλειστό (on/off) οπτικό κανάλι με την παρουσία των νεφών, δηλαδή αν υπάρχει σύννεφο κατά μήκος του δρόμου διάδοσης που επηρεάζει τη ζεύξη αυτή θεωρούμε ότι διακόπτεται και, αντίστοιχα, ορίζεται ως δυαδικό μέγεθος η διάδοση χωρίς νέφη (Cloud Free Line of Sight, CFLOS), δηλαδή CFLOS=1

εάν δεν υπάρχει σύννεφο που επηρεάζει την οπτική ζεύξη ή CFLOS=0 αν υπάρχει σύννεφο που επηρεάζει την οπτική ζεύξη και αντίστοιχα ορίζεται η CFLOS πιθανότητα για κάθε περιοχή ενδιαφέροντος. Στη βιβλιογραφία έχουν παρουσιαστεί διάφορες μελέτες για τον υπολογισμό της CFLOS πιθανότητας, τόσο για μεμονωμένες, όσο και για πολλαπλές ζεύξεις, με τη χρήση δεδομένων νεφοκάλυψης που προέρχονται από μετεωρολογικούς δορυφόρους. Επιπλέον, για τη μοντελοποίηση των νεφών και ως εκ τούτου τόσο της εξασθένησης του σήματος λόγω νεφών, όσο και της CFLOS πιθανότητας, μπορούν να χρησιμοποιηθούν στατιστικά στοιχεία του Κάθετου Ολοκληρώματος της Περιεκτικότητας σε Υγρό Νερό των νεφών, (Integrated Liquid Water Content, ILWC). Για την αντιμετώπιση του φαινομένου αυτού, προτείνεται η τεχνική διαφορισμού: διαφορισμός θέσης (διαφορισμός οπτικών επίγειων σταθμών). Στην περίπτωση αυτή ορίζεται η από κοινού CFLOS πιθανότητα, δηλαδή η πιθανότητα μια τουλάχιστον από τις οπτικές ζεύξεις να μην έχει διακοπεί εξαιτίας των νεφών.

Επιπρόσθετα, σε συνθήκες διάδοσης χωρίς νέφη, τόσο η ανερχόμενη, όσο και η κατερχόμενη οπτική ζεύξη επηρεάζονται από το φαινόμενο των ατμοσφαιρικών στροβιλισμών. [Kaushal17], [CCSDS17a]. Στην περίπτωση της κατερχόμενης ζεύξης χρησιμοποιούνται οπτικοί δέκτες (τηλεσκόπια) μεγάλης διαμέτρου για την άμβλυνση των ατμοσφαιρικών αναταράξεων (aperture averaging), ενώ στην περίπτωση της ανερχόμενης ζεύξης χρησιμοποιείται η τεχνική διαφορισμού πομπού και τεχνικές προ-αντιστάθμισης. Επιπρόσθετα, για τον περιορισμό των ατμοσφαιρικών αναταράξεων μπορούν να χρησιμοποιηθούν προσαρμοστικά οπτικά συστήματα.

ΚΕΦΆΛΑΙΟ 3   ΜΟΝΤΕΛΟΠΟΙΗΣΗ   ΤΟΥ   ΚΑΘΕΤΟΥ   ΟΛΟΚΛΗΡΩΜΑΤΟΣ   ΤΗΣ ΠΕΡΙΕΚΤΙΚΟΤΗΤΑΣ ΣΕ ΥΓΡΟ ΝΕΡΟ ΤΩΝ ΝΕΦΩΝ (ILWC)

Για τη μοντελοποίηση των νεφών μπορούν να χρησιμοποιηθούν στατιστικά στοιχεία του Κάθετου Ολοκληρώματος της Περιεκτικότητας σε Υγρό Νερό των νεφών (Integrated Liquid Water Content, ILWC). Όπως αποδεικνύεται στα [ITU840], [Jeannin08] τα ετήσια στατιστικά χαρακτηριστικά του ILWC μπορούν να περιγραφούν από τη λογαριθμοκανονική κατανομή. Ως εκ τούτου, για τη σύνθεση χρονοσειρών του ILWC *(L)* για μια συγκεκριμένη περιοχή χρειάζονται οι στατιστικές παράμετροι του *ln(L),* δηλαδή η μέση τιμή (*m*), η τυπική απόκλιση (*σ*) και η πιθανότητα το ILWC να είναι μεγαλύτερο του μηδενός, ή αλλιώς η πιθανότητα νεφοκάλυψης για τη συγκεκριμένη περιοχή ενδιαφέροντος. Στην [ITU1853-1] προτείνεται μια μεθοδολογία για τη σύνθεση σημειακών χρονοσειρών του ILWC συσχετισμένες μόνο στο χρόνο και όχι στο χώρο. Ωστόσο, για τον αξιόπιστο υπολογισμό της επίδρασης των νεφών κατά μήκος του δρόμου διάδοσης του σήματος ένα μόνο σημείο δεν επαρκεί. Παράλληλα, όπως συζητήθηκε και στην εισαγωγή, για την αντιμετώπιση των νεφών χρησιμοποιείται η τεχνική διαφορισμού των οπτικών σταθμών (διαφορισμός θέσης). Ως εκ τούτου, η χωρική συσχέτιση των νεφών, τόσο κατα μήκος του δρόμου διάδοσης, όσο και

μεταξύ διαφορετικών σταθμών (διαφορετικών περιοχών) αποτελεί σημαντικό μέρος της μοντελοποίησης των νεφών.

Στο κεφάλαιο αυτό, παρουσιάζεται η μεθοδολογία που αναπτύχθηκε για την παραγωγή χρονοσειρών δισδιάστατων και τρισδιάστατων πεδίων του Κάθετου Ολοκληρώματος της Περιεκτικότητας σε Υγρό Νερό (ILWC) των νεφών. Η προτεινόμενη μεθοδολογία, μεταξύ άλλων, ενσωματώνει τη χωρική και χρονική συσχέτιση του ILWC.

Πιο συγκεκριμένα στο υποκεφάλαιο 3.1 προτείνεται μια μεθοδολογία βασισμένη στις πολυδιάστατες στοχαστικές διαφορικές εξισώσεις και στην [ITU1853-1] για την παραγωγή χρονοσειρών δισδιάστατων πεδίων του ILWC. Η μεθοδολογία αυτή λαμβάνει υπόψη τόσο την χρονική όσο και χωρική συσχέτιση του ILWC. Η κεντρική ιδέα βασίζεται στη σύνθεση δισδιάστατων χαρτών ILWC για κάθε οπτικό σταθμό βάσης. Κάθε χάρτης αποτελείται από έναν αριθμό δισδιάστατων χωρικά και χρονικά συσχετισμένων πεδίων του ILWC με διαστάσεις 1 km x 1km που μπορει να διατυπωθεί ως $L_{map,GS} = [L_1, L_2, ..., L_n]$, όπου τα L_i είναι τα ILWC πεδία και n ο αριθμός των πεδίων που αντιστοιχούν σε κάθε σταθμό. Για περισσότερους από έναν οπτικούς σταθμούς, ένας ILWC χάρτης δημιουργείται για κάθε σταθμό. Πρέπει να τονιστεί ότι και όλοι οι χάρτες μεταξύ τους είναι χωρικά και χρονικά συσχετισμένοι. Θεωρώντας s αριθμό σταθμών τότε το συνολικό πεδίο που δημιουργείται μπορεί να γραφεί ως $L_{total\_field} = [L_{map,GS^1} \ L_{map,GS^2} \ ... \ L_{map,GS^s}]$. Έτσι οι χρονοσειρές L_i μπορούν να υπολογιστούν με τον παρακάτω τύπο [J1]

$$L_i(t) = \begin{cases} \exp\left[Q^{-1}\left(\frac{1}{P_{CLW}}Q(G_i(t))\right)\times\sigma+m\right] & G_i(t)\geq\alpha_{th} \\ 0 & G_i(t)\leq\alpha_{th} \end{cases} \quad (1.1)$$

όπου m είναι η μέση τιμή, $σ$ η τυπική απόκλιση και P_{CLW} η πιθανότητα το ILWC>0 του $ln(L)$ για την περιοχή ενδιαφέροντος. Οι στατιστικές παράμετροι του $ln(L)$ μπορούν να εξαχθούν από βάσεις δεδομένων όπως η ERA-Interim και ITU-R P.840-6 [ITU860-6].

Ο όρος $G_i(t)$ συμβολίζει τη γκαουσιανή διαδικασία που απαιτείται για τη σύνθεση των πεδίων ILWC. Το $G_i(t)$ μπορεί να μοντελοποιηθεί ως η υπέρθεση δύο γκαουσιανών διαδικασιών $X_i =[X_i^1, X_i^2]$ όπου $1\leq i\leq n$ (n ο αριθμός των πεδίων που αντιστοιχούν σε κάθε σταθμό και s ο αριθμός των σταθμών). Για τη σύνθεση των X_i^k διαδικασιών χρησιμοποιούνται πολυδιάστατες στοχαστικές διαφορικές εξισώσεις, λαμβάνοντας υπόψη τη χωροχρονική συσχέτιση του ILWC.

Στη συνέχεια στο υποκεφάλαιο 3.2 παρουσιάζεται η μεθοδολογία για τη δημιουργία τρισδιάστατων πεδίων του ILWC λαμβάνοντας υπόψη και την κάθετη έκταση των νεφών. Αρχικά εφαρμόζεται η μεθοδολογία για τη δημιουργία δισδιάστατων πεδίων του ILWC και έπειτα χρησιμοποιώντας τη σχέση που

προτάθηκε στο [Luini14], οπου συνδέεται η περιεκτικότητα των νεφών σε υγρό νερό (Liquid Water Content) με το ύψος και το ILWC, υπολογίζεται για κάθε πεδίο ILWC και για κάθε χρονική στιγμή η κάθετη έκταση του πεδίου. Με τη διαδικασία αυτή, παράγονται χρονοσειρές τρισδιάστατων πεδίων του ILWC.

Στα Σχήματα 1 και 2, παρουσιάζονται στιγμιότυπα ενός δισδιάστατου και ενός τρισδιάστατου ILWC χάρτη αντίστοιχα, για έναν υποθετικό σταθμό στα Χανιά, Κρήτης. πάνω: τη χρονική στιγμή $t=t_0$ και κάτω: 60 λεπτά αργότερα.
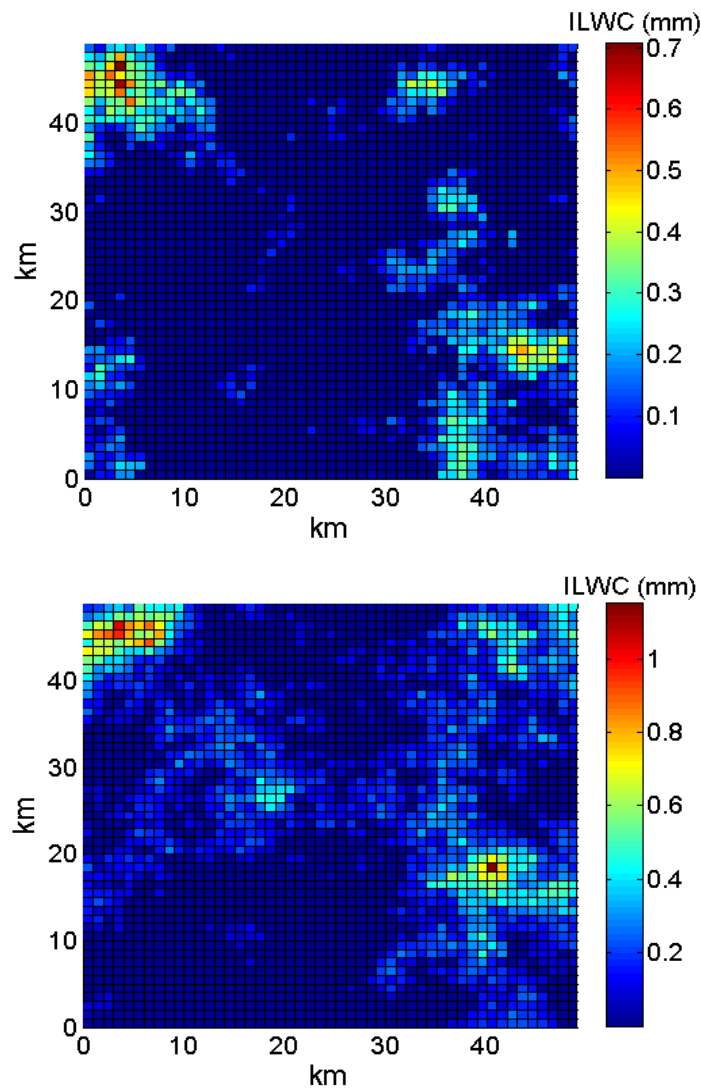
Σχήμα 1: Στιγμιότυπα δισδιάστατων ILWC χαρτών: Πάνω: τη χρονική στιγμή $t=t_0$, Κάτω: 60 λεπτά αργότερα
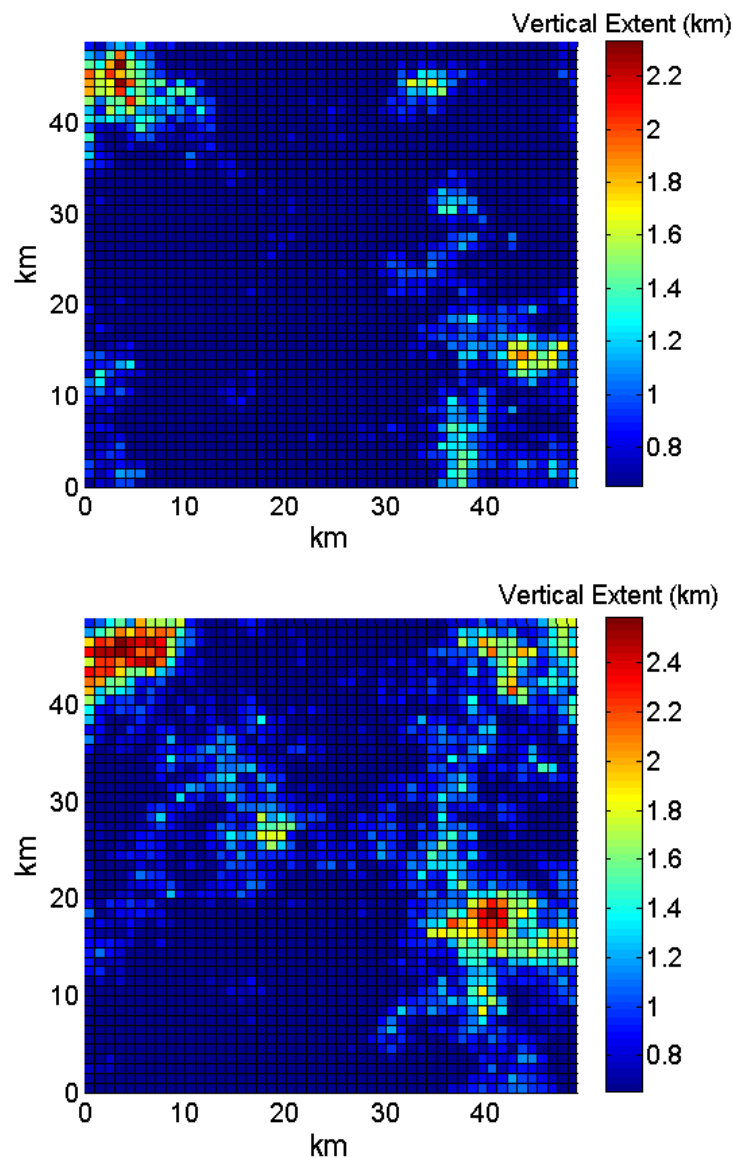
Σχήμα 2: Στιγμιότυπα τρισδιάστατων ILWC χαρτών: Πάνω: τη χρονική στιγμή $t=t_0$ **, Κάτω: 60 λεπτά αργότερα**

Στο υποκεφάλαιο 3.3 εξετάζεται η ικανότητα της προτεινόμενης χωροχρονικης διαδικασίας για τη δημιουργία ILWC χρονοσειρών, να αναπαράγει τα στατιστικά στοιχεία πρώτης τάξης του ILWC.

ΚΕΦΆΛΑΙΟ 4   ΣΥΝΘΕΣΗ ΧΡΟΝΟΣΕΙΡΩΝ ΕΞΑΣΘΕΝΗΣΗΣ ΤΟΥ ΣΗΜΑΤΟΣ ΛΟΓΩ ΝΕΦΩΝ – ΣΥΝΘΕΣΗ CFLOS ΧΡΟΝΟΣΕΙΡΩΝ

Στο κεφάλαιο αυτό, τα χωροχρονικά μοντέλα δύο και τριών διαστάσεων που προτάθηκαν στο Κεφάλαιο 3 χρησιμοποιούνται για τη σύνθεση χρονοσειρών εξασθένησης του σήματος λόγω νεφών και για

οπτική ζεύξη χωρίς νέφη (Cloud Free Line of Sight, CFLOS), τόσο για μεμονωμένες, όσο και για πολλαπλές ζεύξεις (διαφορισμός θέσης, από κοινού στατιστικά χαρακτηριστικά). Και οι δύο προτεινόμενες μεθοδολογίες λαμβάνουν υπόψη τόσο τη γωνία ανύψωσης της ζεύξης, όσο και το υψόμετρο των σταθμών βάσης (για σταθμούς βάσης σε μεγάλο υψόμετρο).

Αρχικά, στο υποκεφάλαιο 4.1, χρησιμοποιώντας το χωροχρονικό μοντέλο τριών διαστάσεων που προτάθηκε στο Κεφάλαιο 3, τα σύννεφα κατηγοριοποιούνται με βάση την κάθετη έκταση τους και λαμβάνοντας υπόψη τις μικρο-φυσικές ιδιότητες των νεφών και τη γνωστή θεωρία σκέδασης Mie, προτείνεται ένα καθολικό χωροχρονικό μοντέλο για τον υπολογισμό και την πρόβλεψη της εξασθένησης του σήματος λόγω νεφών, για συχνότητες μεγαλύτερες της Ka μπάντας [26,5-40GHz], με εφαρμογή έως και τις οπτικές συχνότητες. Οι χρονοσειρές απόσβεσης εξαιτίας νεφών, που βρίσκονται στον κεκλιμένο δρόμο διάδοσης του σήματος, μπορούν να υπολογιστούν χρησιμοποιώντας τον παρακάτω τύπο:

$$A(t,\lambda) = \int_{l_0}^{l_{max}} 4.343 \times 10^3 \int_0^\infty \sigma_{ext}(r,\lambda)n(r,h)dr\ d\ell\ \text{(dB)} \qquad (1.2)$$

όπου το σ_{ext} είναι η διατομή απόσβεσης (extinction cross section), το $n(r,h)$ είναι η κατανομή μεγέθους σωματιδίων (particle size distribution PSD) των νεφών και λ το μήκος κύματος που χρησιμοποιείται. Οι παράμετροι της PSD υπολογίζονται ανάλογα με το είδος του νέφους. Καθώς, για τον υπολογισμό του σ_{ext}, εφαρμόζεται η γνωστή θεωρία σκέδασης Mie, η προτεινόμενη μεθοδολογία μπορεί να χρησιμοποιηθεί για όλο το φάσμα των συχνοτήτων, από την Ka μπάντα μέχρι το φάσμα των οπτικών συχνοτήτων. Η προτεινόμενη μεθοδολογία συγκρίνεται με δεδομένα που λαμβάνονται από τη βιβλιογραφία, παρουσιάζοντας πολύ ενθαρρυντικά αποτελέσματα, όπως φαίνεται από το παρακάτω σχήμα για μια κάθετη ζεύξη στο Μιλάνο, Ιταλία που λειτουργεί σε μήκος κύματος 10.6μm.
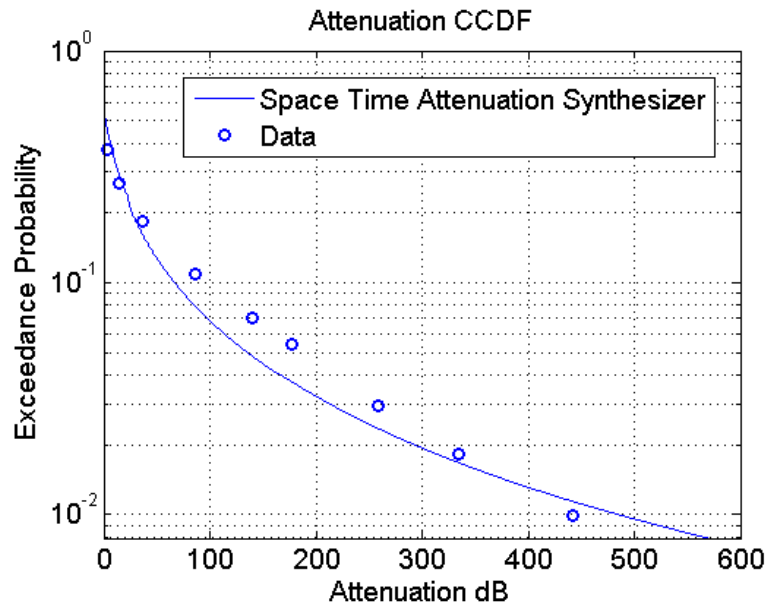
Σχήμα 3: Σύγκριση προτεινόμενης μεθοδολογίας για τη δημιουργία χρονοσειρών απόσβεσης οπτικού σήματος εξαιτίας των νεφών με δεδομένα από τη βιβλιογραφία

Τέλος, στο υποκεφάλαιο αυτό παρουσιαάζονται αριθμητικά αποτελεσμάτα εξασθένησης του σήματος λόγω νεφών για συχνοτητες μεγαλύτερες της Ka μπάντας [26.5-40GHz], έως την οπτική μπάντα.

Συνεχίζοντας, στο υποκεφάλαιο 4.2 υποθέτοντας ένα ανοιχτό/κλειστό (on/off) οπτικό κανάλι με την παρουσία των νεφών, παρουσιάζεται μια μεθοδολογία για τη σύνθεση χρονικά και χωρικά συσχετισμένων CFLOS χρονοσειρών, τόσο για μεμονωμένες όσο και για πολλαπλές ζεύξεις.

Στο υποκεφάλαιο 4.3 οι προτεινόμενες μεθοδολογίες τροποποιούνται για να χρησιμοποιηθούν για οπτικά συστήματα με μη-γεωστατικούς δορυφόρους, όπου η γωνία ανύψωσης της ζεύξης είναι χρονικά μεταβαλλόμενη και στο υποκεφάλαιο 4.5 οι προτεινόμενες μεθοδολογίες για τη δημιουργία CFLOS χρονοσειρών χρησιμοποιούνται για την παρουσίαση αριθμητικών αποτελεσμάτων θεωρώντας γεωστατικούς και μη δορυφόρους.

Τέλος, στο υποκεφάλαιο 4.5, η προτεινόμενη χωροχρονική μεθοδολογία σύνθεσης συσχετισμένων CFLOS χρονοσειρών χρησιμοποιείται για την εξαγωγή χρήσιμων συστημικών στατιστικών χαρακτηριστικών για ένα δίκτυο οπτικών σταθμών βάσεως όπως ο αριθμός των εναλλαγών (switches) των οπτικών σταθμών βάσεως.

ΚΕΦΆΛΑΙΟ 5   ΘΕΩΡΗΤΙΚΗ ΜΟΝΤΕΛΟΠΟΙΗΣΗ CFLOS ΠΙΘΑΝΟΤΗΤΑΣ

Στο κεφάλαιο αυτό παρουσιάζεται ένα μαθηματικό μοντέλο για τον θεωρητικό υπολογισμό και την πρόβλεψη της CFLOS πιθανότητας, τόσο για μεμονωμένη οπτική δορυφορική ζεύξη, όσο και για πολλαπλές

χωρικά συσχετισμένες οπτικές δορυφορικές ζεύξεις. Για τον αξιόπιστο υπολογισμό της CFLOS πιθανότητας, η γωνία ανύψωσης της ζεύξης και το υψόμετρο του σταθμού βάσης λαμβάνονται υπόψη.

Αρχικά, στο υποκεφάλαιο 5.1 παρουσιάζεται η μεθοδολογία για τον θεωρητικό υπολογισμό της CFLOS πιθανότητας για μια μεμονωμένη οπτική δορυφορική ζεύξη. Θεωρώντας ότι το ILWC έχει σταθερή τιμή σε ένα πεδίο στο οριζόντιο επίπεδο με διαστάσεις $1 km^2$, δηλαδή στο επίπεδο που ορίζεται από μια γραμμή 1 km στον χ άξονα και μια γραμμή 1 km στον y άξονα, τότε ο κεκλιμένος δρόμος διάδοσης μπορεί να χωριστεί σε *n* τέτοια πεδία και η CFLOS πιθανότητα ορίζεται ως η πιθανότητα κανένα από τα *i=1-n* πεδία να μην επηρεάζουν την οπτική ζεύξη.

Επιπλέον, όπως περιγράφεται στο κεφάλαιο 3 της παρούσας διατριβής, το ILWC μπορεί να μοντελοποιηθεί ως μια βαθυπερατή Γκαουσιανή διαδικασία περικομμένη (truncated) σε ένα επιθυμητό κατώφλι, για να αναπαράγει την επιθυμητή πιθανότητα εμφάνισης νεφών. Έτσι, χρησιμοποιώντας τις κανονικά κατανεμημένες τυχαίες μεταβλητές $u_i = \left(\ln(L_i) - m_i \right)/\sigma_i$ η CFLOS πιθανότητα για μια μεμονωμένη ζεύξη δίνεται με την παρακάτω έκφραση:

$$P_{CFLOS} = P\left(u_1 < a_{1,th}, .., u_n < a_{n,th} \right) =$$
$$= \int_{-\infty}^{a_{1,th}} .. \int_{-\infty}^{a_{n,th}} f_{u_1..u_n} \left(u_1, .., u_n \right) \cdot du_1 \cdot \cdot du_n$$

(1.3)

όπου $f_{u_1..u_n}$ είναι η συνάρτηση πυκνότητας πιθανότητας της πολυμεταβλητής κανονικής κατανομής και *i=1-n* τα πεδία κατα μήκος του δρόμου διάδοσης του σήματος. Τα περικομμένα κατώφλια $\alpha_{i,th}(i=1,...,n)$ υπολογίζονται με βάση τη γωνία ανύψωσης και το υψόμετρο του σταθμού βάσης.

Στο υποκεφάλαιο 5.2 παρουσιάζεται η μεθοδολογία για τον θεωρητικό υπολογισμό της απο κοινού CFLOS πιθανότητας για πολλαπλές οπτικές ζεύξεις, ενώ στο υποκεφάλαιο 5.3 υπολογίζεται η από κοινού CFLOS πιθανότητα για ταυτόχρονα διαθέσιμες οπτικές ζεύξεις, για την εφαρμογή τεχνικών μετάδοσης χωρικής πολυπλεξίας.

ΚΕΦΆΛΑΙΟ 6   ΜΗΝΙΑΙΑ CFLOS ΣΤΑΤΙΣΤΙΚΑ ΧΑΡΑΚΤΗΡΙΣΤΙΚΑ – ΑΛΓΟΡΙΘΜΟΙ ΒΕΛΤΙΣΤΟΠΟΙΗΣΗΣ ΓΙΑ ΤΗ ΔΙΑΣΤΑΣΙΟΠΟΙΗΣΗ ΟΠΤΙΚΟΥ ΕΠΙΓΕΙΟΥ ΔΙΚΤΥΟΥ

Το κεφάλαιο αυτό επικεντρώνεται στην ανάπτυξη αλγορίθμων βελτιστοποίησης για την επιλογή των επίγειων οπτικών σταθμών, που σχηματίζουν ένα δίκτυο (διαφορισμός θέσης) για την αντιμετώπιση της νεφοκάλυψης.

Αρχικά, γίνεται ιδιαίτερη αναφορά στη μηνιαία διακύμανση της πιθανότητας νεφοκάλυψης αλλά και στις διαφορές μεταξύ των περιοχών στα 2 ημισφαίρια. Οι επισημάνσεις αυτές γίνονται εύκολα αντιληπτές στην παρακάτω εικόνα, όπου παρουσιάζεται η μηνιαία (συμβολίζεται με Μ) πιθανότητα νεφοκάλυψης για 2

σταθμούς, έναν στο Βόρειο Ημισφαίριο (South Mountain, California) και έναν στο Νότιο Ημισφαίριο (Malargue, Argentina), καθώς και ο ετήσιος μέσος όρος (συμβολίζεται με Υ) της πιθανότητας νεφοκάλυψης για κάθε μια, για το έτος 2000.
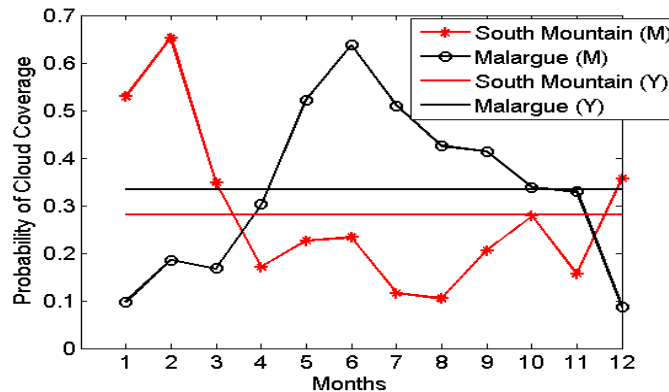
Σχήμα 4: Μηνιαία και Ετήσια Πιθανότητα Νεφοκάλυψης, Βόρειο/Νότιο Ημισφαίριο

Στο υποκεφάλαιο 6.1 αποδεικνύεται ότι τα μηνιαία στατιστικά χαρακτηριστικά του ILWC μπορούν να περιγραφούν επαρκώς με τη λογαριθμική κατανομή.

Στο υποκεφάλαιο 6.2 η μεθοδολογία που προτάθηκε στο υποκεφάλαιο 4.2 για τη σύνθεση CFLOS χρονοσειρών, μετασχηματίζεται με βάση τα μηνιαία στατιστικά χαρακτηριστικά του ILWC.

Επιπρόσθετα, στο υποκεφάλαιο 6.3 δίνονται αναλυτικές σχέσεις για τον υπολογισμό της μηνιαίας CFLOS πιθανότητας, για μεμονωμένες και πολλαπλές ζεύξεις. Παράλληλα, προτείνονται 2 αλγόριθμοι βελτιστοποίησης για την επιλογή των επίγειων οπτικών σταθμών, για την άμβλυνση του φαινομένου παρεμβολής των νεφών. Οι αλγόριθμοι αυτοί λαμβάνουν υπόψη τη μηνιαία διακύμανση της πιθανότητας ύπαρξης νεφών και επωφελούνται από την επιλογή σταθμών σε διαφορετικά ημισφαίρια. Η κύρια συμβολή των προτεινόμενων αλγορίθμων είναι ότι εγγυώνται μια ελάχιστη διαθεσιμότητα ανά μήνα, η οποία δεν είναι απαραιτήτως η ίδια για κάθε μήνα και, χρησιμοποιώντας σταθμούς απο διαφορετικά ημισφαίρια, ελαχιστοποιούν τον αριθμό των επίγειων σταθμών που χρειάζονται για να επιτευχθεί η επιθυμητή διαθεσιμότητα. Τέλος, προτείνεται ένας αλγόριθμος βελτιστοποίησης για τον υπολογισμό του αναγκαίου αριθμού των ενεργών σταθμών ανά μήνα, σε ένα δίκτυο επίγειων οπτικών σταθμών.

ΚΕΦΆΛΑΙΟ 7   ΜΟΝΤΕΛΟΠΟΙΗΣΗ   ΔΙΑΔΟΣΗΣ   ΟΠΤΙΚΟΥ   ΣΗΜΑΤΟΣ   –   ΑΤΜΟΣΦΑΙΡΙΚΟΙ ΣΤΡΟΒΙΛΙΣΜΟΙ

Το κεφάλαιο αυτό επικεντρώνεται στην ανάπτυξη μοντέλων για τη διάδοση του οπτικού σήματος κάτω από συνθήκες διάδοσης χωρίς νέφη, λαμβάνοντας υπόψη το φαινόμενο των ατμοσφαιρικών στροβιλισμών. Τα αποτελέσματα των μεθοδολογιών που παρουσιάζονται σε αυτό το κεφάλαιο, συγκρίνονται με πραγματικά δεδομένα από το οπτικό δορυφορικό πείραμα ARTEMIS.

Αρχικά, στο υποκεφάλαιο 7.1, παρουσιάζεται μια ανασκόπηση του πειράματος ARTEMIS. Στα πλαίσια του πειράματος αυτού υπάρχουν διαθέσιμες μετρήσεις λαμβανόμενης ισχύος τόσο για την ανερχόμενη όσο και την κατερχόμενη ζεύξη μεταξύ του επίγειου οπτικού σταθμού του Ευρωπαϊκού Διαστημικού Οργανισμού (European Space Agency, ESA) στην Τενερίφη, Ισπανία σε υψόμετρο 2.4 km, και του γεωστατικού δορυφόρου ARTEMIS. Το μήκος κύματος που χρησιμοποιείται στην ανερχόμενη ζεύξη είναι 847nm, ενώ στην κατερχόμενη είναι 819nm.

Στο υποκεφάλαιο 7.2 παρουσιάζεται μια μεθοδολογία για τον υπολογισμό του παράγοντα μέσης λήψης σήματος (aperture averaging factor), για οπτικούς δέκτες με κεντρική σκίαση για κατερχόμενη ζεύξη. Σύμφωνα με την προτεινόμενη μεθοδολογία ο παράγοντα μέσης λήψης σήματος (aperture averaging factor) για οπτικούς δέκτες με κεντρική σκίαση δίνεται από τον παρακάτω τύπο:

$$A_{obscured} = \left(\frac{D^4 \cdot A(D) + d^4 \cdot A(d)}{\left(D^2 - d^2 \right)^2} \right) \tag{1.4}$$

όπου D (m) είναι η διάμετρος του δέκτη, d (m) είναι η διάμετρος της σκίασης και A είναι ο παράγοντας μέσης λήψης σήματος, χωρίς να λαμβάνεται υπόψη η κεντρική σκίαση.

Συνεχίζοντας, στο υποκεφάλαιο 7.3 προτείνεται μια μεθοδολογία για τη δημιουργία χρονοσειρών λαμβανόμενης ακτινοβολίας/ισχύος για ανερχόμενες οπτικές ζεύξεις γεωστατικών δορυφορικών συστημάτων, λαμβάνοντας υπόψη τις επιπτώσεις που δημιουργούν στη διάδοση του σήματος οι ατμοσφαιρικοί στροβιλισμοί και τα σφάλματα στόχευσης. Οι βασικές παραδοχές του προτεινόμενου μοντέλου είναι: α) εξετάζεται μόνο η ανερχόμενη δορυφορική ζεύξη με γεωστατικό δορυφόρο, β) Εφαρμόζεται η θεωρία Rytov και ο δείκτης διάθλασης της ατμόσφαιρας (refractive index) μοντελοποιείται σύμφωνα με το φάσμα Kolmogorov (Kolmogorov spectrum), γ) εξετάζονται ζεύξεις με γωνία ανύψωσης μεγαλύτερη των 20 μοιρών , δ) εξετάζεται μόνο η περίπτωση των ήπιων ατμοσφαιρικών αναταράξεων και ε) εξετάζεται η περίπτωση διάδοσης μίας μόνο γκαουσιανής δέσμης.

Η λαμβανόμενη ακτινοβολία δίνεται με την παρακάτω σχέση :

$$I_R(t,r,SL) = n_T n_R n_{Atm} \frac{2P_T}{\pi W_{LT}(SL)^2} \exp\left(\frac{-2\beta^2}{W_{ST}^2(SL)} \right) \exp(2\chi_n) \tag{1.5}$$

όπου n_T και n_r είναι η αποδοτικότητα του πομπού και του δέκτη αντίστοιχα (περιλαμβάνονται οι συνολικές απώλειες λόγω των οπτικών συστημάτων πομπού και δέκτη), n_{Atm} είναι η ατμοσφαιρική αποδοτικότητα, P_T είναι η ισχύς του πομπού, W_{LT} (m) είναι το άνοιγμα της δέσμης μετά από διάδοση απόστασης SL λαμβάνοντας υπόψη και την επίδραση των σπινθηρισμών του σήματος, στο $\exp\left(\frac{-2\beta^2}{W_{ST}^2(SL)} \right)$ λαμβάνονται υπόψη τα σφάλματα στόχευσης και η απόκλιση του κέντρου της δέσμης λόγω στροβιλισμών

37

(beam wander) ενώ στο $\exp(2\chi_n)$ λαμβάνεται υπόψη το φαινόμενο των ατμοσφαιρικών σπινθηρισμών. Η μοντελοποίηση του χ_n βασίζεται στη χρήση στοχαστικών διαφορικών εξισώσεων με fractional κίνηση Brown.

Στο Σχήμα 5 το προτεινόμενο μοντέλο συγκρίνεται με μεγάλη επιτυχία με δεδομένα από το πείραμα ARTEMIS.
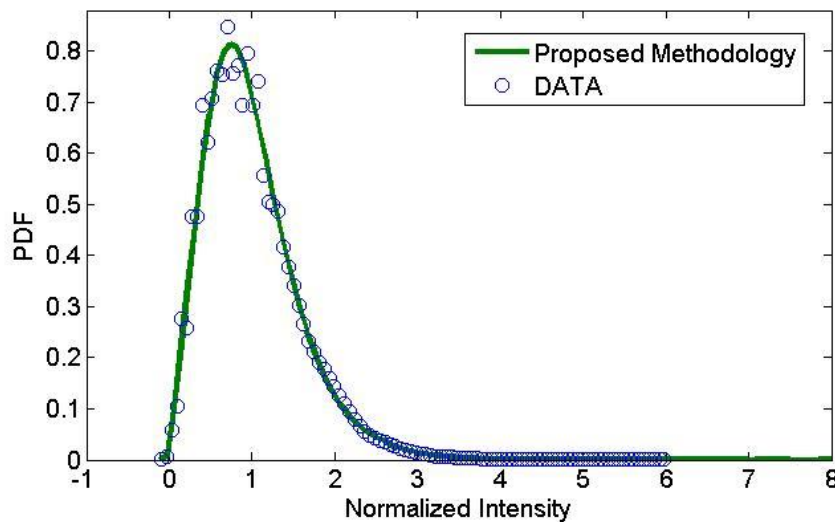
Σχήμα 5: Σύκριση προτεινόμενης μεθοδολογίας (συνεχής γραμμή) για τη δημιουργία χρονοσειρών λαμβανόμενης ακτινοβολίας με δεδομένα από το πείραμα ARTEMIS (κύκλοι)

ΚΕΦΆΛΑΙΟ 8   ΑΝΑΛΥΣΗ ΟΠΤΙΚΩΝ ΖΕΥΞΕΩΝ ΒΑΘΕΟΣ ΔΙΑΣΤΗΜΑΤΟΣ

Το κεφάλαιο αυτό επικεντρώνεται στο σχεδιασμό κατερχόμενης οπτικής ζεύξης βαθέος διαστήματος (Deep Space) σε συνθήκες διάδοσης χωρίς νέφη και στην ανάπτυξη μιας μεθοδολογίας για την επιλογή των παραμέτρων σηματοδότησης (ρυθμός κωδικοποίησης, διάρκεια συμβόλου κ.α.) της οπτικής ζεύξης με σκοπό την επίτευξη του μέγιστου ρυθμού μετάδοσης δεδομένων (data rate) με βάση τις συνθήκες της ζεύξης σύμφωνα με τα νέα πρότυπα που παρουσιάζονται στο [CCSDS17b].

Για τη μοντελοποίηση των συστημάτων αυτών, θεωρούμε κανάλι διάδοσης Poisson, και χρησιμοποιούμε σχήμα διαμόρφωσης έντασης (Intensity Modulation, IM) και απευθείας ανίχνευσης (Direct Detection, DD) [CCSDS17b]. Επιπλέον, σχετικά με τη σηματοδοσία, προτείνεται η χρήση διαμόρφωσης θέσης παλμού (Pulse Position Modulation, PPM) και η κωδικοποίηση με χρήση σειριακών συνελικτικών κωδίκων (serial concatenated convolutional codes). Τέλος, η ανάλυση επικεντρώνεται στη χρήση ανιχνευτών μέτρησης μεμονωμένων φωτονίων (single photon counting detectors).

Πιο συγκεκριμένα, στο υποκεφάλαιο 8.1 παρουσιάζεται η PPM διαμόρφωση και οι SCs κώδικες. Παράλληλα, παρατίθενται και αναλύονται οι παράμετροι που απαιτούνται για τον υπολογισμό του

προϋπολογισμού ισχύος μιας οπτικής δορυφορικής ζεύξης βαθέος διαστήματος, όπως παρουσιάζονται στο παρακάτω σχήμα:
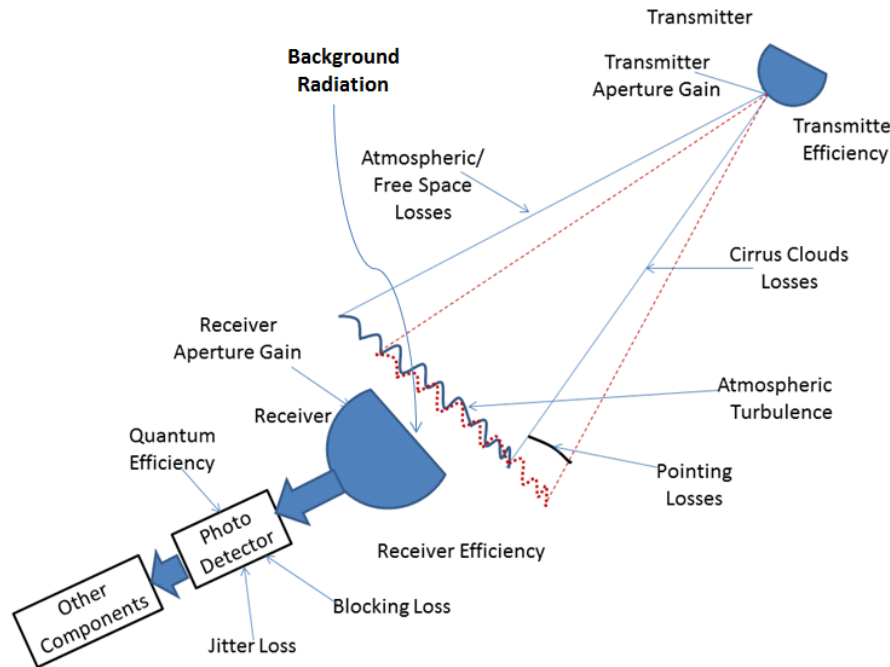
Σχήμα 6 Παράμετροι που απαιτούνται για το υπολογισμό του προϋπολογισμού ισχύος μιας οπτικής δορυφορικής ζεύξης βαθέος διαστήματος

Δίνονται πλήρεις εκφράσεις για τον υπολογισμό της ισχύος του σήματος, καθώς και της ισχύος θορύβου που λαμβάνει και ανιχνεύει ο οπτικός δέκτης.

Στο υποκεφάλαιο 8.2 δίνονται ακριβείς εκφράσεις για τον υπολογισμό της χωρητικότητας (Capacity) του οπτικού διαύλου, του ρυθμού λανθασμένων συμβόλων (Symbol Error Rate, SER) και του ρυθμού λανθασμένων bit (Bit Error Rate, BER).

Στο υποκεφάλαιο 8.4 παρατίθεται η προτεινόμενη μεθοδολογία για την επιλογή των παραμέτρων σηματοδότησης (ρυθμός κωδικοποίησης, διάρκεια συμβόλου κ.α.) της οπτικής ζεύξης. Τέλος, στο υποκεφάλαιο 8.5 χρησιμοποιώντας την προτεινόμενη μεθοδολογία παρουσιάζονται αριθμητικά αποτελέσματα για διάφορα σενάρια συστημάτων βαθέος διαστήματος.

ΚΕΦΆΛΑΙΟ 9   ΣΥΜΠΕΡΑΣΜΑΤΑ

Στο κεφάλαιο αυτό παρουσιάζεται μια σύνοψη των μεθοδολογιών που αναπτύχθηκαν στο πλαίσιο της παρούσας Διδακτορικής Διατριβής και δίνονται προτάσεις για μελλοντική έρευνα.

Ανακεφαλαιώνοντας, στο Κεφάλαιο 3 της παρούσας Διδακτορικής Διατριβής παρουσιάζεται η μεθοδολογία που αναπτύχθηκε για την παραγωγή χρονοσειρών δισδιάστατων και τρισδιάστατων πεδίων του Κάθετου Ολοκληρώματος της Περιεκτικότητας σε Υγρό Νερό (ILWC) των νεφών. Η προτεινόμενη μεθοδολογία λαμβάνει υπόψη τόσο την χρονική όσο και χωρική συσχέτιση του ILWC και επωφελείται από τη χρήση πολυδιάστατων στοχαστικών διαφορικών εξισώσεων για τη δημιουργία χρονοσειρών.

Στο Κεφάλαιο 4 παρουσιάζονται οι μεθοδολογίες που αναπτύχθηκαν για τον υπολογισμό και την πρόβλεψη της εξασθένησης του σήματος λόγω νεφών και της πιθανότητας για οπτική ζεύξη χωρίς νέφη (CFLOS), τόσο για μεμονωμένες όσο και για πολλαπλές ζεύξεις (διαφορισμός θέσης, από κοινού στατιστικά χαρακτηριστικά).

Στο Κεφάλαιο 5 παρουσιάζεται ένα νέο μαθηματικό μοντέλο για τον θεωρητικό υπολογισμό και την πρόβλεψη της πιθανότητας CFLOS, τόσο για μεμονωμένη οπτική δορυφορική ζεύξη όσο και για πολλαπλές χωρικά συσχετισμένες οπτικές δορυφορικές ζεύξεις.

Στο Κεφάλαιο 6 παρουσιάζονται οι αλγόριθμοι βελτιστοποίησης, που αναπτύχθηκαν στο πλαίσιο της παρούσας Διδακτορικής Διατριβής, για την επιλογή των οπτικών σταθμών βάσης, που σχηματίζουν ένα συνδεδεμένο δίκτυο για την αντιμετώπιση της νεφοκάλυψης. Οι αλγόριθμοι βελτιστοποίησης που προτείνονται λαμβάνουν υπόψη τη μηνιαία διακύμανση της νεφοκάλυψης και εκμεταλλεύονται τις μηνιαίες διαφορές μεταξύ βόρειου και νότιου ημισφαιρίου.

Στο Κεφάλαιο 7 παρουσιάζονται οι μεθοδολογίες που αναπτύχθηκαν για τη διάδοση του οπτικού σήματος κάτω από συνθήκες διάδοσης χωρίς νέφη, λαμβάνοντας υπόψη το φαινόμενο των ατμοσφαιρικών στροβιλισμών. Για τη μελέτη αυτή γίνεται ανάλυση των μετρήσεων από το οπτικό δορυφορικό πείραμα ARTEMIS.

Τέλος στο Κεφάλαιο 8 παρουσιάζεται μια μεθοδολογία για τον υπολογισμό του προϋπολογισμού ισχύος οπτικής ζεύξης για ζεύξεις βαθέος διαστήματος και προτείνεται μια νέα μέθοδος για την επιλογή των παραμέτρων σηματοδότησης (ρυθμός κωδικοποίησης, διάρκεια συμβόλου κ.ά.) της οπτικής ζεύξης.

Με βάση τα αποτελέσματα και τους περιορισμούς των μοντέλων που αναπτύχθηκαν στο πλαίσιο της παρούσας Διδακτορικής Διατριβής, μπορούν να προταθούν διάφορες δράσεις για μελλοντική έρευνα, όπως παρουσιάζεται ακολούθως.

Αρχικά, όσον αφορά το χωρο-χρονικό μοντέλο που προτείνεται στο τρίτο κεφάλαιο για τη δημιουργία χρονοσειρών ILWC, για την ενσωμάτωση της χρονικής συσχέτισης του ILWC, χρησιμοποιούνται οι ετήσιες παράμετροι από τη σύσταση ITU-R P. 1853 [ITU1853-1]. Βασιζόμενοι στο έκτο κεφάλαιο, το οποίο επικεντρώνεται στην μηνιαία μεταβλητότητα του ILWC, μπορεί να διεξαχθεί

έρευνα για τη χρονική εξέλιξη του ILWC για κάθε μήνα ξεχωριστά ή ανάλογα με την πιθανότητα εμφάνισης ILWC μεγαλύτερη από το μηδέν (πιθανότητα κάλυψης από νέφος).

Επιπρόσθετα, οι σχέσεις που χρησιμοποιούνται στο χωρο-χρονικό μοντέλο τριών διαστάσεων του ILWC για την κατακόρυφη έκταση των νεφών και το ύψος της βάσης τους είναι γενικές. Δεδομένου ότι οι σταθμοί, που βρίσκονται σε μεγάλο υψόμετρο έχουν εξέχουσα σημασία για τα συστήματα οπτικών δορυφορικών επικοινωνιών, μελέτες σχετικά με το ύψος της βάσης των νεφών και την κατακόρυφη έκταση τους, ειδικά για σταθμούς που βρίσκονται σε μεγάλο υψόμετρο, παρουσιάζουν μεγάλο ενδιαφέρον.

Συνεχίζοντας με τους αλγόριθμους βελτιστοποίησης που προτάθηκαν στην παρούσα Διδακτορική Διατριβή για την επιλογή των οπτικών σταθμών βάσης για συστήματα οπτικών δορυφορικών επικοινωνιών, τόσο με γεωστατικούς δορυφόρους όσο και με δορυφόρους μέσης τροχιάς, για την υλοποίηση τους υποθέτουμε συγκεκριμένο λίστα με σταθμούς ή η Γη χωρίζεται σε συγκεκριμένες περιοχές. Μια ενδιαφέρουσα επέκταση θα ήταν η διαστασιολόγηση του οπτικού συνδεδεμένου δικτύου χωρίς να χωρίζεται η Γη σε συγκεκριμένες περιοχές, αλλά χρησιμοποιώντας ολόκληρη τη Γη ως πιθανούς σταθμούς.

Τέλος, δεδομένου ότι οι οπτικές επικοινωνίες είναι ελκυστικές για συστήματα δορυφορικών επικοινωνιών, με δορυφόρους μέσης και χαμηλής τροχιάς, πρέπει να αναπτυχθούν μεθοδολογίες για τον υπολογισμό της λαμβανόμενης ισχύος, λαμβάνοντας υπόψη τις επιδράσεις των στροβιλισμών για τις περιπτώσεις αυτές. Πρέπει να σημειωθεί ότι τα οι επιδράσεις των στροβιλισμών είναι διαφορετικές στην περίπτωση συστημάτων δορυφορικών επικοινωνιών με δορυφόρους μέσης και χαμηλής τροχιάς, από την περίπτωση συστημάτων με γεωστατικούς δορυφόρους .

1   INTRODUCTION

The increasing demand for high speed internet, multimedia and broadband applications in accordance with the ever growing amount of data that each user transmits has revealed the necessity for higher data rates and large bandwidth. According to [EU Broadband] in 2010 the European Union (EU) set 3 goals for broadband internet: a) all Europeans are provided with basic broadband (up to 30 Megabits per second, Mbps) by 2013 (achieved), b) all Europeans are provided with fast broadband (over 30 Mbps) by 2020 and c) the ultra-fast broadband (over 100 Mbps) for more than 50% of Europeans by 2020.

Even there is progress regarding the EU goals not all the Europe 2020 targets will be met [EU Broadband]. In order to try to reach these goals and in particular to make it financially affordable, satellite communications can play a key role, especially in sparsely populated, rural and remote areas. Although, satellite solutions have the advantage of covering these demands over a wide geography, in order to stay competitive with terrestrial solutions, it is necessary to push the limits of the offered capacity.

Current state-of-the-art satellite technology are the High Throughput Satellites (HTS) with multi-beam antennas, offering capacity of about 70-100 Gbps. It is estimated that next generation HTS satellites will require a capacity of one Terabit/s (1000 Gbps) by 2020. In the next two Figures the Global GEO and Non-GEO HTS Bandwidth demand by Application, according to the market study conducted by NSR [NSR15] are exhibited.
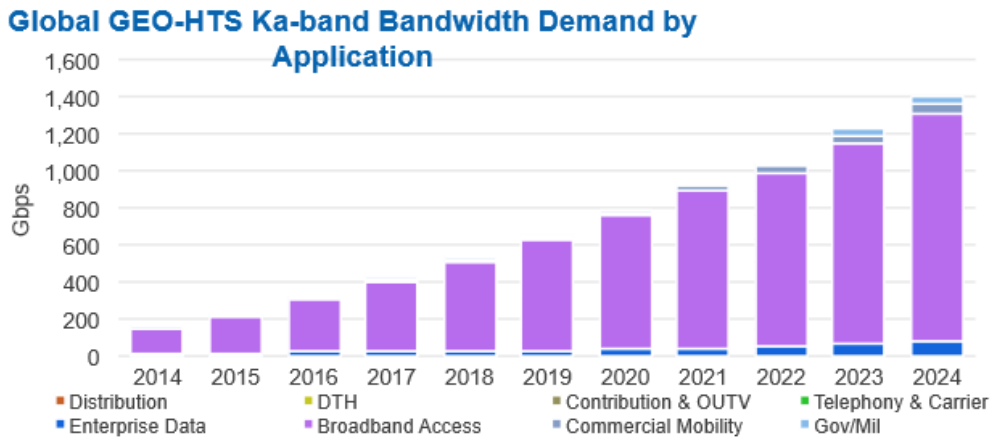
Fig. 1: Global Ka-band GEO HTS Bandwidth Demand by Application (source [NSR15])

Fig. 2: Global Non-GEO HTS Bandwidth Demand by Application (source [NSR15])

To meet these demands due to the limited spectrum of about 2GHz in Ka band [26.5-40 GHz], the new designed high throughput satellite communication systems are shifting to higher frequency bands. A potential solution is the use of Q/V [33-75GHz] and W [75-110 GHz] band where much larger bandwidth is available. Another prominent solution is the employment of optical carrier frequencies for satellite communication systems [Kaushal17], [Toyoshima06]. At optical range, very large bandwidth can be used with no limitations since there is no spectrum congestion.

The use of optical wavelengths exhibit a great variety of advantages [Hemmati09], [Kaushal17]: (a) reduced mass, power and volume of equipment, compared to the satellite systems operating in Radio Frequency (RF) bands is needed, (b) Optical band has 100 to 1000 times more available bandwidth than all of the RF bands, (c) although there are some radiation limitations due to eye- safety issues, optical bands need no frequency regulation due to the highly directive antennas, (d) the light beam can be very narrow, making optical links hard to be intercepted thus improving the system's security.

Optical satellite communication systems incorporate ground-to-satellite, satellite-to-ground, satellite-to-satellite (inter satellite) and ground/satellite to airborne platforms links. Note that space segment can incorporate Geosynchronous (GEO), Medium Earth Orbit (MEO), Low Earth Orbit (LEO) satellites nano satellites, high altitude platforms and unmanned aerial vehicles (UAVs) among others.

Since the employment of optical spectrum in satellite systems constitutes a promising vision, a variety of experimental missions has already been conducted with main purpose the feasibility analysis of optical satellite communication systems. Detailed information for the majority of the campaigns that have already been conducted can be derived from [Kaushal17], [Romba04], [Toyoshima08]. Among these campaigns there are experiments between:

1)   Geosynchronous (GEO) satellites and OGSs:

a)	In 2001 ESA launched the ARTEMIS GEO satellite. Since 2003 bi-directional links between the ARTEMIS GEO satellite and the ESA's OGS in Tenerife, Spain with either ESA's Gourd terminal [Alonso04] or JAXA's LUCE ground terminal [Toyoshima05] has been established for the characterization of laser beam propagation through the atmosphere. Uplink and downlink propagation models have been developed using these measurements [Reyes04a], [Reyes04b]. In addition, for uplink transmission when ESA's ground terminal is used multi beam (up to 4 beams) transmission technique for mitigation of atmospheric turbulence is evaluated [Commeron05].

b)	the Ground/Orbiter Lasercomm Demonstration (GOLD) experiment which was one of the first bi-directional link experiments conducted between the Japanese ETS-VI spacecraft and the ground station at JPL's Table Mountain Facility, Wrightwood CA (2.2 km Altitude) [Wilson97a], [Wilson97b]. ETS-VI was planned to be a GEO stationary satellite but finally its orbit is highly elliptic rather than geostationary.

c) Experimental sessions conducted between the Communications Research Laboratory (CRL) in Tokyo Japan and the Japanese ETS VI satellite [Toyoda97] for the characterization of atmospheric turbulence. A great variety of methodologies for uplink/downlink propagation were evaluated using these measurements [Toyoshima96], [Toyoshima98], [Toyoshima00].

2)	Low Earth Orbit (LEO) satellites and OGS:

a)	the KODEN experiment between the National Institute of Information and Communications Technology (NICT) located in Koganei, Tokyo and the Optical Inter-orbit Communication Engineering Test Satellite (OICETS). OICETS is a LEO orbit satellite [Toyoshima06]. In KODEN experimental mission, multi beam transmission for the uplink propagation is evaluated among others [Toyoshima07b].

b)	the KIODO downlink experiment between the DLR OGS at Oberpfaffenhofen near Munich and the OICETS Japanese LEO satellite. Measurement campaigns executed during 2006 and 2009 [Giggenbach12], [Moll11], [Perlot07].

c)	the measurement campaign between the ESA's OGS at Tenerife using and the Near Field Infrared Experiment low earth orbiting spacecraft [Fields11].

d)	Recently, the SOTA experiment campaign was conducted using the SOCRATES micro LEO satellite and several OGSs [Petit16]. In this experiment the performance of adaptive optics technique for both uplink and downlink is evaluated.

3)	Satellites (Inter-Satellite links) like:

a)	the Semiconductor Inter satellite Link Experiment, SILEX, between the French LEO observation satellite SPOT4 and the ESA's GEO telecommunication satellite ARTEMIS [Tolker02] was one of the first inter satellite link experimental missions

b) An optical link between two LEO orbiting satellites, Terra SAR-X and NFIRE, at 5.5 Gbps on a total distance of 5500 km has been established in 2008 [Fields09].

4)   High Altitude Platforms (HAP) and OGS like:

a)   the measurement campaign took place at ESRANGE near Kiruna, Sweden, with a transportable optical ground station which is used as ground segment and a high altitude platform (HAP, stratospheric balloon) as space segment [Horwath06].

Nowadays, there is increased interest for LEO satellite to ground quantum key distribution (QKD). QKD uses individual light quanta in quantum superposition states to guarantee unconditional communication security between distant parties. Some first results and detailed information about LEO satellite to ground QKD experimental campaign can be derived from [Liao17], [Takenaka17].

Very recently, Laser Light Communications (www.laserlightcomms.com/) has announced the deployment of an all-optical global communications network including satellite elements (MEO satellites). Laser Light Communications intends to be the first Optical Satellite Service (OSS) provider of telecommunications solutions serving the high bandwidth data and next-generation service needs of carriers, enterprises and government agencies around the world based entirely on optical wave technology. The network will be connected to US-Patented StarBeam operating system [Brumley16] which is automated robust cognitive based computing system using Artificial Intelligence (AI) and Machine Learning (ML) algorithms to sense, predict, and infer network conditions and weather patterns [Brumley16]. The Laser Light Communications intends to offer a full network capacity of 33Tbps- 48 200Gbps inter satellite links and 72 customer service links of 200Gbps bi-directionally.

In addition, there is already increasing interest for the usage of optical communications in deep space missions [Hemmati11]. As deep space, distances beyond the Moon are considered. In the scientific literature (journals and conferences), there are many studies for the design of deep space communication links presenting simulation results for potential missions e.g. to Mars [Hemmati11]. Moreover, under the framework of NASA's Lunar Laser Communications Demonstration (LLCD) [Boroson14] project, it has been demonstrated the transmission of pulse modulation formats for shorter distances (Moon to Earth). It has been conducted a successful test on October 18, 2013, transmitting data between the spacecraft and its ground station on Earth at a distance of 385.000km. The same payload has also been proposed as payload for the Phobos and Deimos & Mars Environment (PADME) orbiter [Lee14].

In Fig. 3 the different types of space optical links are summarized as derived from [Hemmati11].
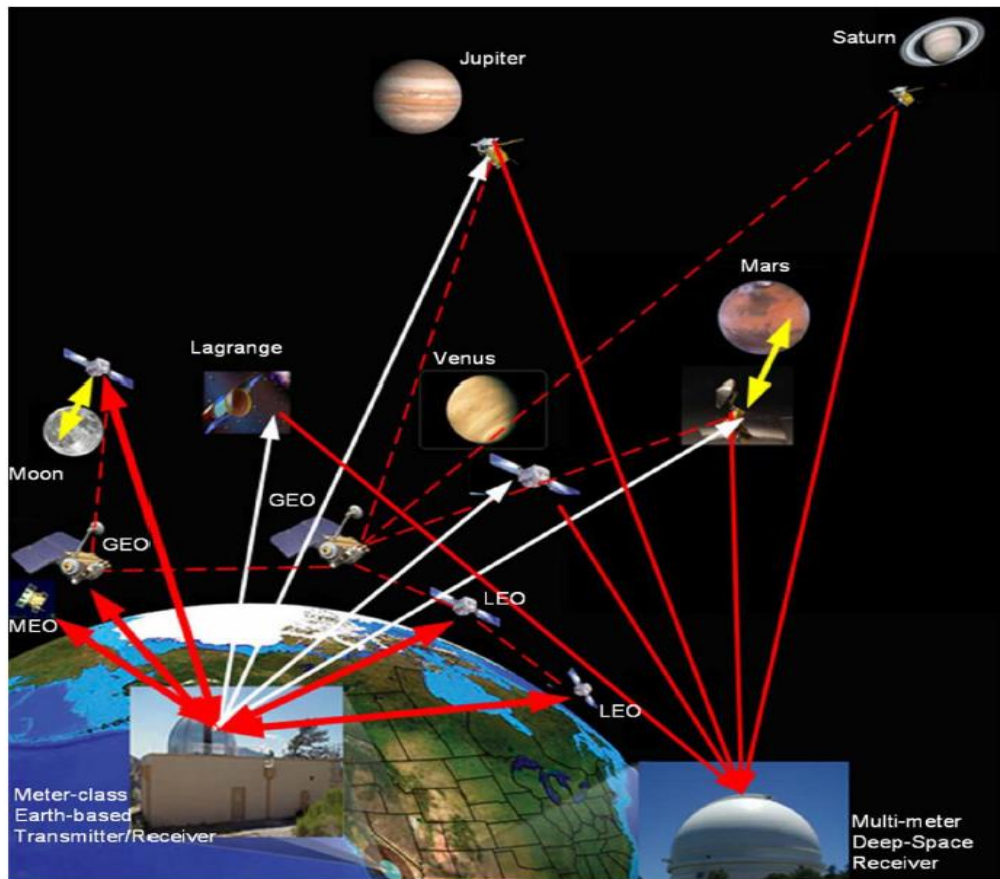
Fig. 3: Different Types of Space Optical Links (source: [Hemmati11])

It can be easily observed that optical frequencies constitute a promising solution for satellite communications systems. However, optical signal is affected by several atmospheric phenomena and mainly, but not limited to, by clouds and atmospheric turbulence. In the next section the phenomena that impair the optical beam for a satellite link are briefly reported.

2 PROPAGATION IMPAIRMENTS DUE TO ATMOSPHERE - LITERATURE REVIEW

When the optical signal propagates through the earth's atmosphere, it is affected by several atmospheric phenomena like atmospheric particles, liquid water clouds, cirrus clouds and atmospheric turbulence among others [Kaushal17], [CCSDS17a]. For the reliable design of optical satellite communication systems the effect of these phenomena should be accurately estimated. Among these phenomena, cloud coverage is the dominant fading mechanism. The attenuation induced by clouds can block the optical satellite link [Kaushal17], [CCSDS17a]. Even under Cloud Free Line of Sight (CFLOS) conditions, i.e. no clouds along the slant path, the optical beam is mainly affected by atmospheric turbulence [Kaushal17], [CCSDS17a].

In optical domain, the attenuation induced by the atmospheric phenomena can be so severe that mostly a fixed power margin as in RF cannot compensate the propagation impairments. Thus, several Fade Mitigation Techniques depending on the atmospheric phenomenon have been proposed like site diversity, transmitter diversity and transmission window selection etc. [Kaushal17], [CCSDS17a], [Hemmati11].

In this section the main atmospheric phenomena that degrade the optical signal are reported and methodologies for the prediction of their effects will be presented. Special attention will be given to the two major propagation factors, i.e. the cloud coverage and turbulence. In addition the proposed fade mitigation techniques for each case are briefly reported.

2.1.1 Transmittance of the atmosphere

The Earth's atmosphere is composed by molecules and aerosols. When the light beam propagates through the atmosphere both molecules and aerosols degrade the signal. The loss is mainly caused by the absorption and scattering and it is described by Beer's law [CCSDS17a], [Hemmati11], [Kaushal17]. For optical communications absorption is dominant. Absorption occurs when a photon is absorbed by atoms or molecules of the atmosphere resulting on the extinction of the incident photon, the heated of atmosphere and radiation emissions. Scattering of electromagnetic waves in visible and IR wavelengths is generally defined as the redirection of energy by air molecules and particles present along the propagation path. Light scattering is severely dependent of wavelength but the losses are not as severe as in absorption. The total atmospheric attenuation is expressed as the combination of absorption and scattering from both aerosols and molecules.

2.1.1.1 Molecules

The Earth's atmosphere is combined by different gasses which vary with the location on the Earth and the altitude over the sea level and interact with the optical beam resulting mainly on molecular absorption and Rayleigh scattering.

49

Molecular absorption is a highly frequency selective phenomenon. The strength of the absorption depends on the wavelength, the height, the pressure and the temperature as presented in Recommendation ITU-R P.1621 [ITU1621]. There are several software packages that are used for the estimation of this effect for the place of interest like LOWTRAN, FASCODE, MODTRAN, HITRAN, and SpectralCalc among others. These software packages take into account parameters like the altitude, the path length, the latitude and longitude of the place among others.

Rayleigh scattering takes place when the scatters (haze, molecules) have shorter physical diameter in comparison with the wavelength which is used. It is negligible for wavelengths greater than 0.8 μm and its magnitude has a wavelength dependence of λ^{-4}. At wavelengths below 1 μm, Rayleigh scattering produces the blue color of sky as a consequence that blue light is scattered much more than other visible wavelengths. The most significant consequence of Rayleigh scattering is the background noise into the receivers both for up-link and down-link [CCSDS17a], [Hemmati11], [Kaushal17].

2.1.1.2 Aerosols

Aerosols are natural and artificial atmospheric particles like water droplets and air pollutants respectively. The concentration, the distribution and the profile of aerosols change, depending on the altitude and the characterization of the place (rural, marine, urban, desert, etc.) [CCSDS17a], [Hemmati11], [Kaushal17]. Moreover, volcanic asses can be observed during volcanic eruptions. As in molecular absorption, aerosol absorption can be computed through software packages.

Mie scattering takes place when scatterers have the same physical diameter in comparison with the wavelength of the radiation. According to Mie theory, Mie scattering depends on the wavelength, the concentration, the size and the distribution of the particles. In ITU-1621 [ITU1621] a formula for the computation of Mie scattering is given.

2.1.2 Transmission Windows

In optical satellite communication systems, the wavelength range is chosen to have maximum transmittance and since absorption is dominant, to have minimum absorption. This is known as atmospheric transmission window. There are several transmission windows within the range of 700 - 1600 nm [CCSDS17a], [Hemmati11], [Kaushal17]. In Fig. 4 the transmittance of the atmosphere versus the wavelength is reported. The transmission window close to 1550nm can be easily seen that the transmittance is above 0.9. Additionally, in order the transmittance is higher, high altitude stations are chosen.
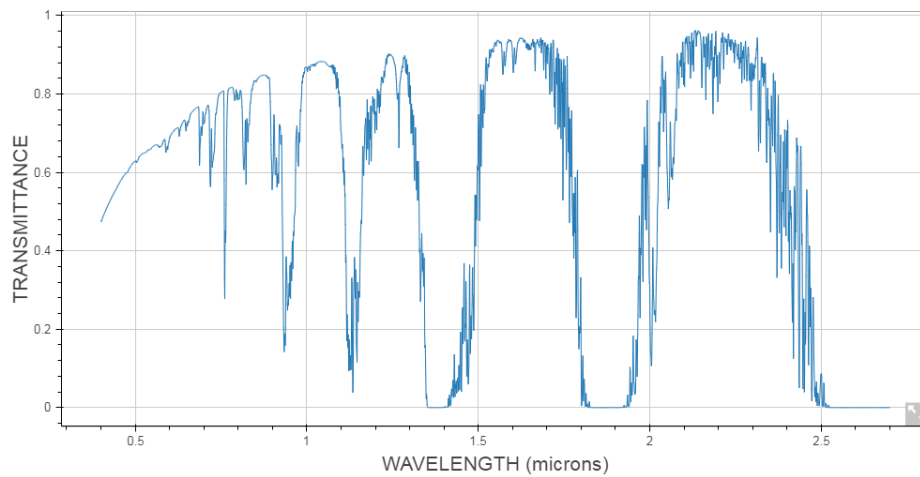
Fig. 4: Transmittance vs Wavelength

2.2 Clouds

Clouds are aerosols which are made from water droplets or ice crystals which are dispersed in atmosphere. They can be classified according to the altitude of their base above Earth's surface as exhibited in the next table [Luini16]:

Table 1: Clouds Classification

High clouds	Cirrus, Cirrocumulus, Cirrostratus
Vertical clouds	Cumulonimbus, Cumulus
Middle clouds	Altostratus, Altocumulus
Low clouds	Stratus, Stratocumulus, Nimbostratus

For the prediction of the effect of clouds in optical signal two major categories will be distinguished: the water clouds where low middle and vertical clouds are incorporated and the ice clouds where high clouds are included.

2.2.1 Ice clouds

Ice clouds are thin semitransparent clouds in very high altitude. Their base ranges from 5-13 km at mid-latitudes, which are mainly composed by ice crystals of different shapes. Cirrus clouds present less than 50% of the time at a given location [Degnan93]. In [Degnan93] a formula based on cirrus thickness for the computation of ice clouds attenuation is introduced.

51

2.2.2   Water Clouds

Water clouds are mainly composed by suspended water particles and contain the most restrictive factor for the optical communications. The presence of clouds induce hundreds dB/km and as a consequence this phenomenon prohibits the propagation of optical signal. The attenuation induced by clouds can be computed according to the next expression taking in to account the microphysical properties of clouds [Luini16]:

$$A_{WaterClouds}(\lambda) = \int_{L_0}^{L_{max}} \beta_{ext}(\lambda) dx \tag{1}$$

$A_{WaterClouds}(\lambda)$ is the attenuation due to clouds, L_0 , L_{max} are the lower and upper bound of slant path and $\beta_{ext}(\lambda)$ is usually referred to as volume extinction coefficient and is typically expressed in dB/km. Because of water clouds synthesis, the shape of particles can be considered as spherical and $\beta_{ext}(\lambda)$ is given according to next expression [Luini16]:

$$\beta_{ext}(\lambda) = 4.343 \times 10^3 \int_0^\infty \sigma_{ext}(r,\lambda) n(r) dr \tag{2}$$

where *n(r)* is the clouds particle size distribution and σ_{ext} is the extinction cross section calculated with the employment of the classical scattering Mie Theory [Bohren], [Ishimarou78] and there are also available free software tools for these calculations [scattport]. Detailed information for particle size distribution can be derived from [Luini16].

The attenuation induced by clouds is so high that the blockage of the link can be simply considered only with the cloud coverage. Thus, for the reliable design of an optical satellite communication system cloud coverage statistics and methodologies for the estimation of CFLOS for a particular place are needed. These methodologies should take into account the temporal and spatial variability of clouds among others.

To continue in the next 2 sub sections methodologies related to cloud coverage are reported. In the first one, methodologies for the estimation of CFLOS for an OGS and an OGSN based on cloud coverage statistics are reported. In the second one information about modeling of clouds using Integrated Liquid Water Content statistics are presented. Additionally, in the third sub section, information about the monthly and hemisphere variability of cloud coverage is reported. This variability is proved really crucial for the design of an optical satellite communication system. Finally in the fourth sub section optimization algorithms for OGS selection for site diversity technique are reported.

2.2.2.1 CFLOS Modeling

In optical satellite communication systems the blockage of the link is caused with the presence of clouds along the slant path. Thus, an on/off channel with cloud coverage is assumed [Perlot12]. In the related literature, several research studies have been published for the estimation of CFLOS probability for both a single OGS and an OGS network (OGSN). The CFLOS probability for a single link is defined as the probability of the optical link is not blocked by clouds, while the CFLOS probability of the OGSN is defined as the probability that at least one of the OGSs forming the OGSN is not blocked by clouds. The majority of these methodologies use cloud mask (coverage) data derived from Earth observation satellites. Earth observation satellites provide cloud mask data in a binary basis i.e., cloudy/non cloudy conditions with a specific temporal and spatial resolution. Using such data the probability of cloud coverage for each OGS of interest is calculated.

According to [Perlot12] and [Net16] the on/off optical channel for each OGS separately can be modeled as a binary variable X_i according to the Bernoulli distribution:

$$X_i \approx B(p_{cloud}^i) = \begin{cases} 1 & , \text{w.p. } p_{cloud}^i \\ 0 & , \text{w.p. } 1 - p_{cloud}^i \end{cases} \tag{3}$$

1 means that the OGS i is blocked by clouds with probability p_{cloud}^i (derived from meteorological data bases) and 0 that there is no cloud coverage with probability $1 - p_{cloud}^i$. In [Perlot12] and [Net16] mathematical formulations for the estimation of ground station availability for single links and diversity scenarios for uncorrelated and correlated ground stations are given. In [Net16] the elevation angle of the links is taken into account among others. In addition in [Portillo17] CFLOS for a single link and an OGSN is estimated employing a Gilbert-Eliot model. In this case in accordance with the cloud mask statistics, cloud coverage duration statistics is also employed.

In the majority of these research items the spatial correlation of cloud coverage between the stations for an OGSN is modeled by an exponential expression [Perlot12]:

$$\rho_{cloud\_coverage}(d) = e^{-(d/d_0)} \tag{4}$$

where d (km) is the distance between two stations and d_0 (km) is the cloud coverage correlation distance, typically it takes values between 300 and 500 km.

For stations with separation distance larger than d_0 it can be assumed that the stations are uncorrelated

2.2.2.2 ILWC Modeling

Cloud coverage can be modeled employing clouds' Integrated Liquid Water Content (ILWC) statistics. ILWC denotes the vertical integral of the Liquid Water Content (LWC) of clouds. LWC in (g/m^3)

is a measure of the mass of the water in the cloud. Thus, in order to have clouds, ILWC has to be greater than zero. Consequently, for ILWC>0 there is cloud coverage and for optical satellite communication systems, it can be assumed that the link is blocked. As adopted in ITU-R P.840 [ITU840] and also studied in detail in [Jeannin08] ILWC long term annual statistics can be sufficiently described by lognormal distribution. In ITU-R P. 1853-1 [ITU1853-1] a methodology for the generation of ILWC time series correlated on temporal domain is presented. This methodology incorporates the time evolution of ILWC but not the spatial variation. According to ITU-R P.1853-1 [ITU1853-1] ILWC time series for a specific point are given according to the next formula:

$$L(t) = \begin{cases} \exp\left[Q^{-1}\left(\frac{1}{P_{CLW}} Q\big(G(t)\big) \right) \times \sigma + m \right] & G(t) \geq \alpha_{th} \\ 0 & G(t) \leq \alpha_{th} \end{cases} \tag{5}$$

where the mean value (m), the standard deviation (σ) and the probability of cloud coverage (P_{clw}) for each place of interest (OGS) are the statistical parameters of $ln(L)$ and they can be derived from meteorological databases like ERA-Interim, ITU-R P.840-6 [ITU860-6] etc. $Q(\ )$ is the well-known Gaussian Q-function from the communication theory and a_{th} is the truncation threshold of the correlated Gaussian noise given from the following expression $\alpha_{th} = Q^{-1}(P_{CLW})$. For the synthesis of Gaussian noise G detailed information can be derived from ITU-R P.1853-1.

Recently, in [Luini14], a methodology (Stochastic Model of Clouds) for the synthesis of 3D spatially correlated cloud fields is proposed. In [Luini14] employing Earth Observation data an expression for the vertical profile of LWC within the cloud is developed. The vertical profile of LWC can be given according to the next expression:

$$\tilde{w}(h) = \begin{cases} \dfrac{L}{(c^2)^{c^1} \Gamma(c^1)} \left(h - h_0\right)^{c^1-1} e^{-(h-h_0)/c^2} & \text{for } h \geq h_0 \\ 0 & \text{for } h < h_0 \end{cases} \tag{6}$$

$$c^1 = 4.27\, e^{-4.93(L+0.06)} + 54.12\, e^{-61.25\,(L+0.06)} + 1.71$$
$$c^2 = 3.17\,(c^1)^{-3.04} + 0.074$$

In the above equations $\tilde{w}(h)$ in g/m^3 is the Liquid Water Content depending on the vertical height, h in km is the vertical height of cloud, h_0 in km is the cloud base height, L in mm is the ILWC, $\Gamma(\ )$ is the Gamma function and c^1, c^2 are the parameters that regulate the shape of $\tilde{w}(h)$.

Additionally, in [Luini12] to generate cloud fields start from the generation of random Gaussian fields, whose spatial correlation $\rho_G(d)$ is given according to the next formula (data from MODIS database has been used):

$$\rho_G(d) = 0.35\,e^{-\frac{d}{7.8}} + 0.65\,e^{-\frac{d}{225.3}}, \ d(km) \tag{7}$$

2.2.2.3   Monthly/Hemisphere Variability

Cloud coverage is highly seasonal and monthly dependent. Even for regions which are favourable for optical communications (low cloud coverage among others) the percentage of cloud coverage greatly depends on the month and season. Moreover, significant differences can be identified between stations that are located in different hemispheres. For example, in Fig. 5 the cloud coverage per month (monthly variability) for year 2009 for one station in north hemisphere, Madrid Spain, and another in south hemisphere Santiago, Chile is presented.
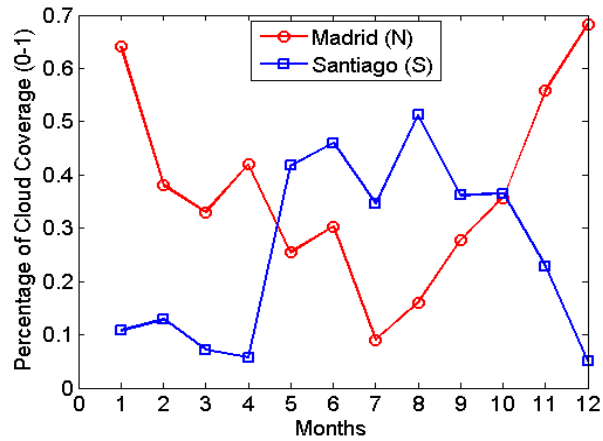
Fig. 5: Percentage of cloud coverage (0-1) for year 2009 for Madrid (North Hemisphere) and Santiago (South Hemisphere)

2.2.2.4   Mitigation of Cloud Coverage/ OGSN Optimization

For the mitigation of cloud coverage, site diversity (large scale diversity) [Panagopoulos04] technique has been proposed [Hemmati11], [Kaushal17]. Multiple optical ground stations (OGSs) dispersed in large distances, in order clouds can be considered as uncorrelated, are employed to guarantee the desired availability of the system. These OGSs are forming an optical ground station network (OGSN). Important for the design of an optical satellite communication system is the optimum selection of the locations of the stations that will form the OGSN.

In [Fuchs15], methodologies for the optimum selection of OGSs for an OGSN taking in to account the spatial correlation of cloud coverage and the probability of cloud coverage for each OGS are defined. To continue, in [Portillo17] a novel methodology for the determination of the optimal OGS location for a LEO system is presented. In this paper except from the cloud statistics, the latency and infrastructure models are also used to evaluate the OGS selection.

2.3   Turbulence

Under cloud free line of sight conditions the dominant phenomenon that degrades the optical signal is the atmospheric turbulence. Atmospheric turbulence comes from the variations of the temperature, the wind speed and the pressure along the propagating path. The energy firstly introduced creates turbulence of size L_0 (outer-scale). Then the large eddies create smaller eddies until they reach a size called the inner scale (l_0). When the turbulent size is lower than l_0 the energy is dissipated and eddies disappear [Andrews05]. Therefore, three ranges of turbulence are identified according to the size of eddies:

- Input range: the size is larger than L_0

- Inertial sub range: the size is between L_0 and l_0

- Dissipation range: size smaller than l_0

Turbulence and the irregularities of the refractive index are characterized by the structure function of the refractive index and the spatial spectrum of refractive index $\Phi_n(\kappa)$. Turbulence is considered, in general, locally homogeneous and its power spectrum can be described with close form for the inertial and dissipation ranges. In the input range, turbulence is considered as anisotropic. There is a great variety of models for spatial spectrum of refractive index like the Kolmogorov, the Tatarskii, the modified von-Karman among others, which are presented in [Andrews05], [Hemmati11]. Here the expression for the well-known and commonly used spatial spectrum of refractive index given by Kolmogorov is exhibited [Andrews05]:

$$\Phi_n(\kappa) = 0.033 C_n^2 \kappa^{-11/3}, \frac{1}{L_0} \le \kappa \le \frac{1}{l_0} \tag{8}$$

C_n^2 is the structure constant of the refractive index. This parameter is of prominent importance as it determines the strength of turbulence. C_n^2 depends on the time of day, the location of the link the wind speed and the height above sea level, among others. Since C_n^2 changes with height, for satellite communications, it has to be integrated over the propagation path i.e., from height of the receiver above sea level to the top of the atmosphere (20km assumed). C_n^2 and consequently turbulence effects are higher near the ground level and decreases with the height. Several models based on measurements campaigns have been proposed [Andrews05], [Kaushal17]. For satellite applications the most commonly used is the Hufnagel Valley Boundary model for vertical links [Andrews05], [Hemmati11], [Kaushal17].

$$C_n^2(h) = 0.00594 \left(\frac{w_{rms}}{27}\right)^2 (10^{-5}h)^{10} \exp\left(-\frac{h}{1000}\right) + 2.7x10^{-16}$$
$$\exp\left(-\frac{h}{1500}\right) + A_0 exp\left(-\frac{h}{100}\right) \tag{9}$$

where w_{rms} is the RMS value of wind speed in m/s, h the height above mean sea level in meters and $A_0(m^{-2/3})$ is the nominal value of $C_n^2(h)$ at ground level. A varies depending on the site conditions the time during the day, etc. For the calculation of the RMS wind speed the Bufton model can be used [Andrews05].

In [Giggenbach12] a modification of Hufnagel Valley Boundary model is introduced to take the ground station into account:

$$C_n^2(h) = A_0 \exp(-H_{GS}/700)\exp(-(h-H_{GS})/100) +$$
$$+ 5.94 \times 10^{-53} \times (\frac{w_{rms}}{27})^2 h^{10}\exp(-h/1000) + 2.7 \times 10^{-16}\exp(-h/1500)$$

(10)

where H_{GS} (m) is the altitude of the ground station.

Turbulence results on scintillation and the beam effects like the beam wander, beam spreading and beam jitter. The effect of these phenomena varies between uplink and downlink propagation. Additionally, significant differences are also identified in the case that as space segment a GEO satellite is used, comparing to the case that either a LEO or a MEO satellite is used.

For satellite communications 3 different wave fronts (plane wave, spherical wave, Gaussian beam) are used [Hemmati11], [Andrews05]:

- Plane wave: The approximation of plane wave is used in applications where the turbulent layers are in the far field. Thus this approximation is mainly used for the downlink (satellite to ground).

- Spherical wave: The approximation of spherical wave is associated with a point source. This approximation can be used for uplink propagation.

- Gaussian Beam: This kind of waves is mainly used in satellite communication systems and especially in uplink propagation. Gaussian beams approximate sufficiently the propagation properties of the wave especially when focusing and diverging characteristics are important. As the Gaussian beams are used in this thesis, some useful expressions are reported. The transmitted Gaussian wave (the transmitting aperture is located in the plane *z =0*) is defined as [Andrews05]:

$$U_0(\mathbf{r},0) = a_0 \exp\left(-r^2/W_0^2 - ikr^2/\left(2F_0^2\right)\right)$$

(11)

r (m) is the distance from the beam center, W_0 (m) is the effective beam wave radius, at which the field falls to *1/e* of the maximum, *k* is the optical wave number related to the optical wavelength, a_0 [$(W/m^2)^{1/2}$] is the amplitude of the field at *z=0* [Andrews05] and F_0 (m) is the radius of curvature. Three kinds of Gaussian beam waves can be identified according to the values of F_0 [Andrews05]. For the uplink satellite applications collimated

beam wave ($F_0 \rightarrow \infty$) is preferred. Moreover, the received irradiance of a collimated Gaussian beam after propagation of distance S*L* (*m*) (slant path) is given according to the next expression:

$$I(r, SL) = \frac{2P_T}{\pi W(SL)^2} \exp\left(\frac{-2r^2}{W^2(SL)}\right) \qquad (12)$$

P_T (W) is the total beam power, and *W(L)* is the beam waist in meters after a propagation distance *L*, given by the next expression:

$$W^2(SL) = W_0{}^2 \left[1 + \left(\frac{\lambda \cdot SL}{\pi \cdot W_0{}^2} \right)^2 \right] \qquad (13)$$

λ(*m*) is the wavelength used. In these expressions the refraction and diffraction of Gaussian beam are included [Andrews05].

In addition, the coherence length of the atmosphere or Fried parameter as it is also called r_0 (*m*) and the isoplanatic angle θ_0 (rad) are two metrics which give important information for turbulence effects. Both metrics depend on the wave front used, the elevation angle of the link, the structure constant of the atmosphere, the altitude of the station and the wavelength among others. Detailed information can be derived from [Andrews05], [Hemmati11].

2.3.1   Scintillation

Turbulence results in random fluctuations of the intensity of the optical signal known as scintillation. Scintillation is present in both uplink and downlink propagation of the signal. Atmospheric scintillation is measured in terms of scintillation index. Scintillation index (SI) is defined as the normalized variance of the received intensity [Andrews05], [Hemmati11] [Kaushal17]:

$$\sigma_I^2 = \frac{\langle I^2 \rangle}{\langle I \rangle^2} - 1 \qquad (14)$$

According to the strength of the turbulence and the scintillation variance, two categories are identified [Andrews05], [Hemmati11] [Kaushal17]:

- Weak fluctuations $\sigma_I^2 < 1$

- Strong fluctuations $\sigma_I^2 > 1$

Scintillation is more severe in lower elevation angles and for elevation angles lower than 20 degrees strong fluctuations are assumed. For modeling of scintillation index, detailed formulas which take into account the refractive index structure parameter and the propagation path among others, for uplink and downlink case, for either strong or weak fluctuations regime are reported in [Andrews05]. In this thesis we

will be focused on the weak turbulence case. The SI for weak turbulence for downlink, assuming a point receiver following the Rytov approximation [Andrews05] can be derived from the formula:

$$\sigma_{\mathrm{I}}^2 \cong \sigma_R^2 = 2.25 k^{7/6} \left(\sec(\zeta)\right)^{11/6} \int_{H_{GS}}^{H_{Turb}} C_n^2(h) \left(h - H_{GS}\right)^{5/6} dh \tag{15}$$

where σ_R^2 is the Rytov variance, ζ is the zenith angle and H_{Turb} is the maximum turbulent height (the upper bound that turbulence present), usually a value of 20km is used.

Additionally for uplink case following the Rytov approximation and assuming that there is perfect tracking of the beam (detailed information are given in [Andrews05], [Andrews06]) SI can be estimated from the next formula:

$$\sigma_{I\,tracked}^2 = 8.70 \mu_{u1} k^{7/6} \left(H_{turb} - H_{GS}\right)^{5/6} \sec^{11/6}(\zeta)$$

$$\mu_{u1} = \mathrm{Re} \int_{H_{GS}}^{H_{turb}} C_n^2(h) \left\{ \xi^{5/6} \left[\Lambda \xi + i \left(1 - \bar{\Theta}\xi\right) \right]^{5/6} - \Lambda^{5/6} \xi^{5/3} \right\} dh \tag{16}$$

$$\xi = 1 - \left(\frac{h - H_{GS}}{H_{turb} - H_{GS}} \right) \tag{17}$$

Θ and Λ parameters are computed according to [Andrews05].

For modeling of irradiance statistics assuming a turbulent medium, distributions like lognormal, Gamma-Gamma, Weibull, Rayleigh etc. depending on the strength of turbulence have been proposed [Andrews05], [Hemmati11] [Kaushal17],[Sandalidis10],[Sandalidis11]. For weak turbulence, mainly lognormal is used. The choice of distribution can vary depending on the strength of turbulence, the uplink/downlink case and the satellite (GEO/LEO).

2.3.2 Beam Wander

Beam wander is mostly caused by large scale turbulence. It is also called "hot-spot" dancing and it is the random displacement of the instantaneous maximum of the bore sight off the receiver aperture (bore sight displacement). Beam wander effects are severe in case of the uplink propagation while in case of the downlink can be omitted. This phenomenon is the main cause of degradation in the uplink and contributes to Beam Spreading among others. Several studies have been conducted for the evaluation of beam wander [Kaushal17]. It is mainly modeled as a Rayleigh distributed variable [Andrews05], [Dios04], [Reyes04a] while the variance of beam wander fluctuations can be given according to the next expression

$$\left\langle r_c{}^2 \right\rangle = 0.54 \left(H_{Turb} - H_{GS} \right)^2 \sec(\zeta)^2 \left(\frac{\lambda}{2W_0} \right)^2 \left(\frac{2W_0}{r_0} \right)^{5/3} \tag{18}$$

2.3.3   Beam Spread

As has already mentioned optical beam is spread due to refraction and diffraction. However, in presence of turbulence, the beam spread increases again, because the beam experiences random deflections. In general and as given in [Andrews05], [Andrews06] the spot size of an optical beam in turbulent atmosphere is given by:

$$W_{LT}^2 = W^2 + W_{ST}^2 + \left\langle r_c^2 \right\rangle \tag{19}$$

where W is the spot size after diffraction, W_{ST} is the spot size due to the small scale spread (also called beam breathing) and $\left\langle r_c^2 \right\rangle$ gives the beam wandering. The beam spreading can be taken into account through the Strehl ratio. Strehl ratio is a measure of quality of the signal.

2.3.4   Beam Jitter

Moreover, due to turbulence, the phenomenon of beam jitter is introduced which is defined as the move of the short term beam around its center. This effect is caused by the turbulent eddies whose size is close to the value of beam radius W_0 and less than the spatial coherence radius (r_0). Detailed information can be derived from [Andrews05].

2.3.5   Mitigation Techniques- Turbulence

2.3.5.1   Aperture Averaging

For downlink case, where turbulence is close to the receiver, mainly random fluctuations of the optical signal-scintillation effects are caused. For mitigation of downlink scintillation, aperture averaging technique is performed. Large apertures are employed to increase the average signal power collected and to reduce the signal fluctuations. To quantify the aperture averaging effect, the aperture averaging factor is defined as the ratio of the variance of received irradiance collected by a finite aperture, to the corresponding collected received irradiance of a point aperture receiver [Andrews05], [Hemmati11] [Kaushal17] [Yura83] :

$$A = \frac{\sigma_I^2(D\ )}{\sigma_I^2(0)} \tag{20}$$

where $\sigma_I^2(D)$ is the SI for an aperture with diameter equal to D and $\sigma_I^2(0)$ is the SI for a point receiver. In the literature a variety of expressions for the estimation of aperture averaging factor exist. For weak turbulence, for downlink plane wave propagation, the aperture averaging factor for finite size collecting aperture is evaluated analytically, using the following expressions [Yura83], [Andrews05], [Hemmati11] [Kaushal17] [Vetelino07]:

$$A(D) = \left[1 + 1.1 \left(\frac{D^2}{\lambda h_s \sec(\zeta)} \right)^{7/6} \right]^{-1} \tag{21}$$

$$h_s = \left[\frac{\int C_n^2(h)(h - H_{GS})^2 \, dh}{\int C_n^2(h)(h - H_{GS})^{5/6} \, dh} \right]^{6/7} \tag{22}$$

Aperture averaging technique is not applicable in uplink propagation, since the receiver is seen as a point.

2.3.5.2   Transmitter diversity

One promising technique for the mitigation of turbulence, especially for the uplink case, is the transmitter (small scale) diversity technique. In this technique multiple terminals are placed in a distance, at least higher than the coherence length of the atmosphere, so as the propagation paths are independent and they transmit the same signal. As these terminals are far enough, each beam suffers from different turbulence effects and as a result full advantage of the spatial diversity is achieved. In ARTEMIS and KODEN experimental campaigns the transmitter diversity is tested among others, with very promising results for mitigation of turbulence effects in uplink propagation [Alonso04], [Toyoshima06]. In [Comeron05], [Toyoshima07b] methodologies for the multi-beam uplink transmission, taking into account both the scintillation and the beam effects (beam wander etc.), are proposed.

2.3.5.3   Adaptive Optics

Adaptive Optics (AO) is used for the mitigation of atmospheric turbulence effects both on uplink and downlink case. AO is basically a system where a reference optical signal which comes from a star or an astronomical object or a satellite, is used to pre-correct the transmitting wave so as the turbulence distortions are cancelled. An AO system basically consists of a wave front sensor, a wave front processor and conjugation elements (deformable/tip-tilt mirrors) [Tyson96]. The first two elements using the reference signal, estimate the conjugation phase which is needed to be applied in the transmitting signal so as the

turbulence distortions are cancelled, while the phase conjugation operation is executed using deformable mirrors [Tyson96].

However, for the uplink OA systems appear some restrictions [Tyson96]. The prominent one is that for the correction of turbulence distortions, both the reference signal and the transmitting wave should propagate through the same path. Therefore, point-ahead-angle (PAA) shall be smaller than the isoplanatic angle (IPA) [Fried82], [Tyson96].
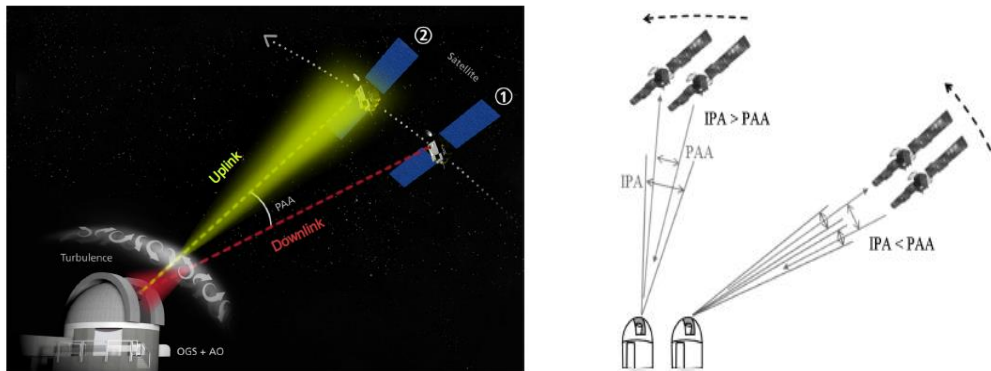
Fig. 6: Point ahead angle and isoplanatic angle configuration (source: [Leonard16] and [Dimitrov15].

For the incorporation of AO systems compensation in channel modeling, Zernike polynomial terms are used. In [Tyson96], a methodology for the computation of scintillation index, log amplitude variance and other important metrics for an AO system is exhibited.

3   ILWC SPACE-TIME SYNTHESIZER

As described in Introduction ILWC annual statistics can be described by lognormal distribution [ITU840], [Jeannin08]. For synthesis of ILWC (L) time series for a specific location the statistical parameters of $ln(L)$ i.e. the mean value (m), the standard deviation (σ) and the probability of cloud coverage (P_{clw}) for each place of interest are required. Additionally, in [ITU1853-1] a methodology for the synthesis of point values of ILWC correlated only on temporal domain and no on spatial is proposed. However, to take into account the effect of clouds along the whole slant path a single point is not sufficient. Additionally, as discussed in Introduction for mitigation of cloud coverage site diversity (OGS diversity) technique is employed. Therefore the spatial correlation of clouds is needed.

In this Chapter methodologies for the generation of 2 and 3 dimensions ILWC time series, correlated both on temporal and on spatial domains are exhibited. More specifically, in Section 3.1 a stochastic dynamic model for the generation of 2 Dimensions ILWC fields is proposed. The model is based on the stochastic differential equations (SDEs) and incorporates the spatial and temporal behaviour of ILWC.

In Section 3.2 a 3D ILWC space time synthesizer is proposed. Using the 2-D ILWC time series presented in Section 3.1 and incorporating the vertical extent of clouds 3-D ILWC time series are generated. In order that the vertical extent of clouds can be obtained the well-defined expression reported in Section 2.2.2.2 which relates the LWC with height is employed.

Finally, in Section 3.3 the capability of the space-time synthesizer of ILWC to reproduce the exceedance probability of theoretical curves from ITU-R databases (ECMWF ERA-40) for several locations is examined.

3.1   ILWC 2D Synthesizer

In this Section a methodology for the generation of 2 Dimensions ILWC time series correlated both on temporal and on spatial domains for each place of interest (Ground Station-GS) is exhibited. For the generation of spatially correlated time series of ILWC, multi-dimensional stochastic differential equations are employed. The main idea is the synthesis of ILWC maps for each OGS. Each map consists of several ILWC grids with spatial resolution of 1 km x 1 km, correlated on temporal and on spatial domain. The ILWC map for each GS can be exhibited as $L_{map,GS} = \left[L_1, L_2, \ldots, L_n \right]$, where L_i are the ILWC grids along the slant path and n is the number of grids needed so as the whole slant path is taken into account. In Fig. 7 the configuration of the ILWC 2D map is reported:
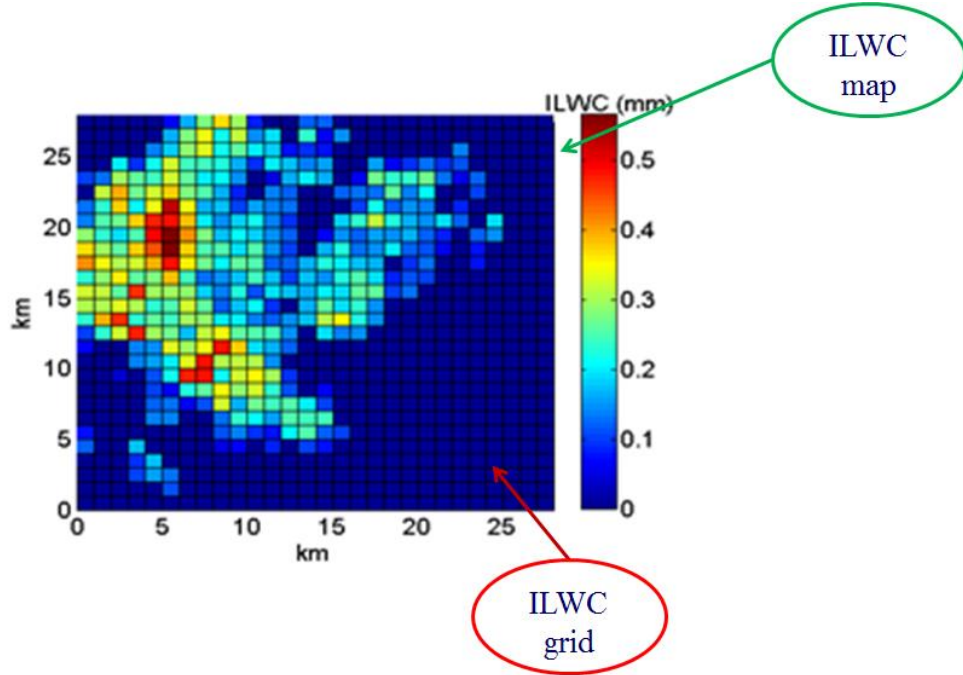
Fig. 7: ILWC map configuration

For more than one places of interest (GSs), an $L_{map,OGS}$ is generated for each GS. Again these maps are correlated both in temporal and spatial domain one to each other i.e. the ILWC grids of GS #3 are not only temporally and spatially correlated one to each other but also they are temporally and spatially correlated with the ILWC grids of GS #1, GS #2, etc. Thus, the ILWC field for N stations can be identified as $L_{total\_field} = \begin{bmatrix} L_{map,GS^1} & L_{map,GS^2} & \dots & L_{map,GS^N} \end{bmatrix}$. Now L_i time series are computed according to the next expression as described in Section 2.2.2.2:

$$L_i(t) = \begin{cases} \exp\left[Q^{-1}\left(\frac{1}{P_{CLW}} Q\big(G_i(t)\big) \right) \times \sigma + m \right] & G_i(t) \geq \alpha_{th} \\ 0 & G_i(t) \leq \alpha_{th} \end{cases} \tag{23}$$

where m, σ, P_{clw} are the statistical parameters of $ln(L)$ for each place of interest and can be derived from data bases like ERA-Interim, ITU-R P.840-6 [ITU840-6] etc. The statistical parameters can be considered constant along the slant path. $Q(\ )$ is the well-known Gaussian Q-function and α_{th} is computed according to the next expression:

$$\alpha_{th} = Q^{-1}\left(P_{CLW} \right) \tag{24}$$

64

$G_i(t)$ is the underlying Gaussian process for the generation of each grid (e.g. with index i). $G_i(t)$ can be defined as the superposition of two Gaussian processes $X_i = [X_i^1, X_i^2]$ where $1 \leq i \leq n*N$ (n is the number of grids for each OGS and N is the number of OGSs)[ITU1853-1]:

$$G_i(t) = \gamma_1 \cdot X_i^1(t) + \gamma_2 \cdot X_i^2(t), \ \ (i = 1,....,n*N) \tag{25}$$

where γ_1, γ_2 can be derived from meteorological data, or the values proposed in [ITU1853-1] can be used. The temporal correlation of the underlying Gaussian processes X_i^k ($k=1, 2$, $i=1:n*N$) is considered exponentially decaying as a function of time [ITU1853-1]. The $n*N$ different ILWC stochastic processes are assumed as an $n*N$-dimensional continuous Markov process. Due to the spatial correlation of clouds, time series of each X_i^k can be generated through the solution of the following $n*N$-dimensional Stochastic Differential Equation [Karagiannis12]:

$$d\mathbf{X}_t^k = \mathbf{B}^k \cdot \mathbf{X}_t^k dt + \mathbf{S}^k \cdot d\mathbf{W_t} \ , \ (k=1, 2) \tag{26}$$

with strong solution [Karatzas91], [Karlin75]:

$$\mathbf{X}_{i,t}^k = e^{t \cdot \mathbf{B}^k} \cdot \mathbf{X}_0^k + e^{t \cdot \mathbf{B}^k} \cdot \int_0^t e^{-s \cdot \mathbf{B}^k} \cdot \mathbf{S}^k \cdot d\mathbf{W}_s, \ (k=1, 2) \tag{27}$$

where where $\mathbf{B}^k$ is the diagonal matrix $\mathbf{B}^k = [b_{ij}^k]_{1 \leq i, j \leq n}$ with elements

$$b_{ij}^k = - \beta^k \cdot \delta_{ij} \tag{28}$$

where δ_{ij} is the Kronecker delta function and β^k are the dynamic parameters of the Gaussian processes of ILWC. β^k can be derived either from ILWC data or from [ITU1853-1]. Moreover,

$$e^{t\mathbf{B}} = \sum_{n=0}^{\infty} \frac{t^n}{n!} \mathbf{B}^n \tag{29}$$

Since matrix $\mathbf{B}$ is a diagonal one we have:

$$[e^{t\mathbf{B}}]_{ij} = e^{-\beta_i t} \delta_{ij} \tag{30}$$

$\mathbf{W}(t)$ is the $n*N$-dimensional Wiener process i.e. $\mathbf{W}_i(t) \ 1 \leq i \leq n*N$ are independent Wiener processes known as Brownian motions [Karatzas91]:

$$\mathbf{W}(t) = [W_1(t),...,W_{n*N}(t)]^T \tag{31}$$

The same Wiener process is inserted both in $X_{i,t}^1$ and $X_{i,t}^2$. As far as the computation of $\mathbf{S}^k$ is

concerned [Karagiannis12], the correlation matrix $\mathbf{C}$ will be firstly estimated. This matrix contains the information about the spatial correlation of ILWC. Since the size of every grid is 1km x 1km, a single link slant path may be affected by more than one grid and therefore the spatial correlation must be incorporated into the model even for the calculation of cloud attenuation on a single link. The correlation $\rho_{i,j}$ between X_i^k and X_j^k, depends on the distance between i and j grid points and for this we use the expression proposed in [Luini14] derived from MODIS database (proposed for distances less than 250km):

$$\rho_{i,j}(d) = 0.35 e^{-\frac{d}{7.8}} + 0.65 e^{-\frac{d}{225.3}}, \; d(km) \tag{32}$$

Therefore, the correlation matrix $\mathbf{C}$ of the n-points of ILWC is given:

$$\mathbf{C} = \begin{bmatrix} 1 & . & . & . & \rho_{1,n*s} \\ . & 1 & & & . \\ . & & 1 & & . \\ . & & & 1 & . \\ \rho_{n*s,1} & . & . & . & 1 \end{bmatrix} \tag{33}$$

If we denote $\mathbf{\Lambda}^k$ as

$$\mathbf{\Lambda}^k = 2 \cdot \beta^k \cdot \mathbf{C} \tag{34}$$

and $\mathbf{\Lambda}^k = \mathbf{S}^k \cdot (\mathbf{S}^k)^{\mathbf{T}}$, $\mathbf{S}^k$ matrix is obtained from Cholesky decomposition of $\mathbf{\Lambda}^k$ [Karagiannis12]. Finally, the initial values of the Gaussian processes are given through the following vector:

$$\mathbf{X}_0^k = [x_{01}^k, x_{02}^k, ..., x_{0n*N}^k] \tag{35}$$

In b)

Fig. 8a and b, snapshots of ILWC maps 50x50km correlated on spatial and temporal domain for a hypothetical GS in Paphos, Cyprus, employing the proposed methodology are presented. The first one is at time $t=t_0$ while the second one is 60 min later.

a)

b)
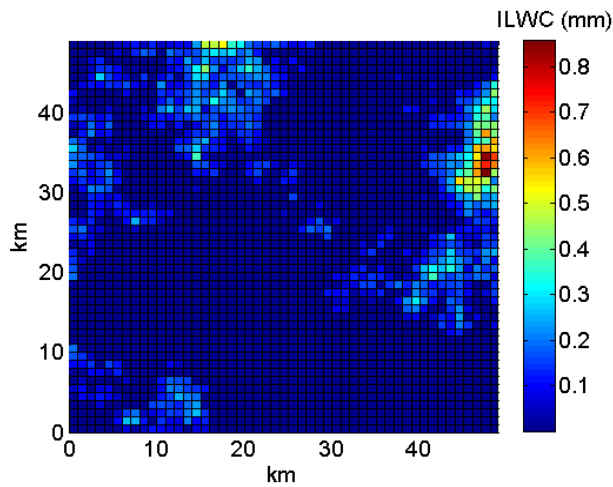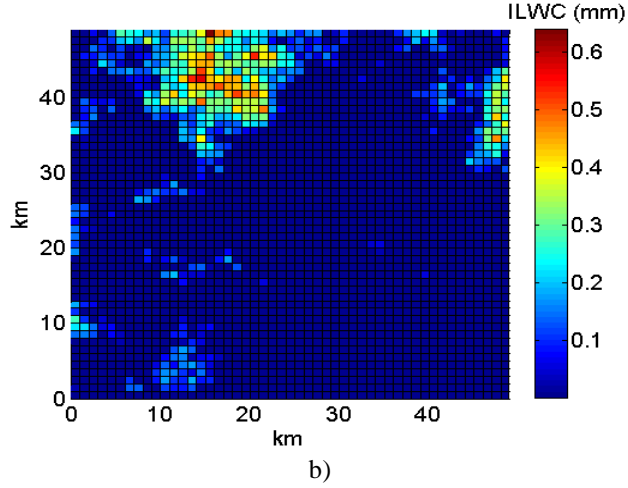
Fig. 8: Snapshots of ILWC maps correlated on spatial and temporal domain, a) $t=t_0$**, b)** $t=t_0+60min$

3.2   ILWC 3D Synthesizer

In the previous subsection the 2D ILWC synthesizer is reported. However in order to accurately take into account the effect of clouds along the propagation path the vertical extent of clouds is needed. Therefore the 2-D maps are converted to 3-D incorporating the vertical extent of clouds. In order to obtain the vertical extent of clouds, LWC (*w*) at a given time instance and at a given grid point on the horizontal plain may be calculated using the LWC model proposed in SMOC [Luini14]. Taking as input the ILWC time series generated in the previous section, the LWC time series for a height *h* above mean sea level, for a grid *i* can be calculated through [Luini14]:

$$\tilde{w}_i\left(h,t\right)=\begin{cases}\dfrac{L_i(t)}{c_i^{\,2}(t)^{c_i^{\,1}(t)}\,\Gamma(c_i^{\,1}(t))}\left(h-h_0\right)^{c_i^{\,1}(t)-1}\,e^{-(h-h_0)/c_i^{\,2}(t)} & \text{for } h\geq h_0 \\[2mm] 0 & \text{for } h<h_0 \end{cases} \tag{36}$$

$$c_i^{\,1}(t)=4.27\ e^{-4.93(L_i(t)+0.06)}+54.12\ e^{-61.25\ (L_i(t)+0.06)}+1.71 \tag{37}$$

$$c_i^{\,2}(t)=3.17\ c_i^{\,1}(t)^{-3.04}+0.074$$

In the above equations $\tilde{w}_i(h,t)$ in g/m^3 is the Liquid Water Content depending on the vertical height, *h* in km is the vertical height of the cloud, h_0 in km is the cloud base height, *L* in mm is the ILWC, $\Gamma()$ is the Gamma function and $c_i^{\,1}(t)$, $c_i^{\,2}(t)$ are the parameters regulating the shape of $\tilde{w}_i(h,t)$. With this methodology we may acquire, from ILWC *L* fields, time series of $\tilde{w}_i(h,t)$, not only on different grids but also on different time instances and height. Moreover, for the calculation of the vertical extent (*dh*), the base cloud height (h_0) and the top cloud height (h_{th}) are needed. The max height (h_{th}) is calculated from (36) considering the remark from [Luini14] that $\tilde{w}(h,t)\to 0$ for $\tilde{w}_i(h,t)\leq 0.06\cdot L_i(t)$ and furthermore h_0 is taken from the generalized extreme value PDF [Luini14] that has been derived from the CloudSat data:

$$p(h_0)=\frac{1}{\sigma}t\left(h_0\right)^{\xi+1}e^{-t(h_0)}\quad t(x)=\begin{cases}\left[1+\left(\dfrac{x-\mu}{s}\right)\xi\right]^{-\frac{1}{\xi}} & \xi\neq 0 \\[3mm] e^{-(x-\mu)/s} & \xi=0 \end{cases} \tag{38}$$

67

where ξ=0.484, s=0.582, μ=0.987. Therefore, the vertical extent $dh=h_{th}- h_0$ may be calculated. Cloud base is considered constant along the slant path. The vertical extent is assumed constant within the grid.

In Fig. 9 we present a snapshot of time series for LWC showing its vertical extent dependence as computed using the above methodology is presented.
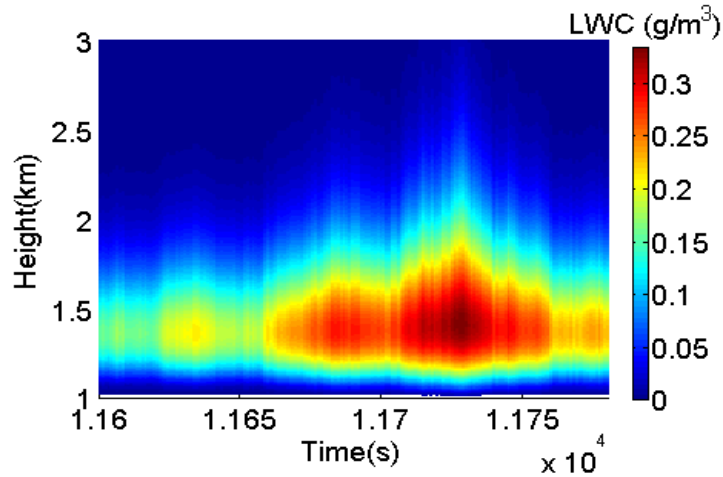
Fig. 9: LWC vertical extent time series

In Fig. 10 snapshots of 2-D ILWC maps correlated on spatial and temporal domain for a hypothetical OGS in Chania, Crete are presented. The first one is at time $t=t_0$, while the second is 60 min later and in Fig. 11 2D cloud maps are transformed in 3D, with the proposed methodology.
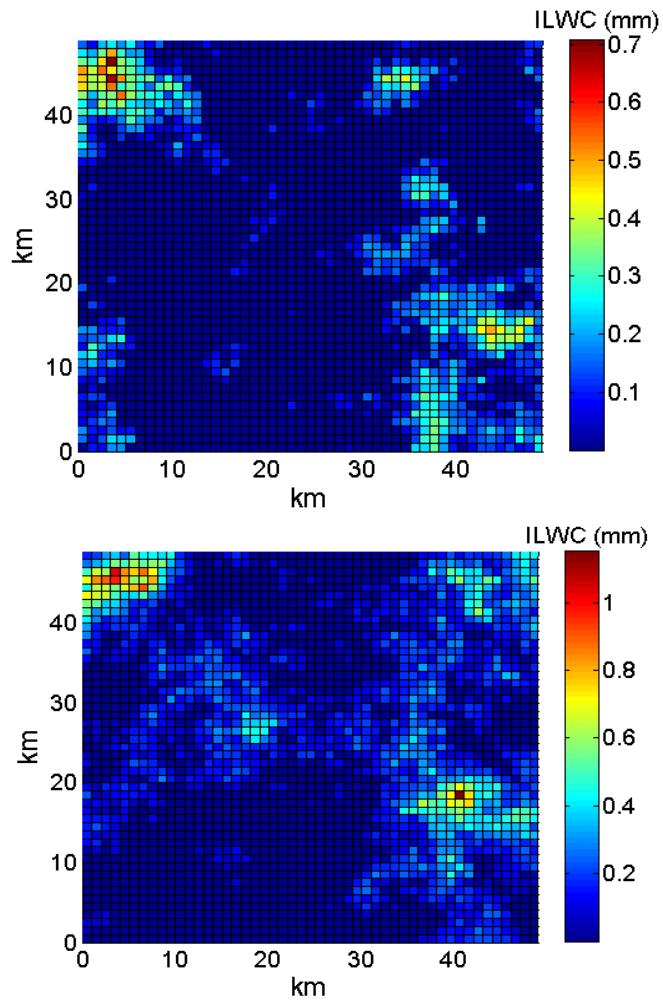
Fig. 10: Snapshots of ILWC 2-D maps correlated on spatial and temporal domain up: *t=t₀*, **down** *t=t₀+60*min
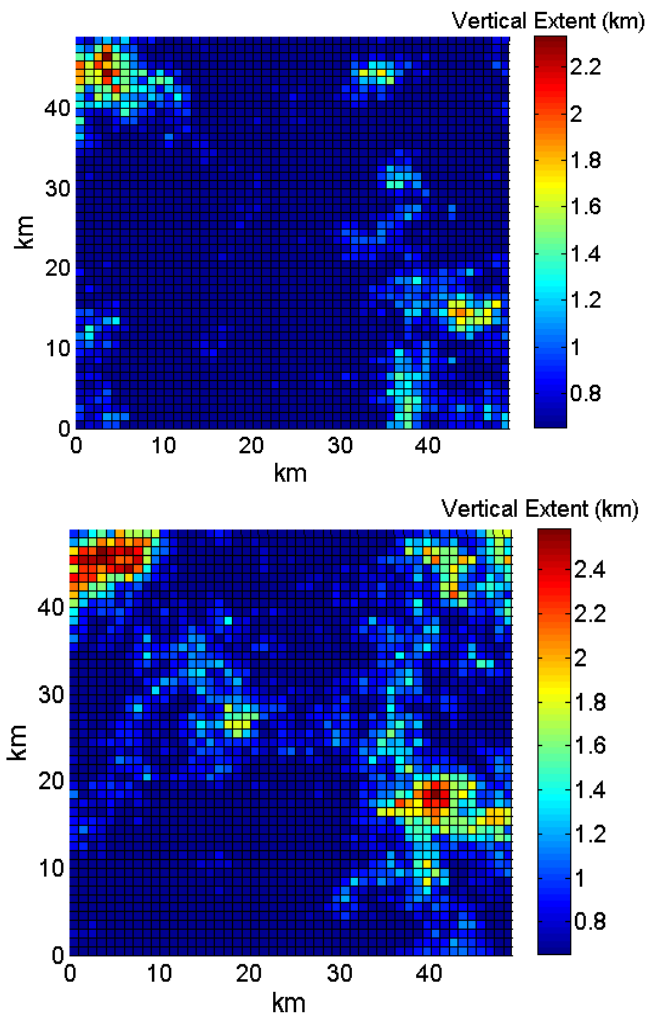
Fig. 11: Snapshots of 3D maps correlated on spatial and temporal domain-Vertical Extent up:*t=t₀*, down: *t=t₀+60*min

3.3   LIWC time series synthesizer validation

In this section, the capability of the ILWC space-time synthesizer to reproduce the first-order (exceedance probability) statistics of the theoretical curves from ITU-R databases (ECMWF ERA-40) [ITU840] for some locations is confirmed. It can be observed that the Complementary Cumulative Distribution Functions (CCDFs) derived from the synthesized data and the ones from databases coincide (Fig.12, Fig.13). That's a proof that the ILWC space time synthesizer reproduces the first order statistics of ILWC.
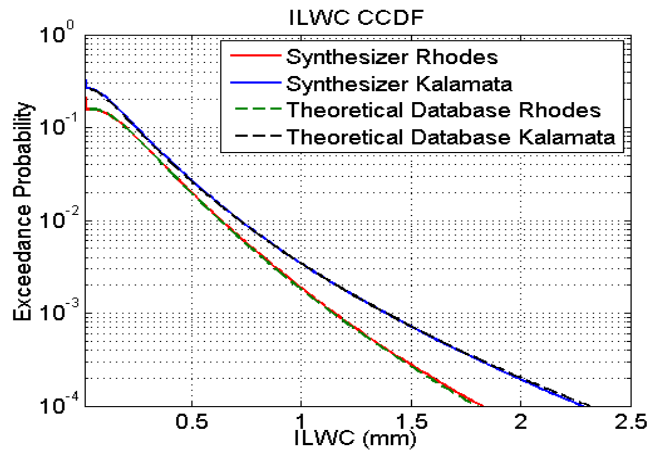
Fig. 12: First order statistics validation of the ILWC synthesizer, Rhodes, Kalamata Greece.
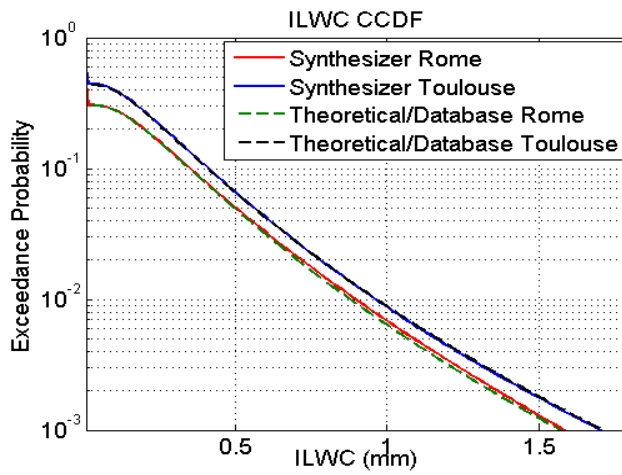
Fig. 13: First order statistics validation of the ILWC synthesizer, Rome, Italy, Toulouse, France.

4   CLOUD ATTENUATION-CLOUD FREE LINE OF SIGHT TIME SERIES GENERATORS

In this Chapter the 2D and 3D synthesizers proposed in Section 3 are employed for the generation of cloud attenuation and cloud free line of sight time series for both single and joint slant paths. Single and joint CFLOS and cloud attenuation statistics are reported.

Firstly, in Section 4.1 employing the 2D and 3D synthesizers proposed in Section 3 clouds are classified based on the cloud vertical extent and using the microphysical properties of them and the well-known Mie scattering theory, a unified space-time model for the prediction of induced attenuation due to clouds for frequencies above Ka band [26.5-40 GHz] and up to optical range are presented. The proposed methodology is tested with data obtained from literature, showing encouraging results. Finally, single and joint cloud attenuation statistics from Ka to optical band are reported.

To continue, in Section 4.2 assuming an on/off channel with cloud occurrence a methodology for the generation of Cloud Free Line of Sight (CFLOS) time series correlated on temporal and spatial domain is presented. The proposed methodology takes advantage of the use of the ILWC synthesizers exhibited in Section 3.

In Section 4.3 some information about the use of the synthesizers proposed so far in this Chapter assuming non-GEO satellites, i.e. with time dependent elevation angles as space segment, are exhibited. In Section 4.4 single and joint CFLOS statistics assuming as space segment either GEO or LEO or MEO satellites using the synthesizer proposed in Section 4.2, are exhibited.

Finally, in Section 4.5 the space time CFLOS synthesizer (Section 4.2) is employed in order that the average number of OGS switches for an OGSN and the percentage of time each OGS is selected to transmit data, are estimated. Therefore, the capability of space time synthesizers in order that valuable statistics from the system point of view can be derived, is highlighted.

4.1   Cloud Attenuation from Ka to Optical Band

In this Section a methodology for the calculation of cloud attenuation time series using as input the time series of ILWC synthesizer presented in Section 3 is proposed. This model appears to be unified and can be employed in both RF bands and optical range.

To begin with as described in Section 2.2 (expression (1)) the attenuation for a specific wavelength (λ) induced from liquid water particles of clouds, is calculated as:

$$A(\lambda) = \int_{l_0}^{l_{max}} \beta_{ext}(\lambda) d\ell \quad \text{(dB)} \tag{39}$$

where $\beta_{ext}(\lambda)$ is the volume extinction coefficient and depends on the wavelength λ. $A(\lambda)$ is the induced attenuation on the slant path through the cloud medium and l_{max}, l_0 are the upper and lower limits of

the slant path in (km) through the cloud formation, respectively. The volume extinction coefficient, called also specific attenuation, is given as:

$$\beta_{ext}(\lambda) = 4.343 \times 10^3 \int_0^\infty \sigma_{ext}(r,\lambda) n(r) dr \quad \text{(dB/km)} \tag{40}$$

where $\sigma_{ext}(r,\lambda)$ in μm^2 is the extinction cross coefficient, $n(r)$ in $\mu m^{-1}/cm^3$ is the particle size distribution of cloud droplets, r in μm is the clouds droplet radius. Since the $\sigma_{ext}(r,\lambda)$ can be estimated for the whole range of wavelengths, appears to have a unified use for the prediction of attenuation due to clouds. $\sigma_{ext}(r,\lambda)$ can easily be calculated by the employment of the classical scattering Mie Theory [Bohren83], [Ishimarou78]. There are also available free software tools for these calculations [scattport].

The particle size distribution of cloud droplets depends on the cloud type. Water clouds can be classified into four main different types, taking into account their vertical extent and are presented in Table 2 [Luini16]:

Table 2: Vertical extent of the four cloud types employed in the methodology

Cloud Type	Average Vertical Extent (km)
Cumulonimbus	>2.5
Cumulus	2.5
Nimbostratus	1.4
Stratus	0.7

For the calculation of the attenuation due to clouds the vertical extent of clouds is needed. Therefore the ILWC synthesizer presented in Section 3 is employed. Employing the 2 D and 3 D synthesizer the vertical extent of clouds along the propagation path, depending on the ILWC statistics for each place of interest, is estimated.

In addition, a model for the particle size distribution $n(r)$ must be adopted. Therefore, we employ the four-parameter modified gamma function [Luini16], which is a flexible and widely used representation of water clouds particle size distribution:

$$n(r) = g \cdot r^\alpha \cdot \exp\left(-b \cdot r^\gamma\right) \tag{41}$$

Since the vertical extent of the cloud is estimated from the 3D ILWC synthesizer, the cloud type is defined according to Table 2 and the parameters a, b, γ can be determined according to Table 3.

Table 3: a, b, γ parameters for the particle size distribution of cloud droplets

Cloud Type	a	b	γ
Cumulonimbus	3	0.5	1
Cumulus	3	0.5	1
Nimbostratus	2	0.425	1
Stratus	2	0.6	1

Now in [Luini16] an expression which relates the Liquid Water Content w with particle size distribution of cloud droplets $n(r)$ is introduced:

$$w = \frac{4}{3}\pi\rho_w \int_{r_1}^{r_2} r^3 n(r)\,dr = \frac{4}{3}\pi\rho_w \frac{g}{\gamma}\frac{\Gamma\big((\alpha+4)/\gamma\big)}{b^{(\alpha+4)/\gamma}} \tag{42}$$

where ρ_w in g/cm^3 is the water density and g, a, b, γ are the particle size distribution of cloud droplets parameters. Employing the equation (36) from the previous Section, where LWC is computed for every grid point i depending on the height, the time and the ILWC 2D synthesizer, we can calculate easily the parameter g of the particle size distribution of cloud droplets as a function of the height and time for every point i:

$$g_i(h,t) = \frac{3\cdot\gamma\cdot b^{\alpha+4/\gamma}\cdot \tilde{w}_i(h,t)}{4\cdot\pi\cdot\rho_w\cdot\Gamma\big((\alpha+4)/\gamma\big)} \tag{43}$$

Therefore, the particle size distribution of cloud droplets is calculated in terms of cloud height, i.e. $n(r,h)$ and consequently the volume extinction coefficient is also calculated in accordance to height. Finally, employing the expressions (39) and (40) and the rest calculated parameters, time series of attenuation due to clouds is computed for the specific slant path and the cloud height:

$$A(t,\lambda) = \int_{l_0}^{l_{max}} 4.343\times10^3 \int_0^{\infty} \sigma_{ext}(r,\lambda)n(r,h)\,dr\ d\ell \quad \text{(dB)} \tag{44}$$

Here it must be noted that knowing the 3D profile of all the cloud grids along the slant path, i.e. the vertical extent of each ILWC grid and assuming that each ILWC grid has dimensions of 1km^2, cloud attenuation statistics can be computed depending on the propagation path i.e. the elevation angle and the altitude of the station.

In Fig. 14 and Fig. 15 two examples (snapshots) of the proposed cloud attenuation time series methodology are presented. The ground terminal is located in Milan, Italy and the considered elevation angle is 40deg. In Fig. 14 the operating frequency is set equal to 40 GHz, while in Fig. 15 a wavelength in optical range equal to 1550nm is considered.

75
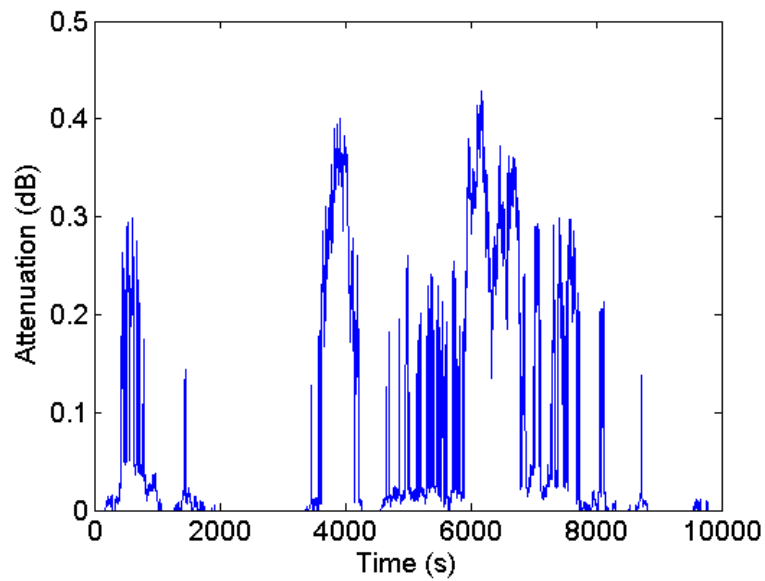
Fig. 14: Cloud attenuation time series at 40GHz, 40deg, Milan, Italy
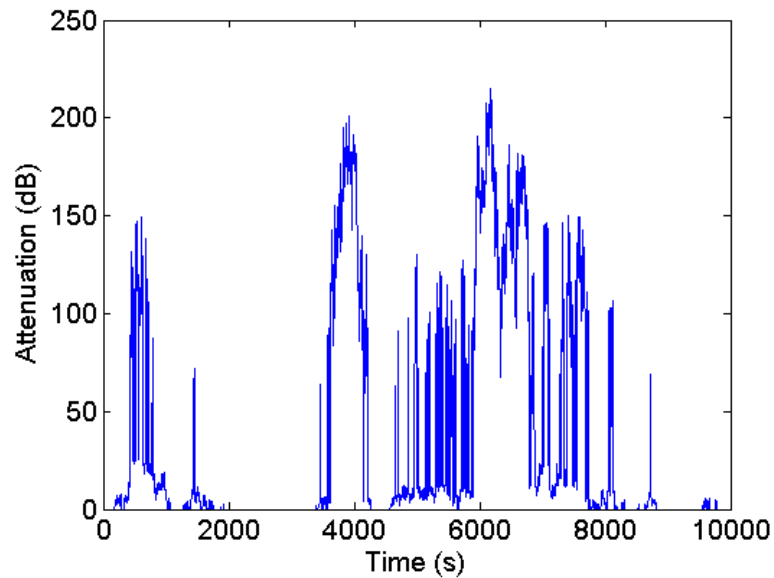
Fig. 15: Cloud attenuation time series at 1550nm, 40deg, Milan, Italy

4.1.1   Validation of Cloud Attenuation time series synthesizer

The proposed cloud attenuation time series synthesizer is validated in terms of attenuation first order statistics CCDF with experimental data. Since the synthesizer is unified it will be compared with data both in RF and optical frequencies.

Firstly, in Fig. 16 the proposed space time cloud attenuation synthesizer is compared with experimental data at 30 GHz, from FERAS station [Report1]. The attenuation data used for this comparison

have been obtained from local radio soundings at FERAS station in Milan/Linate, in accordance with the use of Salonen's model and the Rayleigh model at 30GHz [Report1]; a vertical link is considered. For this case the long term statistical parameters m, σ, and P_{CLW} of the ILWC that are required for the attenuation prediction, have been computed from the specific data [Report1], in order to have a fair comparison with the same inputs.
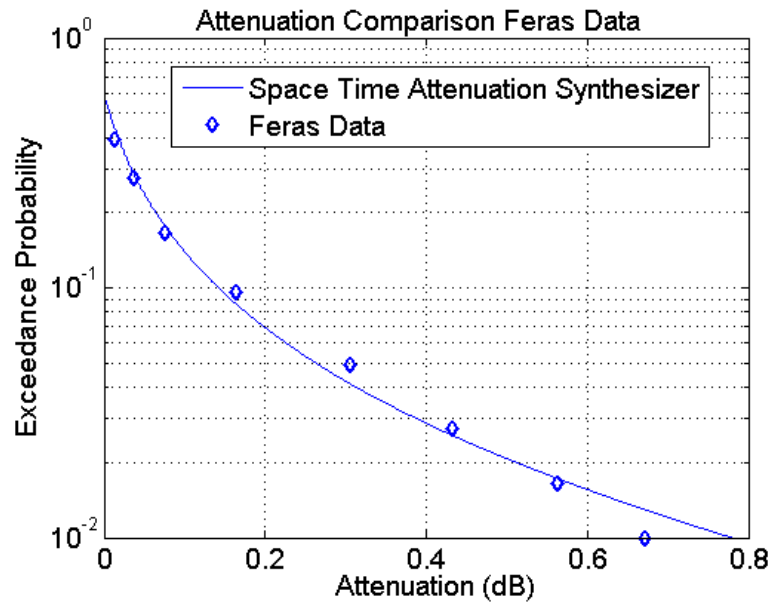
Fig. 16: RF validation of Cloud Attenuation Space Time Synthesizer with data at 30 GHz

In Fig. 17 the validation of the proposed model with attenuation data at 10.6μm is exhibited. The data were exported from [Report1] following the same procedure as before. The link is vertical and it is located in Milan/Linate.
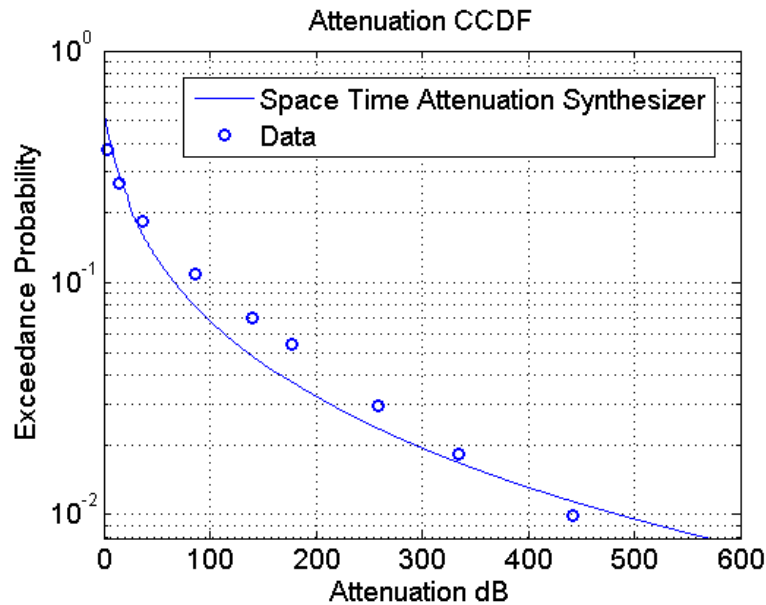
Fig. 17: Validation of Cloud Attenuation Space Time Synthesizer with data at 10.6μm wavelength

The exceedance probability calculated from the proposed model appears to be in a very good agreement with experimental attenuation data at both configurations, using 30GHz operating frequency and 10.6μm wavelength.

4.1.2   Cloud Attenuation Numerical Results

In this section the proposed methodology is employed for the generation of cloud attenuation statistics for a ground to GEO satellite link, for both RF and optical frequencies.

To begin with, the predicted single link cloud attenuation statistics in terms of complementary cumulative distribution function (CCDF) for two hypothetical links, one located in Athens, GR (37.98°N, 23.79E) and the other in Paris, FR (48.86°N, 2.36 °E), for two operating frequencies (40 GHz and 90GHz) and also two elevation angles (20deg and 40deg), are reported in Fig.18 and Fig.19. The statistical parameters of ILWC needed for the ILWC synthesizer are derived from ERA 40 [ITU840] for each place. For both stations the altitude is assumed close to 200m. Along with the CCDFs derived from the proposed methodology, we present the CCDFs predicted employing the ITU-R P.840-6 [ITU840].
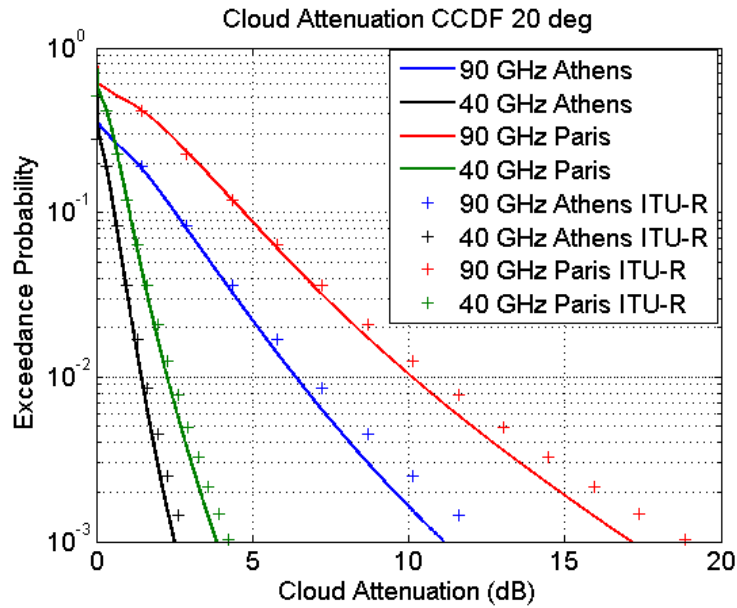
Fig. 18: Cloud Attenuation CCDFs with elevation angles 20deg, 40GHz, 90GHz
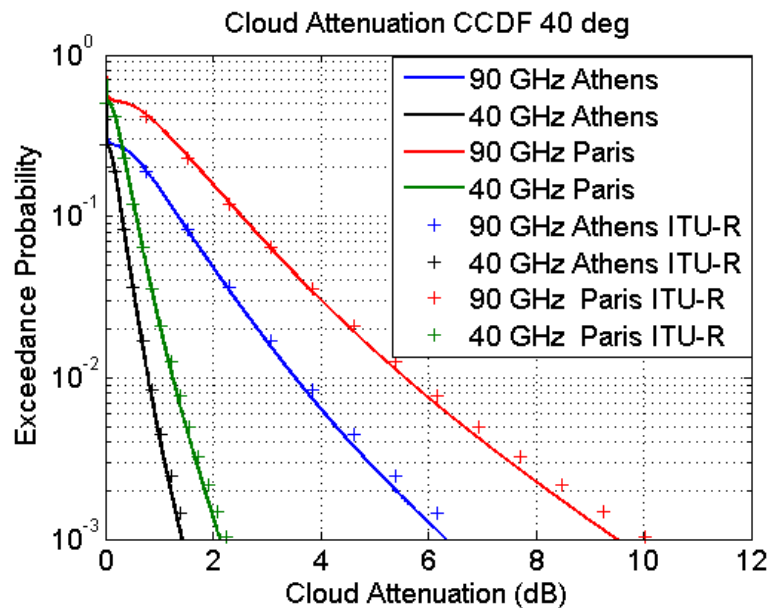
Fig. 19: Cloud Attenuation CCDFs with elevation angles 40deg, 40GHz, 90GHz

It can be easily observed that as the frequency of operation increases the impact of cloud attenuation is greater and therefore it cannot be omitted in the performance analysis of the satellite links and especially in W band (90 GHz).

Moving on to optical frequencies, the CCDF of cloud attenuation for 3 locations, assuming as space segment the ASTRA satellite at 19.2 ºE and the wavelength of operation at 1550nm, are presented in Fig. 20. In Table 4 the characteristics of the three links are reported.

Table 4: Link Characteristics, Cloud Attenuation-Optical Frequencies

Location	Latitude	Longitude	Altitude (m)	Elevation Angle (deg)
Tenerife, SP	28.27°N	17.89 °W	2400	37.46 deg
Hymettus Athens, GR	37.96°N	23.82 °E	1000	45.73 deg
Milan, IT	45.47°N	9.19 °E	300	36.71 deg
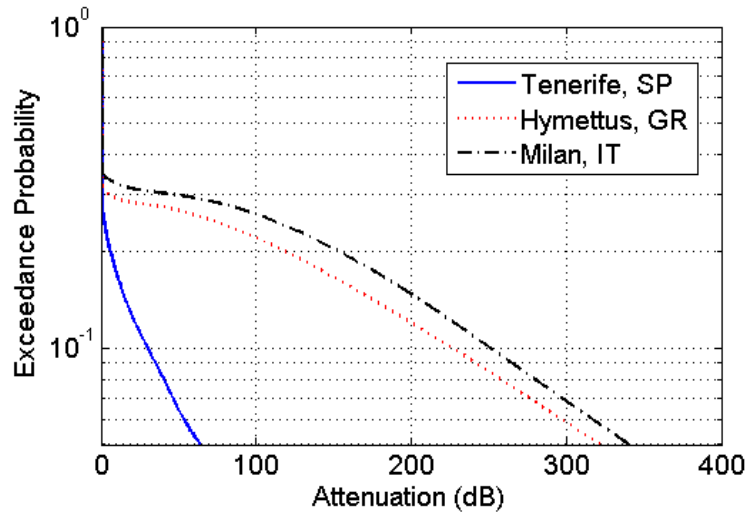
Fig. 20: Cloud Attenuation CCDF, wavelength: 1550nm

4.2 Cloud Free Line of Sight Time Series Generator

It can be easily observed from Fig. 13 that the attenuation induced by clouds is very high even with the presence of clouds. Therefore, the blockage of the link and an on/off channel is assumed with the presence of clouds.

Cloud Free Line of Sight (CFLOS) probability is the probability of the optical link not blocked by clouds and it is defined as the complementary probability of cloud occurrence (P_{clw}), which is, 1 minus P_{clw}. For vertical links P_{clw} can be derived from data sets like ERA Interim, ERA 40 [ITU840] etc. In the proposed approach, CFLOS time series are computed taking into account the propagation path (altitude of the station, elevation angle) the vertical extent of clouds and the temporal and spatial correlation of clouds.

To begin with the ILWC synthesizer presented in Section 3 is employed. The main steps of the methodology will be presented below:

- 2D ILWC maps (time series) correlated both on temporal and on spatial domain employing the proposed synthesizer are produced for each place of interest (Section 3.1).

- The vertical extent of each ILWC grid is computed and the 2D ILWC maps are converted into 3D maps. The vertical extent is considered constant within the grid.

- Cloud mask (Cloud blockage) time series are computed: it is assumed that if there is at least one cloud grid (grid with ILWC>0) with vertical extent that impairs the link along the slant path then the whole optical slant path, is considered blocked. It is considered that a cloud grid impairs the link if the lowest point of slant path crossing that grid is lower than the top height of the grid. Therefore since the 3D configuration of the clouds along the slant path is defined, the cloud mask time series are computed taking into account the propagation path (elevation angle and altitude of the station (for high altitude stations)). The whole slant path will be either blocked or free of clouds.

- CFLOS time series are computed as 1 minus the cloud mask time series.

- Finally CFLOS probability is the average of CFLOS time series.

In Fig. 21 the need of incorporating the elevation angle and the altitude of the station (for high altitude stations) for the estimation of CFLOS, for optical satellite links, is identified.
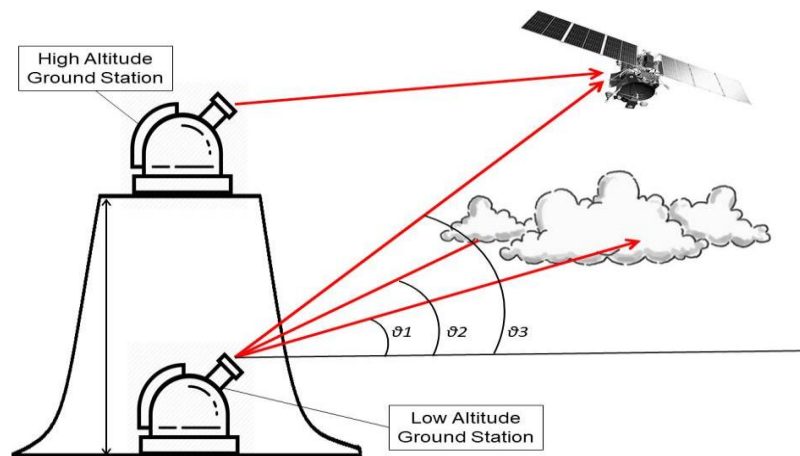
Fig. 21: Optical Satellite Link -CFLOS calculation (elevation angle, high altitude).

In Fig. 22 a snapshot of cloud mask time series is presented for an optical satellite link in Nemea, GR, with elevation angle 46deg.
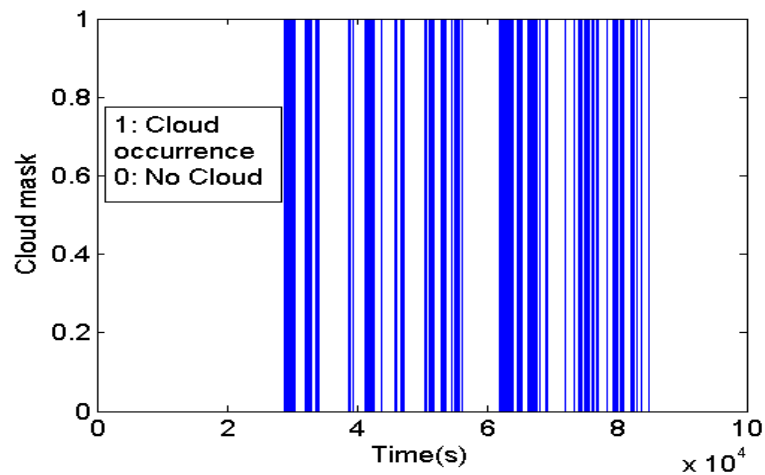
Fig. 22: Cloud Mask Time series

In Fig. 23 CFLOS probability is computed using the reported synthesizer for different elevation angles. A hypothetical link in Naxos is assumed while CFLOS is estimated for elevation angles from 20 to 90deg. Statistical parameters of ILWC are derived from ITU-R databases (ECMWF ERA-40) [ITU840]. It can be easily pinpointed that for low elevation angles, CFLOS is lower while for elevation angles are more than 50 deg the CFLOS remains nearly constant. It comes from the fact that for low elevation angles the propagation path in the atmosphere increases and as a result the probability of a cloud present in the slant path increases.
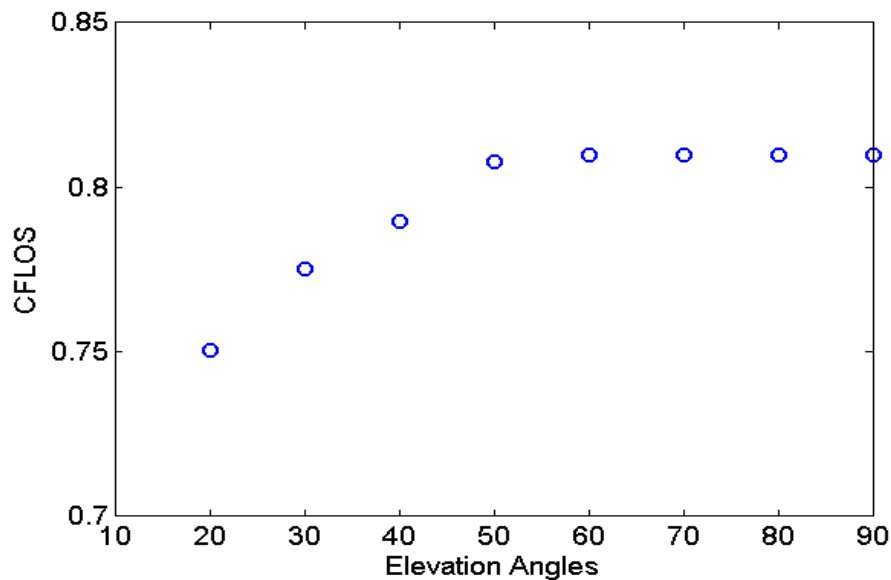
Fig. 23: CFLOS vs Elevation Angle – Hypothetical OGS in Naxos

4.3   Employment of space time synthesizers on NGSO systems

In this section some information about the employment of the synthesizers presented in the previous sections in case of assuming a Non GEO satellite as space segment, i.e. a LEO satellite or a MEO satellite or

a MEO constellation is presented. The main assumptions are the same either cloud attenuation or CFLOS time series are produced.

To begin with, regarding the cloud attenuation and CFLOS probability the main difference between a Ground Station-GEO and a Ground Station-Non GEO satellite communication system is that for the Ground Station-Non GEO satellite communication system the elevation angle of the link changes with time. Therefore, the developed methodologies must be able to capture the elevation angle time dependence. The methodology followed is based on the synthesizers proposed in previous sections. The main steps and assumptions of the methodology used are reported:

- 2D ILWC maps (time series) with a specific time resolution correlated both on temporal and on spatial domain are produced for each place of interest, employing the proposed synthesizer (Section 3.1).

- The vertical extent of each ILWC grid is computed and the 2D ILWC maps are converted into 3D maps. The vertical extent is considered constant within the grid.

- The sub satellite points of the non GEO satellite or the non GEO satellite constellation are generated using a specific time resolution and or an orbital period. For this step the AGI/STK tool kit [AGI] may be used for the computation of the sub satellite points. The time resolution of the sub-satellite points is selected to be the same with the time resolution of ILWC time series. For MEO case, sub satellite points for 1 orbital period are enough; however for LEO satellites more than 1 orbital period is needed.

- For each station, using the sub satellite points, the elevation angles with each satellite are calculated with the same time resolution. When a satellite is not in the visibility area of the station the elevation angle is considered zero for the calculations. If a non GEO constellation (e.g. MEO constellation) is assumed and if in the visibility area of the station there are more than one satellites then it can be assumed that the ground station communicates with the satellite with the highest elevation angle, in the visibility area for this time instant.

- Since the 3D profile of clouds along the slant path is known for every time instant and the elevation angles are known, with the same time resolution, cloud attenuation and CFLOS time series are computed, employing the methodologies proposed in Section 4.1 and Section 4.2.

It must be noted that the 2D and 3D ILWC synthesizers are independent of the elevation angle.

4.4   Single and Joint CFLOS numerical results

In this section the methodologies proposed so far for the generation of CFLOS statistics, are employed for the estimation of single OGS CFLOS probability and joint CFLOS statistics (OGS network), taking into account the elevation angle and the altitude of the OGSs. For the joint CFLOS statistics it is

assumed that if at least one OGS of the OGSN is not blocked by clouds, then the OGS network is considered as free of clouds. Results assuming GEO and Non GEO satellites are reported.

4.4.1   Single and Joint CFLOS numerical results-GEO satellite

In this sub section CFLOS is computed for stations in Hellenic territory assuming a GEO satellite. The ASTRA GEO satellite at 19.2°E is employed. The statistical parameters of ILWC are derived from ITU-R P.840-6 [ITU840]. In Table 5 the CFLOS statistics as computed employing the proposed methodology are reported. In the 6th column the CFLOS for each single link is estimated and in the last column the joint *CFLOS* considering that at least one of ground terminal is not blocked by clouds is presented, i.e. in the second row assuming that there are only the stations in city of Rhodes and Heraklion, in the third row assuming that there are only the stations in city of Rhodes, Heraklion and Kalamata etc. The temporal and spatial variability of clouds is taken into account. It can be pinpointed that using these stations a 99.9% joint availability is achieved.

Table 5: CFLOS statistics multiple stations in Greece- ASTRA GEO satellite

Location	Lat. (deg)	Lon. (deg)	Alt (m)	Elev. An. (deg)	P_{CFLOS} (%)	DIVERSITY *CFLOS* (%)
City of Rhodes	36.43	28.22	300	46.66	82.0	82.0
Heraklion, Crete	35.33	25.13	250	48.49	75.6	94.9
Kalamata	37.05	22.102	380	46.92	70.7	98.3
Mytilene, Lesvos	39.11	26.54	150	44.08	70.1	99.2
Hymettus Athens, GR	37.96	23.82	1000	45.73	69.3	99.6
Nemea	37.84	22.62	310	45.99	67.9	99.7
City of Corfu	39.62	19.89	145	44.14	66.3	99.8
Thessaloniki	40.64	22.95	350	42.85	60.4	99.9

4.4.2   Single and Joint CFLOS numerical results - LEO satellite

Now single and joint CFLOS statistics are generated assuming a LEO satellite and a hypothetical OGS network in Greece (Ground to LEO). The stations used are presented in Fig. 24. As space segment the Iridium LEO satellite is assumed (altitude: 779km, inclination angle 88.9 deg).

Employing AGI/STK tool kit [AGI], the sub satellite points of the LEO satellite are generated using a specific time resolution. The time resolution of the sub satellite points is selected to be the same with the time resolution of the CFLOS time series. When the LEO satellite is not in the visibility area of the OGS the elevation angle is considered zero. In addition, it is assumed that when the elevation angle is less than 20deg there is no connection with the satellite and again the elevation angle is set zero. For a single OGS the CFLOS statistics are computed given that the LEO satellite is within the visibility area of the station. For the

site diversity scenario the joint CFLOS statistics are computed, given that at least one station is within the visibility area of the satellite. In Fig. 25 the Probability Density Function of elevation angle (given that the elevation angles are higher than 20deg), for a hypothetical OGS located in Heraklion, Crete, Greece, given that the LEO satellite is in the visibility area of the station is reported. Sub-satellite points have been generated for 1 year, with 30sec temporal resolution.
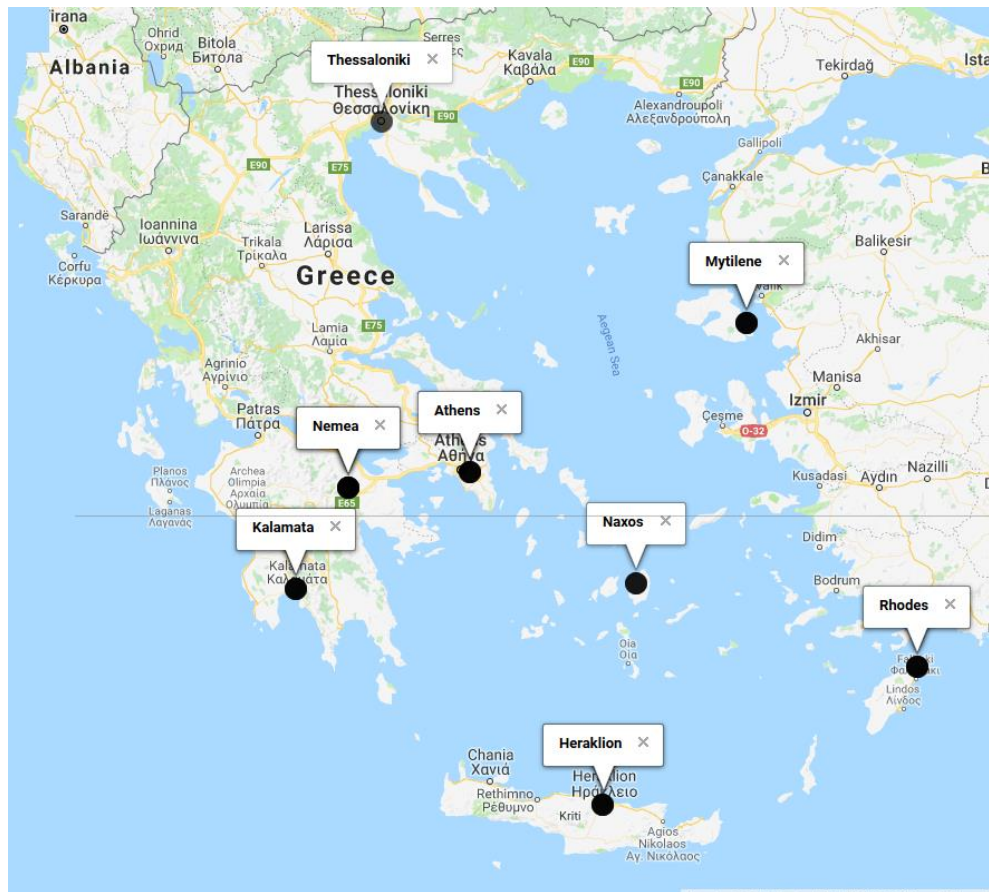
Fig. 24: Hypothetical OGS Network Greece, LEO satellite scenario
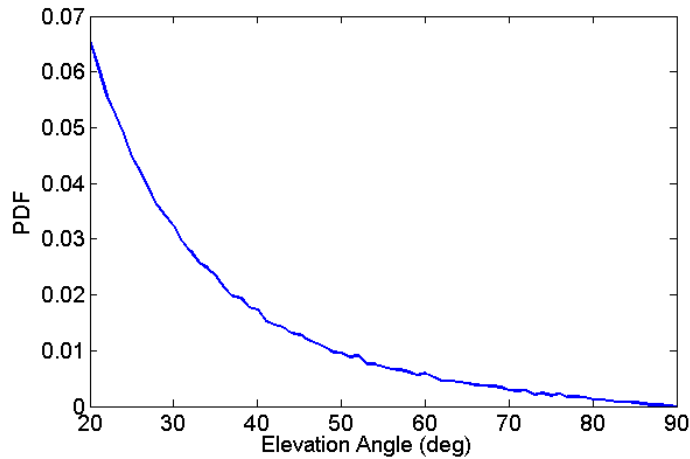
Fig. 25: Elevation Angle PDF Heraklion-Iridium LEO sat.

For the generation of CFLOS statistics the mean statistical parameters of ILWC are derived from ERA Interim database (ECMWF), for years from 2000 until 2016. This data base is different from the one used before. The temporal resolution of both sub satellite points and the CFLOS time series is set as 30sec. In Table 6 CFLOS is computed for each hypothetical OGS.

Table 6: CFLOS probability for single links, LEO satellite communication system

Location	Latitude (deg)	Longitude (deg)	Altitude (m)	Min-Max Elev. Angle(deg)	P_{CFLOS} (%)
Nemea	37.84	22.62	440	20-89.4	55.6
Heraklion, Crete	35.33	25.13	400	20-89.86	69.1
Athens	37.96	23.82	500	20-89.6	62.2
Kalamata	37.05	22.102	400	20-89.6	61.4
City of Rhodes,	36.43	28.22	300	20-89.4	71.7
Mytilene, Lesvos	39.11	26.54	420	20-89.5	64.6
Thessaloniki	40.64	22.95	430	20-89.8	53.5
Naxos	37.09	25.46	500	20-89.3	68.3

Finally, assuming that the above stations form a regional OGSN the joint CFLOS is estimated as 91.32%.

86

4.4.3   Single and Joint CFLOS numerical results – MEO constellation

In this sub section single and joint CFLOS statistics are presented for a MEO constellation system with 12 MEO satellites orbiting at 8062km with inclination angles less than 0.1 deg, similar to the one of O3b [O3b]. A number of fully interconnected optical ground stations (OGSs), which form an OGS network, are employed to cope with cloud coverage applying site diversity technique. OGSs are considered feeder link terminals transmitting information to the MEO satellites, using optical frequencies. It is also assumed that each OGS is equipped with two laser terminals at least. This assumption allows a seamless satellite handover, since the one laser terminal points at the rising satellite and the second one at the descending satellite. It is assumed that each OGS always transmits data to the satellite with the highest elevation angle, among the ones within the visibility area.

Now, employing AGI/STK tool kit [AGI], the sub satellite points of the MEO constellation are generated, using a specific time resolution and/or an orbital period. The time resolution of the sub-satellite points is selected to be the same with the time resolution of ILWC time series. For each station, using the sub satellite points, the elevation angles with each satellite are calculated with the same time resolution. When a satellite is not in the visibility area of the station the elevation angle is considered zero for the calculations and if there are more than one satellite simultaneously in the visibility area of the OGS, the OGS communicates with the satellite with the highest elevation angle.

In Fig. 26, for the 12 MEO satellite constellation, the probability density functions PDFs of elevation angle for three hypothetical OGS are presented. The OGS are located in Heraklion, Greece, Rome, Italy and Paphos, Cyprus. At least one satellite is always in the visibility area of each station.
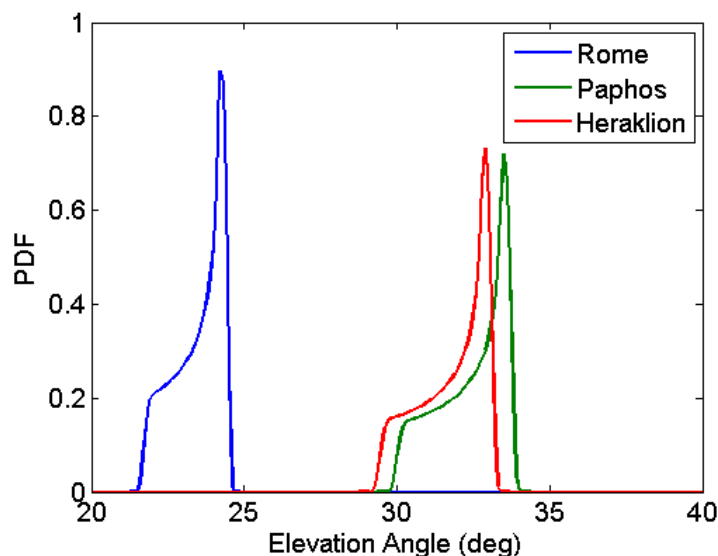
Fig. 26: PDF of elevation angle for three different OGSs with 12 MEO Satellites.

Now, considering a network of 12 OGS, the CFLOS probability for single links is reported. The minimum and maximum elevation angles for each OGS are also presented. The statistical parameters of ILWC have been derived from the monthly database of Era-Interim for the period from 1/1/2009 until 31/12/2015.

Table 7: CFLOS probability, single links, MEO constellation satellite communication system

	Area	Lat. (°N)	Lon. (°E)	Alt. (km)	Min-Max Elevation Angles (deg)	P_{CFLOS} (%)
1	Nemea	37.83	22.6	0.3	26.3 - 29.7	55.30
2	Heraklion	35.24	25.16	0.8	29.33 - 33.14	67.70
3	Catania	37.51	14.95	0.1	26.7 - 30.1	63.34
4	Rome	41.9	12.5	0.1	21.6 - 24.5	52.83
5	Sintra	38.82	-9.3	0.2	25.14 - 28.4	55.98
6	Madrid	40.42	-3.7	0.8	23.3 - 26.35	54.36
7	Barcelona	41.41	2.1	0.3	22.17 - 25.1	57.95
8	Gibraltar	36.14	-5.35	0.2	28.27 - 31.9	58.64
9	Tenerife	28.76	-17.89	2.4	37.15 - 42.2	83.32
10	Paphos	34.77	32.43	0.2	29.9 - 33.8	74.03
11	Toulouse	43.61	1.45	0.2	19.7 - 22.7	40.93
12	Matera	40.67	16.6	0.4	23.01 – 26.03	56.21

It can be noticed, that Tenerife has the highest CFLOS probability, as expected, since the altitude of Tenerife OGS (2.4km a.m.s.l) is high and a lot of clouds range are bellow the OGS.

Now CFLOS statistics for three cases of OGS networks are presented. The 1st OGSN consists of the stations with numbers {10, 7, 12, 5, 1, 11}, the 2nd OGSN with numbers {9, 10, 7, 12, 5, 1, 11} and the 3rd OGSN {10, 2, 3, 12, 1, 4}. The 2nd OGSN is the same with 1st OGSN having added the high altitude station of Tenerife. In Fig. 27, the 1st and 2nd OGSN are exhibited, while in Fig. 28 the third OGSN is depicted.

Fig. 27: 1ˢᵗ & 2ⁿᵈ OGSN-MEO constellation
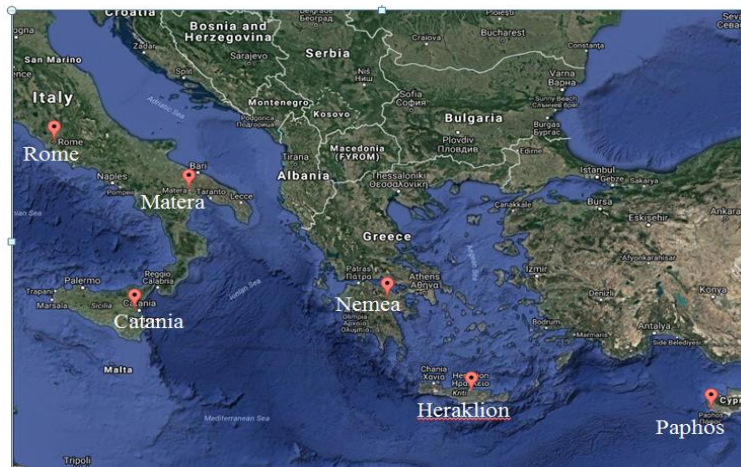
Fig. 28: 3ʳᵈ OGSN-MEO constellation

In

Table 8-Table 10 joint CFLOS probabilities for these three configurations of OGSNs are reported. The CFLOS values in the first row correspond to the first station, in the second row to the joint CFLOS of the two stations, in the third raw to the joint CFLOS of the three stations etc.

Table 8: 1ˢᵗ OGSN Joint CFLOS statistics

OGSs	P_{CFLOS} (%)
{10}	74.03
{10,7}	89.08
{10,7,12}	95.20
{10,7,12,5}	97.88
{10,7,12,5,1}	99.01
{10,7,12,5,1,11}	99.33

Table 9: 2ⁿᵈ OGSN Joint CFLOS statistics

OGSs	P_{CFLOS} (%)
{9}	83.32
{9,10}	95.67
{9,10,7}	98.18
{9,10,7,12}	99.20
{9,10,7,12,5}	99.64
{9,10,7,12,5,1}	99.83
{9,10,7,12,5,1,11}	99.89

Table 10: 3ʳᵈ OGSN Joint CFLOS statistics

OGSs	P_{CFLOS} (%)
{10}	74.03
{10,2}	91.21
{10,2,3}	96.74
{10,2,3,12}	98.40
{10,2,3,12,1}	99.15
{10,2,3,12,1,4}	99.54

From the above joint numerical results it can be seen that for the 1ˢᵗ OGSN, 5 OGSs are required in order to achieve a threshold of 99%, while for the 2ⁿᵈ OGSN (where a high altitude station is used) 4 OGSs may be used to satisfy this threshold. In the 3ʳᵈ OGSN, the threshold of 99% is also achieved with five OGSs.

4.5   OGSN switches

The development and use of space time synthesisers give some additional really important benefits, since valuable statistics from the system point of view can be derived. In this sub section the proposed space time CFLOS synthesizer is employed, in order the average number of OGS switches for an OGSN and the percentage of time that each OGS is selected to transmit data, to be defined.

Therefore, the second and third OGSNs reported in Section 4.4.3 are tested in terms of the average number of OGS switches per year and the percentage of time each OGS is selected to transmit data to the MEO constellation. The main contribution of this sub section is to define the number of switches of the OGSN, assuming that we have an ideal system that is aware (perfect knowledge) of the cloud occurrence time series in each station of the OGSN. More specifically, it is assumed that at every time instant the OGSN is aware of which OGS will have the larger CFLOS duration, i.e. the CFLOS duration is between the current time instant given that that the station is not blocked by clouds (so as it can be selected) and the next time in the future that the clouds will appear and block the slant path. This means that we assume that we are fully and continuously aware when clouds are present on a site and for how long. Consequently, we select to transmit data employing and activating the OGS with the highest CFLOS duration (known as described above). This OGS is named as active OGS. When the active OGS becomes cloud blocked, the next active site is the one with the highest upcoming CFLOS duration that is not blocked at this time instant. This is assumed as an OGS switch. When all stations are blocked we have the outage of the system. After an outage event, if the next active station is the same with the previous active station we do not have an OGS switch, while if the next active (after the outage), differs from the previous active (before outage) then this is an OGS switch. When we go from an active station to outage this is an OGS switch. Here it must be noted that we examine the switches only between the stations and no between the MEO satellites. For example, if the active station (assume OGS#1) transmits data to MEO satellite #1 (the one with the highest elevation angle in the visibility area) and according to the system definition reported in Section 4.4.3, after some minutes the active station OGS#1 will transmit data to MEO satellite #2, because this is now the satellite with the highest elevation angle among the ones in the visibility area and then this is not an OGS switch since the OGS #1 is still the active OGS.

Since the second order statistics are examined, in order to avoid "ping pong" phenomena authors test the OGSN every 10 minutes. It is assumed that the channel will not change for 10 minutes, regarding the clouds. That means that a time resolution of 10 minutes is considered in the proposed methodology presented in the previous section. The time evolution of the ILWC has been taken from the ITU-R P.1853-1 [ITU1853-1].

Now the number of average OGS switches per year for the OGSN #2 is 1768. In Table 11 the percentage of time each OGS is selected is reported.

Table 11: Percentage of time each OGS is selected - OGSN#2, MEO

OGSs	Percentage of OGS USE (%)
{1}	11.51
{5}	11.66
{7}	12.32
{9}	20.31
{10}	27.8
{11}	4.78
{12}	11.5
NO OGS (Outage)	0.12

Now the number of average OGS switches per year for the OGSN 3 is 1810. In Table 12 the percentage of time each OGS is selected is reported.

Table 12: Percentage of time each OGS is selected - OGSN#3, MEO

OGSs	Percentage of OGS USE (%)
{1}	11.45
{2}	20.8
{3}	16.94
{4}	10.25
{10}	28.67
{12}	11.36
NO OGS (Outage)	0.53

An interesting result, which can be pinpointed from Table 11 is that although the OGS #9 (Tenerife) has higher CFLOS probability (see Table 9) than OGS #10 (Paphos), for OGSN #2 the hypothetical OGS in Paphos is selected for higher percentage of time. This may come from the spatial and temporal correlation of the whole OGSN (all the stations forming the OGSN#2). Thus, it is important to design CFLOS tools which take into account the temporal and spatial variability/correlation of clouds.

5   CLOUD FREE LINE OF SIGHT THEORETICAL MODELING

As described in previous sections, the estimation of CFLOS probability for a single link and a spatial diversity scenario (OGSN) is really crucial for optical satellite communication systems. In previous sections, methodologies for the estimation of single and joint CFLOS probability using Stochastic Differential Equations were reported.

However, those methodologies can be proved difficult to be implemented. Therefore, in this chapter, a simple physical and mathematical theoretical model for the prediction of CFLOS probability along a single slant path and for separated on spatial domain multiple optical satellite links is presented. For the accurate evaluation of CFLOS the elevation angle of the slant path, the altitude of ground stations and the spatial variability of clouds are considered.

The methodology is based on the assumption that ILWC follows lognormal distribution and on the well-defined relationship between ILWC and liquid water density (36). Moreover, the correlation of ILWC in spatial domain is taken into account and it is assumed that the statistical parameters of ILWC are constant along the slant path. In addition, CFLOS probability for simultaneously available optical links for the application of spatial multiplexing transmission techniques is estimated.

The remainder of the Chapter is structured as follows: In Section 5.1 the methodology for the estimation of CFLOS probability for a single link is presented. In Section 5.2 the methodology for the prediction of the joint CFLOS probability for a spatial diversity scenario is shown. In Section 5.3 CFLOS probability for a given number of simultaneously available links for spatial multiplexing transmission technique is reported and in Section 5.4 some numerical and validation results using the proposed methodologies are exhibited.

5.1   CFLOS Theoretical Modelling for Single Optical Satellite link

As described in previous sections, cloud masses can be defined knowing the cloud base, the integrated liquid water content, the liquid water content and the vertical extent of clouds. For slant paths it is assumed, that clouds impair the link if a cloud formation is present at the slant path. Considering a satellite slant path through the cloud layer (See Fig. 29) then the probability of CFLOS is equal to the probability that the line integral of the liquid water density ($\tilde{w}$) over the line of slant path (C) is equal to zero, i.e.:

$$P_{CFLOS} = P\left(\int_C \tilde{w} \, ds = 0 \right) \qquad (45)$$

where $\int_C \tilde{w}ds$ is the line integral of liquid water density over the line of slant path and $C(x,y,h)$. The liquid water density at a point (x,y,h) is given by expression (36) of Section 3.2, but without dependence of time. For better clarity the expression is reported again here:

$$\tilde{w}(x,y,h) = \begin{cases} \dfrac{L(x,y)}{(c_2)^{c_1}\,\Gamma(c_1)}(z-h_0)^{c_1-1}\,e^{-(z-h_0)/c_2} & \text{for } h \geq h_0 \\ 0 & \text{for } h < h_0 \end{cases}$$

$$c_1(L) = 4.27\, e^{-4.93(L+0.06)} + 54.12\, e^{-61.25\,(L+0.06)} + 1.71$$

$$c_2(L) = 3.17\, c_1^{-3.04} + 0.074$$

(46)

where $L(x,y)$ is the integrated liquid water content at point (x,y), h_0 is the cloud base height and $\Gamma(\ )$ is the well-known gamma function.
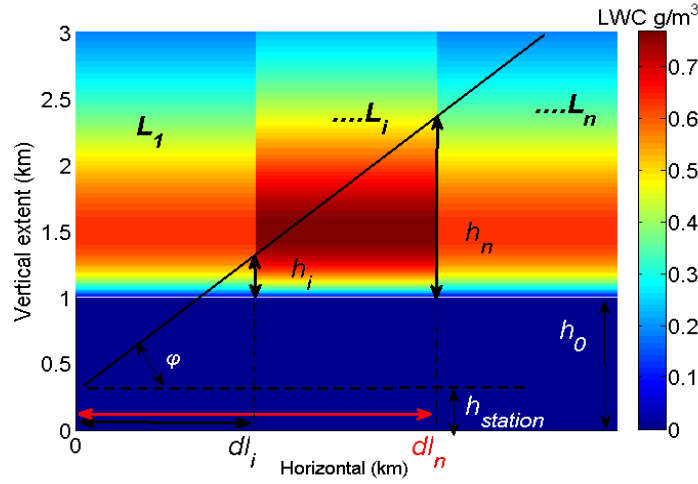
Fig. 29: Slant path configuration – Cloud vertical extent snapshot

It is assumed that in an horizontal plane with an area of $1km^2$, i.e. the plane defined by a line of 1 km on x-axis and 1 km on y-axis, the ILWC is constant, as shown in Fig. 29. Then, the line integral of (45) can be written as:

$$P_{CFLOS} = P\left(\sum_{i=1}^{n}\int_{C_i}\tilde{w}ds = 0\right)$$

(47)

where C_i is the line of slant path in which the ILWC remains constant and n is the number of grids so as the whole slant path is taken into account.

Therefore, on every line C_i, $\tilde{w}$ depends only on height. In order to consider that a slant path is affected by clouds, the top height of the cloud (h_{top}) at every point must be higher than the lowest point of every line C_i. Considering the geometry of Fig. 29, the lowest point above clouds on line C_i is given by:

94

$$h_{i,th} = dl_i \cdot \tan(\varphi) + h_{station} - h_0 \tag{48}$$

where dl_i is the distance on the horizontal plane between the two lowest points of two lines, i.e. 1 km in our case, φ is the elevation angle, $h_{station}$ the altitude above mean sea level of the station and h_0 is the height of cloud base. Therefore, (47) becomes:

$$P_{CFLOS} = P(\Delta h_1 < h_{1,th}, ..., \Delta h_i < h_{i,th}, ..., \Delta h_n < h_{n,th}) \tag{49}$$

where $\Delta h_i = h_{i,top} - h_0$ for the line C_i.

From [Luini14], it is considered that $\tilde{w}_i(h_i, L_i) \to 0$ for $\tilde{w}_i(h) \leq 0.06 L_i$ and the top cloud height on the 3-D plane defined on line C_i, where L is constant can be calculated through the solution of the following transcendental equation:

$$\int_{h_0}^{h_{i,top}} \tilde{w}_i(h_i, L_i) dh_i = 0.94 L_i \Leftrightarrow \gamma\left(c_{1,i}, \left(h_{i,top} - h_0\right)/c_{2,i}\right)/\Gamma\left(c_{1,i}\right) = 0.94 \tag{50}$$

where $\gamma(\ )$ is the incomplete gamma function.

Through (50), the explicit relation between the integrated liquid water content and the vertical extent of the cloud (h_{top}-h_0) can be calculated.
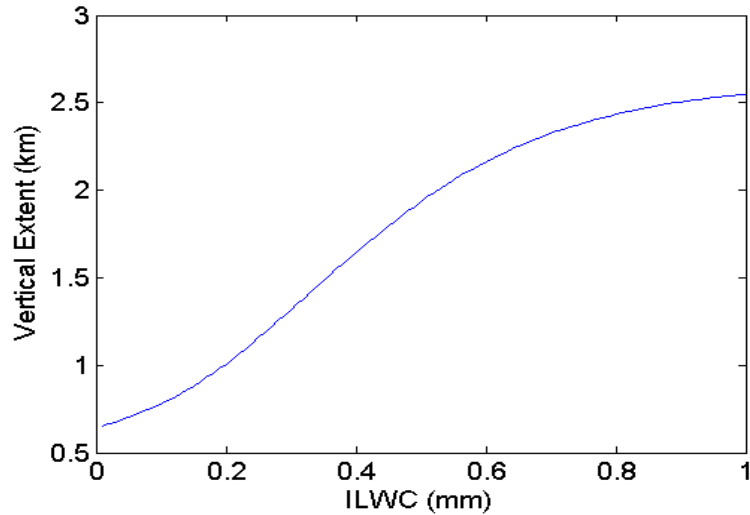
Fig. 30: Vertical extent of clouds vs ILWC

The relation between ILWC and the vertical extent of the clouds is numerically evaluated in Fig. 30. Vertical extent is an increasing function of ILWC and so (50) has a single and unique solution. Therefore, (49) can be written in terms of ILWC using (50) as:

$$P_{CFLOS} = P\left(L_1 < L_{1,th}, L_2 < L_{2,th}, ..., L_n < L_{n,th}\right) \tag{51}$$

As described in previous Sections ILWC can be modelled as a Gaussian low pass process, truncated to a desired threshold to match the desired cloud probability occurrence. Thus using the normally distributed random variables $u_i = \left(\ln(L_i) - m_i\right)/\sigma_i$ where m_i, σ_i are the mean value and standard deviation of grid point i respectively the CFLOS probability is given as:

$$
\begin{aligned}
P_{CFLOS} &= P\left(u_1 < a_{1,th}, .., u_n < a_{n,th}\right) = \\
&= \int_{-\infty}^{a_{1,th}} .. \int_{-\infty}^{a_{n,th}} f_{u_1..u_n}\left(u_1, .., u_n\right) \cdot du_1 \cdot \cdot du_n
\end{aligned} \tag{52}
$$

where $f_{u_1..u_n}$ is the pdf of the multivariate normal distribution [Papoulis02], $1...n$ is the number of $1 \times 1 \text{km}^2$ grids needed so as the whole slant path is taken into account.

The elements of the correlation matrix for the random variables u_i are calculated employing the correlation factor reported in Section 3.1.

Finally $\alpha_{i,th}(i=1,...,n)$ are the truncation thresholds for each grid, given according to the next formula based on [ITU1853-1]:

$$a_{i,th} = Q^{-1}\left(P_{CLW_i} \cdot Q\left(\ln\left(\left(\frac{L_{i,th}}{\exp(m_i)}\right)\frac{1}{\sigma_i}\right)\right)\right) \tag{53}$$

where as described in Section 3.1 m_i, σ_i, are the mean value and standard deviation of $\ln(L)$ and P_{clwi} is the probability that L exceeds 0 mm for a single grid. It can be assumed that the statistical parameters of $ln(L)$ (i.e. m, σ, P_{clw}) are constant along the slant path. Therefore they are the same for all grids and they only depend on the location of the station.

For the cloud base $h_0 (km)$ local available statistics may be used. Otherwise, cloud base values can be derived from a proposed distribution in [Luini14], and then the mean value of P_{CFLOS} is calculated. h_0 can be considered constant in a target area [Luini14], Section 3.2.

5.2   CFLOS Theoretical Modeling for Multiple Optical Satellite links

In this Section a theoretical methodology for the estimation of joint CFLOS probability P_{CFLOS}^{joint} or multiple optical links separated on spatial domain in a site diversity scenario is proposed. The methodology takes advantage of the use of the model developed in Section 5.1

The joint CFLOS probability for N links is the probability that at least one station is not affected by clouds, i.e.:

$$P_{CFLOS}^{\text{joint}} = 1 - P\left(\int_{sp^1} \tilde{w}ds > 0, ..., \int_{sp^N} \tilde{w}ds > 0 \right) \tag{54}$$

where SL^i is the line of the slant path on link i, $i=1,...,N$. Using (47), the probability that clouds are present through a single satellite slant path is:

$$P_{Cloud}^i = P\left(\int_{sp^i} \tilde{w}ds > 0 \right) = 1 - P_{CFLOS}^i \tag{55}$$

where P_{CFLOS}^i is calculated employing the methodology presented in the previous section. Considering the random variable that clouds present in a single slant path is a binary variable, the following may be assumed for P_{Cloud}^i:

$$P_{Cloud}^i = Q\left(\alpha_{sp,th}^i \right) \tag{56}$$

Therefore, the threshold value of zero mean and unity variance Gaussian random variable (u_{sp}^i) over which clouds are present in a single link is:

$$\alpha_{sp,th}^i = Q^{-1}\left(P_{Cloud}^i \right) \tag{57}$$

The joint CFLOS probability, i.e. the probability that at least one station is free of clouds, is given by:

$$P_{CFLOS}^{\text{joint}} = 1 - P\left(u_{sp}^1 \geq a_{sp,th}^1, ..., u_{sp}^N \geq a_{sp,th}^N \right) \tag{58}$$

The joint Complementary Cumulative Distribution Function (CCDF), for the k variables can be calculated from the joint CDFs according to [Papoulis02]. Then based on (57) we conclude on:

$$P^{Jo\text{int}}{}_{CFLOS} = 1 - \int_{a_{sp,th}^1}^{\infty} .. \int_{a_{sp,th}^N}^{\infty} f_{u_1..u_N}\left(u_1, .., u_N \right) \cdot du_1 \cdot\cdot du_N \tag{59}$$

while $f_{u_{sp}^1 u_{sp}^2 ... u_{sp}^N}$ are the pdf of multivariate normal distribution [Papoulis02]. The mean value of the normal random variables is zero, the standard deviation is one and the values of correlation matrix are also calculated through the well-defined correlation expression proposed in [Luini14] and given in Section 3.1. The distances used are the distances between the slant paths, i.e. the Euclidean distances of the ground terminals.

5.3   Simultaneously Joint CFLOS Statistics for an OGSN

In this sub section the probability of two or more stations not simultaneously blocked by clouds is defined. In case that two or more stations are simultaneously under cloud-free line-of-sight conditions, then spatial multiplexing technique can be used in order to increase the transmitted capacity.

The probability that clouds are not present in 2 or more stations from *s* total is given by [SenGupta09]:

$$P_{SA}(p) = 1 - \sum_{v=0}^{p-1} P(v) \tag{60}$$

where *p* is the number of ground stations that we want to be at least active, *P(0)* is the probability that no station is available, i.e. 1- P_{CFLOS}^{joint} and *P(v)* is the probability that exactly *v* stations are available and can be calculated by [SenGupta09]:

$$P(v) = \sum_{l=0}^{N-v} (-1)^l \binom{v+l}{v} S_l$$

$$S_l = \sum_{1 \le i_1 < i_2 < ... < i_{v+N}} \sum^{v+l} \cdots \sum P(\bigcap_{j=1}^{v+l} u_{sp}^{i_j} < a_{sp,th}^{i_j}) \tag{61}$$

l is the number of the available stations.

5.4   CFLOS Theoretical Modeling Simulation Results

The analytical formulations presented in this Chapter are employed for the estimation of single and joint CFLOS statistics.

Firstly, the proposed formulas for the prediction of CFLOS for the single slant path are validated with simulation data from the analytical stochastic model presented in Section 4.2 (Fig.31). The solid lines are the predicted CFLOS values using the methodology in Section 4.2. and the symbols are the predicted CFLOS values using the methodology in Section 5.1. The statistical parameters for ILWC needed are derived from both methodologies from ITU-R P.840-6 [ITU840]. The order of the magnitude of the variation of P_{CFLOS} with elevation angle comes from the high spatial correlation of ILWC along the slant path.
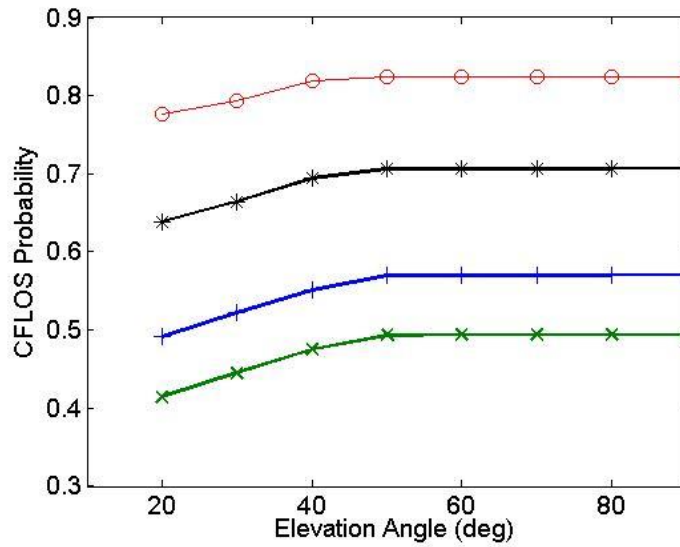
Fig. 31: CFLOS probability vs. elevation angle for single links: o-Paphos, *-Madrid, +-Lyon, x-Stockholm

To continue, in Table 13, numerical results for a site diversity scenario with hypothetical links placed in Greece are presented. The ASTRA satellite at 23.5°E is considered as space segment. In a pool of 10 hypothetical stations located in Greece and the CFLOS probability of each single link is computed taking into account the elevation angle and the altitude of each hypothetical station.

Table 13: Single OGSs CFLOS

Area	Lat. (^{o}N)	Lon. (^{o}E)	Alt. (m)	Elevation Angles(deg)	P_{CFLOS} (%)
Athens	37.98	23.78	300	43.19	69.2
Kea	37.61	24.32	250	46.39	72.3
Taygetos Mountain	36.95	22.35	1700	47.12	71.38
Korinthos	37.94	22.9	350	46.15	68.2
City of Rhodes	36.4	28.2	200	47.47	82.0
Larissa	39.64	22.42	300	44.1	63.8
City of Limnos	39.92	25.14	320	43.78	67.4
Lefkada	38.66	20.63	330	45.1	67.5
Psiloritis Mountain Crete	35.23	24.77	1900	49	79.2
Skopelos	39.11	23.71	250	44.72	68.4

Now using the above stations we want to compute the joint CFLOS in order to achieve a 99.8% availability. In Table 14 the joint CFLOS values in the last column are the corresponding ones for double, triple etc. multiple site diversity schemes.

Table 14: Joint CFLOS, OGSN Greece

Area	Lat. (°N)	Lon. (°E)	Alt. (m)	Elevation Angles(deg)	P_{CFLOS} (%)
City of Rhodes	36.4	28.2	200	47.47	82.0
Psiloritis Mountain Crete	35.23	24.77	1900	49	95.12
Lefkada	38.66	20.63	330	45.1	98.21
City of Limnos	39.92	25.14	320	43.78	99.22
Taygetos Mountain	36.95	22.35	1700	47.12	99.6
Kea	37.61	24.32	250	46.39	99.76
Larissa	39.64	22.42	300	44.1	99.87

Now for a hypothetical scenario with the first 4 stations of Table 14 the probability of having simultaneously available at least 2 or 3 stations out of 4 is calculated. For 2 available stations the $P_{SA}(2) = 93.16\%$ and for 3 available stations $P_{SA}(3) = 71.63\%$. These probabilities can be used in order to evaluate various joint transmission techniques.

100

6   CFLOS MONTHLY STATISTICS-OGSN DIMENSIONING

From Section 2.2.2.3 it can be pinpointed that cloud coverage exhibits remarkable monthly variations which cannot be observed when yearly averages are used. There are also great differences in the monthly cloud coverage probabilities (maxima and minima) between the two hemispheres. The above observations should not be omitted for the design of OGSNs. For example, in Fig. 32 cloud coverage per month (M) for one station in Northern Hemisphere, South Mountain, California, and another in Southern Hemisphere, Malargue, Argentina, is presented along with the respective yearly averages (Y). The cloud coverage statistics are derived from the ERA Interim database for the year 2000.
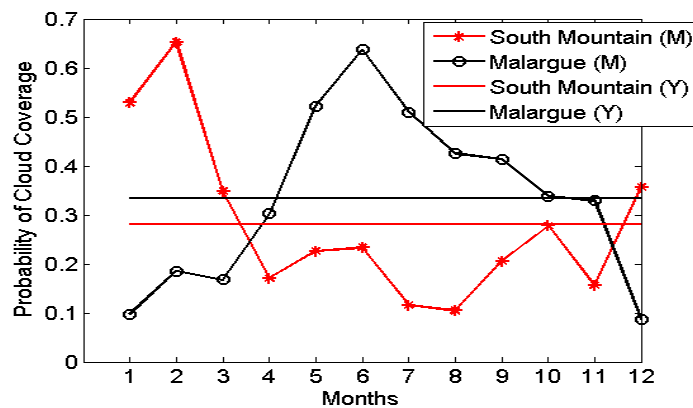
Fig. 32: Cloud Coverage Monthly (M)-Yearly(Y), North/South Hemisphere

Consequently, it can be observed that monthly-based statistics must be taken into account for the estimation of CFLOS and are crucial for the development of algorithms for optimum, robust and cost effective selection of OGSs. As described so far, CFLOS can be estimated using ILWC statistics and ILWC annual long term statistics can be sufficiently described by lognormal distribution.

Firstly, in this Chapter, in Section 6.1 it is shown that ILWC monthly statistics can be sufficiently described by lognormal distribution. Then, in Section 6.2, the CFLOS synthesizer described in Section 4.2 is used for the estimation of monthly CFLOS statistics and numerical results are reported. To continue, in Section 6.3 analytical formulas for the estimation of single and joint monthly CFLOS availability are reported. Additionally, two novel optimization algorithms for the optimum selection of OGS for mitigation of cloud coverage are reported. These algorithms are aware of the clouds monthly variability and take advantage of the hemisphere differences. The main contribution of these algorithms is that they guarantee a minimum availability per month, which is not necessarily the same for each month. The benefits of using optical stations in different hemispheres are highlighted. Additionally, an optimization algorithm for the identification of active stations per month is also reported. Finally some numerical results are exhibited.

6.1 ILWC Monthly Statistics-Distribution

For the characterization of monthly ILWC statistics, inputs derived from ERA-Interim database are used. Specifically, total column cloud liquid water data for 11 years, from 2006 to 2016 with temporal resolution of one sample every 6 hours and with spatial resolution of $0.75^o \times 0.75^o$ are employed. For this analysis data for 30 different places dispersed all around North/South America and Europe (not in tropical areas or oceans) is used. ILWC data are grouped for each place and month and then the long term statistics in terms of CCDF are tested with lognormal, Weibull and gamma distribution. In order to guarantee the accuracy of the proposed distribution the Root Mean Square (RMS) error between the fitted CCDFs and the empirical CCDFS derived from Era Interim data is calculated, for an interval of time percentage from 99% to 0.8% [Jeannin08], for each place and month. Then for each place the maximum and the average monthly RMS error is computed, similarly to [Jeannin08]. According to the executed analysis, ILWC monthly statistics can be best described by the conditional (i.e., knowing that ILWC>0) lognormal distribution for the regions of interest. For all the locations that have been chosen, for the analysis the mean RMS error is less than 8% while the maximum RMS error is less than 15%. For example the average RMS errors for 7 different places are given in Table 15:

Table 15: Average RMS error-ILWC monthly distribution

Place	Average RMS error (%)
Dallas (USA)	4
Buenos Aires (Argentina)	3.6
Lyon (France)	2
Manchester (England)	1.6
Berlin (Germany)	2
Madrid (Spain)	2.8
Lisbon (Portugal)	3

In Fig. 33 an example of ILWC derived from Era Interim data and the fitted lognormal distribution for two months in Lyon (France), is exhibited. The accuracy of the predicted results may be improved if data with higher spatial resolution is used.
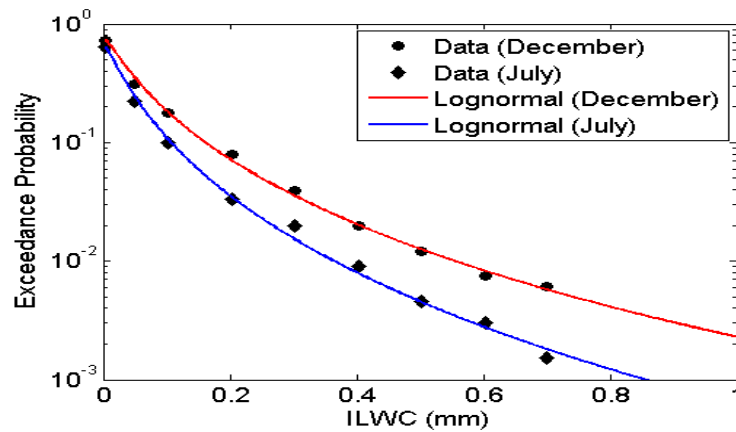
Fig. 33: Monthly ILWC CCDF derived from ERA Interim database for Lyon France

6.2 CFLOS Time Series Based on Monthly ILWC statistics

Since the monthly ILWC long term statistics can be sufficiently described by the conditional lognormal distribution, the CFLOS space time synthesizer presented in Section 4.2 can be employed for the generation of seasonal and monthly CFLOS statistics, capturing the temporal and spatial variability of clouds and taking into account the elevation angle and the altitude of the link. However, in this case as statistical parameters of the logarithm of ILWC, monthly parameters are used. These statistical parameters can be extracted using the ERA Interim or other databases and employing the fitting methodology presented in the previous section, for each place of interest for either one or multiple years. Therefore, a methodology for the generation of CFLOS time series is exhibited. The following steps are followed for each month:

- The monthly statistical parameters of the logarithm of ILWC for each place of interest are computed according to the fitting procedure reported. Otherwise, the methodology reported in [Luini14] can be employed.
- Using the monthly statistical parameters 2D ILWC time series are generated for each month, taking into account the temporal and spatial variability of clouds (see Section 3.1).
- 2D ILWC time series are converted to 3D time series (see Section 3.2) for each month.
- CFLOS time series are computed for each month, taking into account the elevation angle and the altitude of each link (see Section 4.2).
- Single and Joint monthly CFLOS statistics are computed (see Section 4.2).

Now, the proposed methodology is employed for the generation of monthly CFLOS time series and the estimation of single and joint monthly CFLOS statistics in North and South America. The statistical parameters have been derived from the monthly database of Era-Interim, for the period from 1/1/2009 to 31/12/2015. The hypothetical optical links, which are used for the numerical results, are shown in Table 16.

103

Table 16: Hypothetical OGS-Different Hemispheres

Area	Lat. (°N)	Lon. (°E)	Elevation Angles(deg)	Alt. (m)	Hemisphere
Santiago, Chile	-33.44	-76.68	50.51	600	South
Malargüe, Argentina	-35.483	-69.58	48.04	1400	South
Steele Valley, Carlifornia USA	33.76	-117.32	32.0	612	North
Vernon, Texas, USA	34.218	-99.40	43.57	400	North
Santiago, Chile	-33.44	-76.68	50.51	600	South

In Fig. 34 monthly CFLOS statistics are depicted for two stations one in the north and another in the south hemisphere, using in one hand monthly and on the other hand annual statistical parameters. The results reveal that using annual statistical parameters, the monthly variability of CFLOS probability and the variability between the two hemispheres cannot be captured. Thus, the use of annual statistical parameters cannot guarantee a robust optical ground station dimensioning.
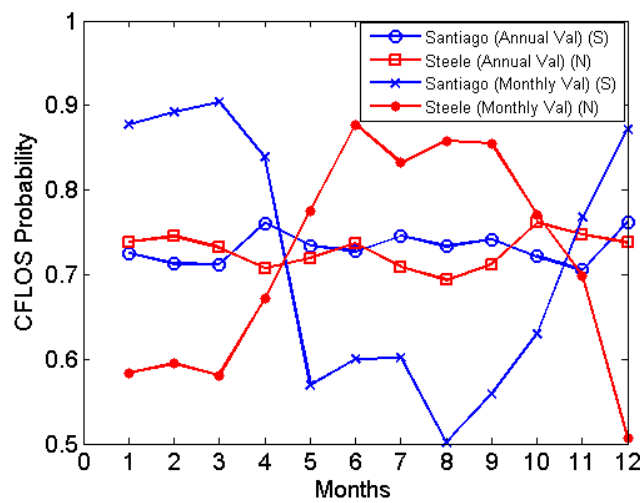
Fig. 34: Monthly CFLOS Probability using annual and monthly statistical parameters (North/South hemisphere)

Except from the statistics for the single links, joint CFLOS statistics (for an OGSN) are also presented. For the double site diversity scenario the stations of Santiago and Steele Valley are used, for the triple the station of Malargüe is added to the previous ones and finally for the quadruple scenario the station at Vernon is added. It can be observed that for double scenario there is one station from the south hemisphere and another from the north etc.

In Fig. 35 and Fig. 36 the monthly joint CFLOS probability for the double, triple and quadruple spatial diversity scheme is computed, using annual and monthly statistical parameters as input to the methodology.
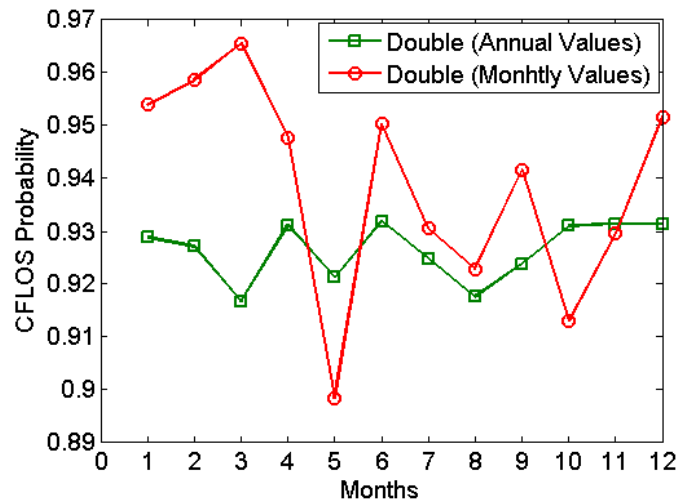
Fig. 35: Joint Monthly CFLOS Probability for double diversity scenario (annual and statistical parameters are used).
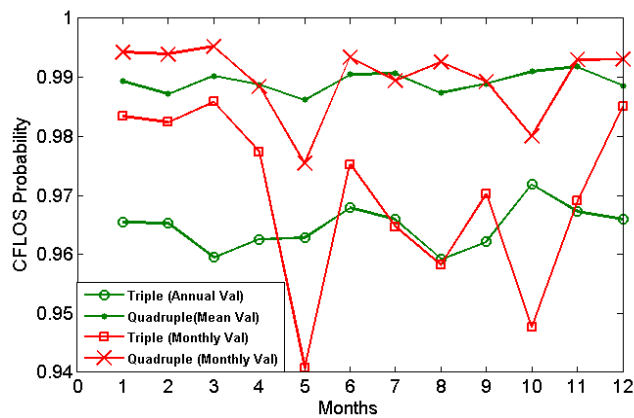
Fig. 36: Joint Monthly CFLOS Probability for triple and quadruple spatial diversity scenario (annual and statistical parameters are used).

From this section it can be easily observed the necessity of using monthly statistical parameters, while the employment of optical ground stations located in different hemispheres can be proved really beneficial.

105

6.3 OGSN Dimensioning-Monthly CFLOS formulation

In this sub section, firstly, the methodology presented in Chapter 5 is modified, in order that analytical formulas for the estimation of single and joint monthly CFLOS availability are presented. Moreover, 2 monthly aware algorithms for the optimum OGS selection are reported . The benefits of using optical stations in different hemispheres are highlighted. Finally, an optimization algorithm for the identification of active stations per month is also reported.

6.3.1 CFLOS Analytical Formulas-Monthly Statistics

To begin with, based on Section 5, assuming that the random variable that clouds are present in a satellite link is a binary variable, the joint monthly CFLOS availability is given according to the next expression Section 5.2:

$$
\begin{aligned}
P_{avail,m}(i_1, i_2, \ldots, i_N) &= 1 - P\left(u_{i_1} > a_{i_1,m}^{sp\_th}, .., u_{i_N} > a_{i_N,m}^{sp\_th}\right) = \\
&= 1 - \int_{a_{i_1,m}^{sp\_th}}^{+\infty} \int_{a_{i_2,m}^{sp\_th}}^{+\infty} \cdots \int_{a_{i_N,m}^{sp\_th}}^{+\infty} f_{u_{i_1}..u_{i_N}}\left(u_{i_1}, .., u_{i_N}\right) du_{i_1} du_{i_2} \ldots du_{i_N}
\end{aligned}
\tag{62}
$$

where $m=1..12$ represents each month, $(i_1, \ldots, i_N)$ represent the stations which constitute the satellite optical network and $f_{u_{i_1}..u_{i_N}}\left(u_{i_1}, .., u_{i_N}\right)$ is the pdf of multivariate normal distribution (MVND) of the N stations. For the computation of MVND, the spatial correlation matrix of the random variables u_i is needed (see Section 5). Spatial correlation is computed according to expression (32). $a_{i_N,m}^{sp\_th} = Q^{-1}(P_{N,CLW,m})$ is the threshold value, of zero mean and unity variance Gaussian variable u_{i_N} , over which clouds are present, in a single link for each month m. $P_{NCLW,m}$ is the probability of cloud occurrence for each month, for each link taking into account the whole slant path, the elevation angle and the altitude of the station computed as $P_{N,CLW,m} = 1 - P_{N,CFLOS,m}$, where $P_{N,CFLOS,m}$ is the CFLOS probability of the station for each month. Employing the definition of CFLOS probability over a slant path shown in Section 5.1, and assuming that ILWC is constant in a horizontal plane of 1km^2 $P_{NCFLOS,m}$, for each link it can be written according to the following expression :

$$
\begin{aligned}
P_{N,CFLOS,m} &= P\left(w_{1,m} < a^{th}_{1,m}, .., w_{n,m} < a^{th}_{n,m}\right) = \\
&= \int_{-\infty}^{a^{th}_{1,m}} \cdots \int_{-\infty}^{a^{th}_{n,m}} f_{w_{1,m}..w_{n,m}}\left(w_{1,m}, .., w_{n,m}\right) \cdot dw_{1,m} \cdots dw_{n,m} \\
m &= 1 \ldots 12
\end{aligned}
\tag{63}
$$

where $f_{w_{1,m}..w_{n,m}}\left(w_{1,m}, .., w_{n,m}\right)$ is the multivariate normal distribution of the whole slant path, and $1\ldots n$ is the number of 1x1km^2 grids needed so as the whole slant path is taken into account. The variable m is an

indicator of the month, with 1 representing January and 12 December. The truncation thresholds for each month for the single link ($a^{th}_{i,m}$) are given from the next expression:

$$a^{th}_{i,m}, = Q^{-1}\left(P_{CLW,m} Q\left(\ln\left(\left(\frac{L^{th}_{i,m}}{\exp(\mu_m)} \right)\frac{1}{\sigma_m} \right) \right) \right) \tag{64}$$

$$m = 1..12, i = 1..n$$

where $L^{th}_{i,m}$ is computed according to Section 5.1. The variables μ_m, σ_m are the mean value and standard deviation of $ln(L_m)$, while $P_{CLW,m}$ is the probability that L_m exceeds 0 mm for each month for each link. These statistical parameters can be extracted using the ERA Interim or other databases and employing the fitting methodology presented in the previous section, for each place of interest for either one or multiple years.

Now the above expressions will be used for the development of algorithms, for the optimum selection of OGS for the mitigation of cloud coverage provided that a minimum availability requirement for each month is satisfied.

To begin with the problem formulation, it is assumed that a set $V = \{1, 2, \ldots, N\}$ of all the possible OGSs is defined ($1...N$ available stations). The subset with the minimum cardinality (minimum number of stations) that fulfils an availability constraint per month, must be optimum selected. Thus the optimization problem can be expressed as:

$$\min_{\{i_1,i_2,\ldots,i_\Omega\}\subseteq V} \Omega \qquad \text{s.t.} \quad P_{avail,m}(i_1,i_2,\ldots,i_\Omega) \geq P^{th}_{avail,m}, \quad 1 \leq m \leq 12 \tag{65}$$

where Ω is the cardinality of the set of selected OGSs, $P^{th}_{avail,m}$ is the minimum required availability for month m, and $P_{avail,m}(i_1,i_2,\ldots,i_\Omega)$ is the availability achieved for month m by selecting the subset $\{i_1,i_2,\ldots,i_\Omega\}$ of OGSs. The availability is given through the methodology defined so far in this subsection, taking into account the spatial correlation of clouds and the monthly statistical parameters for each place of interest.

Now 2 different algorithms will be proposed for solving this optimization problem:

6.3.2 Exhaustive Search Algorithm (ESA)

The first method is to check all the possible OGSs subsets, i.e. all the Ω-combinations ($1<\Omega<N$) of the set V, starting from $\Omega=1$ and increasing the value of Ω by 1, until the smallest Ω for which there is an Ω-combination that satisfies all the availability constraints is found. When we find this value of Ω, Ω^*, we select the Ω^*-combination that maximizes the quantity $\min_{1\leq m\leq 12}\left\{P_{avail,m}(i_1,i_2,\ldots,i_{\Omega^*})/P^{th}_{avail,m}\right\}$ among all the Ω^*-combinations. The Exhaustive Search Algorithm requires at most $\sum_{k=1}^{N}C(N,k)=2^N-1=O(2^N)$ comparisons, and

so it is exponential with the number of OGSs. Although optimal, this algorithm is impracticable, especially when N is relatively large.

6.3.3 Cost function-based Heuristic Algorithm (CHA)

For this algorithm a set W that contains the selected OGSs so far and it is initially empty ($W = \varnothing$) is defined. At each step, the following cost function for all OGSs that are not selected yet: $\cos t(i) = \sum_{m=1}^{12} \left(\min\left\{ P_{avail,m}\left(W \cup \{i\}\right) - P_{avail,m}^{th}, 0 \right\} \right)^2$, $i \in V \setminus W$ is calculated. This cost function measures the total violation of the constraints, when an OGS i is added to the set W of currently selected OGSs. To continue, the OGS that minimizes the cost function is added to the set w. The CHA terminates when all the constraints are satisfied.

This algorithm requires at most $\sum_{j=0}^{N-1}(N-j) = N(N+1)/2 = O(N^2)$ comparisons, thus having polynomial time complexity. Hence, the Cost function-based Heuristic Algorithm is a highly efficient algorithm.

6.3.4 Active OGSs per month

From the previous sections the stations that must be installed, in order that an availability threshold per month is achieved, can be found. However, not all of these stations must be active every month. In this section a methodology is defined for the determination of the stations that should be active in each month, among the ones selected using any of the previous optimization algorithms. If we denote by w^* the set of OGSs, that were selected using one of the previous algorithms, we seek to find a subset of W^* (possibly different) for each month that satisfies the availability constraint. Particularly, we have to solve the following optimization problem, to find the active OGSs for month m $(1 \le m \le 12)$:

$$\min_{\{i_1,i_2,\ldots,i_\Omega\} \subseteq W^*} \Omega \qquad \text{s.t.} \quad P_{avail,m}(i_1, i_2, \ldots, i_\Omega) \ge P_{avail,m}^{th} \tag{66}$$

This problem can be heuristically solved using a modified version of CHA for the selected stations. The algorithm terminates when the constraint in (66) is satisfied.

6.3.5 OGSN Dimensioning Numerical Results

In Table 17 a pool of 17 stations in North and South America are reported. The set of the first 15 OGSs are used for the OGSN dimensioning. For all the simulations it is assumed that for each month we have the same availability threshold i.e. as space segment a GEO satellite at 77deg W is considered. For the statistical parameters of ILWC the same data set as in Section 6.1 is used and for the estimation of availability the methodology proposed in this Section 6.3 is employed.

Table 17: OGS pool-OGSN Dimensioning

	Area	Lat. (^{o}N)	Lon. (^{o}E)	Alt. (km)	Elevation Angles (deg)
1	Santiago	-33.43	-70.64	0.3	50.5
2	Steele V.	33.76	-117.3	0.6	32.0
3	Vernon	34.21	-99.4	0.4	43.6
4	Buenos Aires	-34.6	-58.41	0.3	45.2
5	Oklahoma	35.44	-97.53	0.45	43.4
6	Maryland	39.38	-77.08	0.22	44.4
7	Lurin	-12.28	-76.85	0.1	75.6
8	Sao Paulo	-23.55	-46.65	0.7	46.3
9	Washington	39.9	-77.04	0.2	43.9
10	Las Vegas	36.12	-115.2	0.65	32.0
11	Dallas	32.74	-96.9	0.16	46.3
12	Lima	-11.94	-76.72	0.8	76.0
13	S. Mountain (CA)	34.33	-118.99	0.4	30.4
14	Manassas	38.78	-77.57	0.12	45.1
15	Malargue	-35.48	-69.59	1.4	48.1
16	Kit Peak	31.96	-111.6	2.2	37.4
17	Calama	-22.5	-68.69	2	62.1

In Fig. 37 the number of selected OGSs versus the required availability P_{avail}^{th} for the proposed optimization algorithms, is illustrated. CHA selects the same number of OGSs compared to ESA, for all the values of P_{avail}^{th}. For $P_{avail}^{th} = 99.9\%$, the selected OGSs for installation are {1,3,4,7,10,13,15}, {10,1,7,3,15,13,4} using ESA and CHA respectively. For CHA the results are given in order of selection. Both algorithms select the same OGSs.
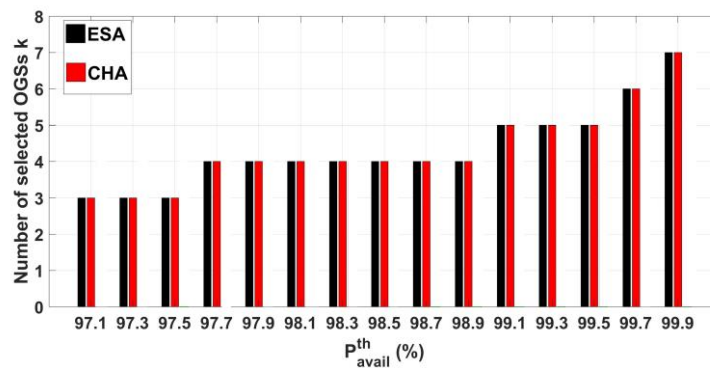
Fig. 37: The number of selected OGSs k vs P_{avail}^{th} for the proposed optimization algorithms

After the selection of the 7 OGSs for installation, the set of active OGSs per month is given in Table 18. The last column contains the monthly availability of active OGSs and the monthly availability achieved if all selected OGS were active. We observe that all the selected OGSs should be active only in 5 out of 12 months per year. Furthermore, 6 OGSs have to be active for 5 months and only 5 OGSs need to be active for 2 months. As a result, there are 1-2 redundant OGSs for 7 months a year.

Table 18: Active stations per month ($P_{avail}^{th} = 99.9\%$)

Month	# of active OGSs	Active OGSs	P_{avail}^{active} / P_{avail} (%)
Jan.	6	1,3,4,10,13,15	99.93 / 99.96
Feb.	7	1,3,4,7,10,13,15	99.93 / 99.93
Mar.	7	1,3,4,7,10,13,15	99.94 / 99.94
Apr.	6	1,3,4,7,10,13	99.91 / 99.96
May	7	1,3,4,7,10,13,15	99.92 / 99.92
Jun.	6	1,3,4,7,10,13	99.95 / 99.97
Jul.	6	1,3,4,7,10,13	99.93 / 99.96
Aug.	5	1,3,7,10,13	99.91 / 99.97
Sept.	5	1,3,7,10,13	99.92 / 99.98
Oct.	7	1,3,4,7,10,13,15	99.94 / 99.94
Nov.	7	1,3,4,7,10,13,15	99.95 / 99.95
Dec.	6	1,3,4,10,13,15	99.90 / 99.94

Finally, if we add two more OGSs of high altitude (16: Kit Peak, 17: Calama) to the initial set of 15 OGSs, the selected OGSs for $P_{avail}^{th} = 99.9\%$ are {1,2,16,17} and {17,16,1,2} using ESA and CHA, respectively. Both the proposed algorithms select the same subset of OGSs. The number of active OGSs per month are (4,4,3,3,3,4,3,3,3,3,3), so there is 1 redundant OGS for 9 months a year.

As exhibited in [Stubenrauch13], cloud coverage statistics exhibit yearly variability. Therefore for the resulting 7 OGSs, the joint CFLOS availability is computed for each month for each one of the 11 years used for the analysis and the minimum and maximum (among the 11 years) per-month availabilities are reported: minimum:{99.73, 99.84, 99.88, 99.77, 99.82, 99.88, 99.92, 99.95, 99.96, 99.83, 99.96, 99.87}% and maximum lies around 99.99% for each month. Thus, to accommodate both the yearly and monthly variability and guarantee a minimum availability threshold per month per year, the whole methodology can be employed for each year separately and then the OGSN for the worst case scenario is selected.

7   ATMOSPHERIC TURBULENCE MODELING AND VALIDATION WITH EXPERIMENTAL MEASUREMENTS

As described in Section 2.3 even under cloud free line of sight conditions propagation through the Earth's atmosphere still degrades the performance of the optical satellite communication system. The laser beam is attenuated due to atmospheric absorption and scattering, cirrus clouds and atmospheric turbulence. Among these impairments, atmospheric turbulence constitutes the main prohibitive phenomenon for optical satellite communications under CFLOS conditions. In this thesis the effects of turbulence regarding only GEO satellite are investigated.

In downlink propagation (from satellite to OGS), where turbulence mainly causes the signal-scintillation effects, aperture averaging technique is performed for the mitigation of this impairment. As explained in Section 2.3.5.1, for the quantification of the aperture averaging effect, aperture averaging factor (A) is really important. So far in literature, a variety of expressions for the estimation of aperture averaging factor is presented [Andrews05], [Hemmati09], [Kaushal17] and [Yura83]. In these expressions finite receiving apertures clear of central obscuration are assumed. However, large apertures have significant central obscuration. In the NASA's report edited by Fried [Fried75] firstly the aperture averaging factor for an obscured aperture is defined and a methodology is reported, where remarkable differences between a central obscured and a clear of obscuration aperture can be pinpointed, as far as the aperture averaging factor is concerned. In this Chapter a modified methodology for the estimation of aperture averaging factor for a central obscured aperture is presented and is validated with actual measurements from the ARTEMIS optical satellite measurement campaign [Romba04].

In uplink propagation atmospheric turbulence causes the scintillation effects and the so called beam effects, like the beam spreading and beam wandering [Andrews05] [Hemmati09], [Kaushal17]. Additionally, miss-pointing errors degrade the optical satellite uplink performance. For the reliable design of an optical uplink GEO satellite communication system, the accurate prediction of atmospheric turbulence effects is required. Therefore, methodologies for the estimation of uplink received power, taking into account the phenomena that degrade the optical signal and mainly the atmospheric turbulence effects based on actual measurements are needed. In this Chapter, a unified methodology for the generation of received irradiance/power time series for an optical uplink GEO satellite feeder link is presented. The proposed methodology takes into account the turbulence and miss-pointing effects among others, while it benefits of the use of Stochastic Differential Equations (SDEs), driven by fractional Brownian motion for the incorporation of the scintillation effects. The methodology is validated with actual measurements from the ARTEMIS optical satellite measurement campaign [Romba04].

Furthermore, it must be noted that for the estimation of turbulence effects on uplink the atmospheric parameters causing turbulence on the whole slant path should be estimated. The accurate estimation of these

parameters is required to reliably design a laser beam propagation system. A methodology for estimating the atmospheric conditions using downlink irradiance measurements is presented. Again experimental measurements from the ARTEMIS optical link campaign are used.

The remainder of the Chapter is structured as follows: In Section 7.1 a quick review of ARTEMIS optical satellite measurement campaign is reported. Measurements from this campaign are employed for the validation of the proposed methodologies. In Section 7.2 the methodology for the estimation of aperture averaging factor for central obscured aperture, in accordance with validation results is presented. In Section 7.3 the methodology for the generation of received irradiance/power time series is presented and validated; in addition, some numerical results using the proposed synthesizer are exhibited.

7.1 Recap of ARTEMIS Experimental Campaign

In this Section a review of the ARTEMIS bi-directional optical satellite link campaign will be presented.

7.1.1 ARTEMIS Campaign General Information

The European Space Agency (ESA) has launched the geostationary data-relay satellite ARTEMIS (GEO satellite), with one of its payloads being a laser communication terminal (LCT) (OPALE terminal) in 2001. Since April 2003 bidirectional links between ARTEMIS and the ESA Optical Ground Station in Tenerife have been established, for the study and characterization of laser beam propagation through the atmospheric turbulence [Alonso04], [Romba04]. From this campaign there are measurements employing the ESA's 1m telescope as receiver (downlink) and transmitter (uplink).

The ESA's OGS is located at the Observatorio del Teide at Izaña, Tenerife, Spain, at an altitude of 2393m over the sea. This site fulfills all the requirements for the establishment of optical satellite communication links like high altitude, low humidity, low occurrence of clouds and dust episodes and the strength of turbulence is low. The OGS is equipped with 1m telescope with 4 incoherent beams and the necessary instrumentation to establish a bi-directional optical data link with satellites. The main technical information is presented below, as taken from [Romba04]:

Table 19: ESA's OGS Technical Details

Location and geometrical details	
Longitude:	16.5101° West
Latitude	28.2995° North
Altitude	2.393 km
Telescope (Receiver)	
Entrance pupil diameter:	1016 mm
Central Obscuration/ Central Bore	330mm/215mm
LCT Transmitter	
Laser power out of aperture	300mW (maximum)
Laser beam diameter $(1/e^2)$	40 mm – 300 mm, four incoherent beams
Communication wavelength	847 nm

The main technical information of ARTEMIS GEO satellite is presented below, as taken from [Romba04]:

Table 20: Artemis GEO Satellite Technical Details (OPALE terminal)

Location and geometrical details	
Longitude:	21.5° East
Latitude	21.5 North
Altitude	35787 km
Telescope (Receiver)	
Entrance pupil diameter:	250mm
LCT Transmitter	
Laser power out of aperture	10mW (avarage)
Laser beam diameter $(1/e^2)$	125mm one beam
Communication wavelength	819 nm

Additionally, the Japanese Aerospace Exploration Agency (JAXA) developed the LUCE optical terminal and set it up at ESA's OGS in Tenerife, where bi-directional sessions from September 8 to 16, 2003 were established, between the LUCE terminal and the ARTEMIS satellite. LUCE acts as transmitter and receiver. LUCE terminal can transmit only one beam. Technical information about the LUCE terminal is reported bellow as derived from [Toyoshima05]:

Table 21: LUCE Terminal Technical Details

Telescope (Receiver)	
Entrance pupil diameter:	260mm
LCT Transmitter	
Laser power out of aperture	10mW (average)
Laser beam diameter ($1/e^2$)	120mm one beam
Communication wavelength	847 nm

7.1.2   ARTEMIS Campaign DATA Investigation (ESA's Terminal)

The raw data from the ARTEMIS campaign was provided by ESA and Dr. Zoran Sodnik under the ONSET project. The main amount of the data was since 2003 while there were also some scarce sessions during 2001 which could not be used because tracking was overexposed. Each session lasts about 20 minutes, while no more than 4 sessions are recorded during a single day. In accordance with the raw data, technical notes [ANEX-ARTEMIS] with detailed information about each session were delivered.

To begin with, a quick review of the technical notes since important information are derived is reported. In ANNEX A of [ANEX-ARTEMIS] for each session there are separate figures depicting the uplink and downlink irradiance time series in nW/m^2. For both uplink and downlink were two kinds of figures, the first ones depicting the whole session and the second ones the first 100 seconds, where the acquisition of the link took place. Under the figures there are tables where useful metrics and statistics for each session have been computed, like the variance and the mean value of the intensity and the logarithm of the intensity, the scintillation index, the range of the raw data and the probability of fades and surges in accordance with some valuable comments.

At this point, the main steps of the link acquisition procedure are briefly reported below, so as better insight of data is acquired.

- Beacon signal is turned on for 27 seconds. Beacon signal is received from antenna with 1m aperture and so there is a great averaging. The recording starts when OGS sees the light from the satellite.

- The Communication link is turned on at 27 sec.

- For 2 secs communication link and beacon are turned on together.

- At 30 secs beacon signal is turned off.

To continue, in ANNEX B of [ANEX-ARTEMIS] summary tables for each session are reported. In these tables detailed information about the input parameters and the phases of the experiment are stored. More specifically, the date and time of each session is recorded. In addition, each change which took place is reported and the time of this change is also recorded in the table. For the uplink case, the OGS laser terminal

can transmit up to 4 beams. As a result there are recording stages of the experiments where either 4, or 3 or 2 or 1 beams are transmitted. The transmission process starts always with 4 beams and ends with 1. The number of beams which is transmitted is recorded in table. Moreover the diameter of each beam transmitted from the OGS and the total power are recorded. It is considered that each transmission aperture has the same diameter as the beam diameter. Power can change during the session and of course each change is recorded. Furthermore, comments are also included, where among others there are flags for the presence of thin clouds and dust. When these flags are 1 the effects of clouds and dust must be taken into account in the analysis.

Moving to the raw data, they are stored either in txt or dat (ASCII) or TSA files for both the OGS (downlink) and the OPALE terminal (uplink). Loading the raw data the first two line provide information about the date.

- DATE=[year-month-day]
- UTC=[hour: minute: second milliseconds]

The second line describes the contents of the data lines:

- F=[data sampling frequency in Hz]
- X=[conversion factor into x-tracking error in μrads]
- Y=[conversion factor into y-tracking error in μrads]
- E=[conversion factor into irradiance in nW/m^2]

X and Y correspond to the tracking error, which is the residual error seen by the tracking sensor. The tracking sensor is part of a high speed tracking loop with a computer and a tip/tilt mirror.

Finally, the records of the x tracking, y tracking and Irradiance are multiplied by their factors and the measurements are acquired. Only the Irradiance measurements can be used.

For the uplink data there is an offset value due to tracking mechanism on OPALE, which has to be subtracted numerically (Interaction with ESA - Dr. Zoran Sodnik). Therefore, for each session the lowest measured uplink value is subtracted from the whole session in order that the results are not being biased. In Fig. 38, a plot of the uplink irradiance time series after subtracting the lowest value of the session is exhibited. From this figure the four phases of the transmission (4beams, 3beams, 2beams, 1beam) can be easily identified.
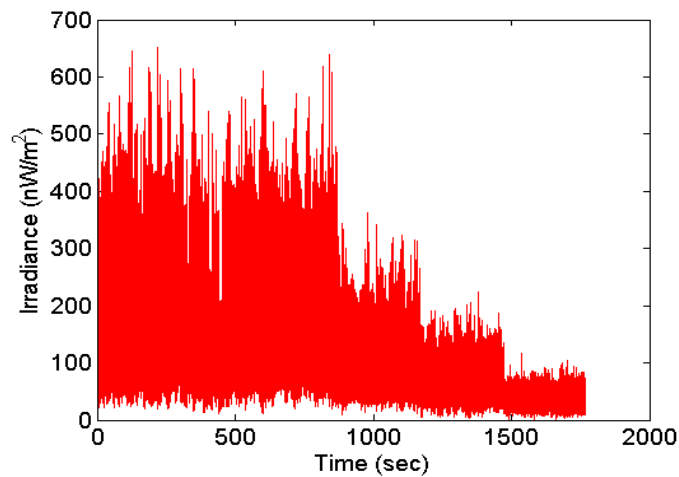
Fig. 38: Uplink time series after subtracting the offset value-Raw data ARTEMIS Campaign

Now an example of the downlink measurements is reported. In Fig. 39 a plot of the downlink irradiance raw data after the multiplication is exhibited.
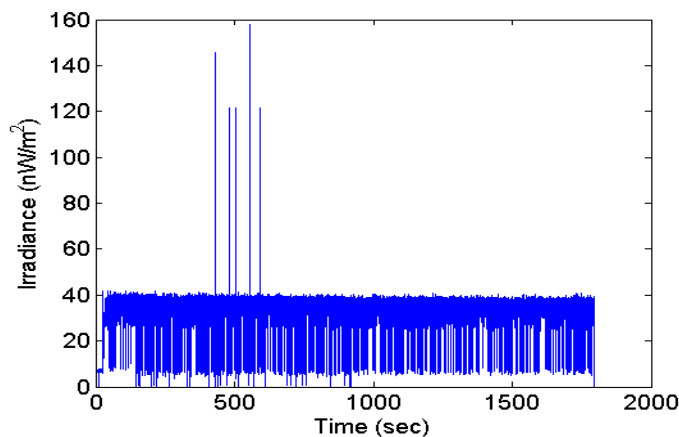
Fig. 39: Time series of irradiance for a downlink session-Raw data ARTEMIS Campaign

It can be easily pinpointed that there are some artificial peaks and scary instances in the data, which have to be discarded so as our results are not biased. These instances are coming from a noise problem of the tracking CCD camera in the OGS (Interaction with ESA - Dr. Zoran Sodnik). In order to discard these instances median filtering is employed. In Fig 40 a plot of time series of downlink session, after the process of removing these artificial peaks, is presented.

116
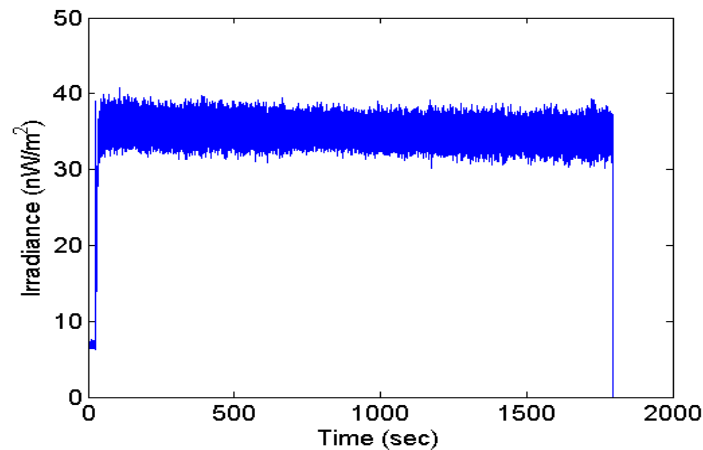
Fig. 40: Time series of irradiance for a downlink session after filtering-Raw data ARTEMIS Campaign

7.1.3   ARTEMIS Campaign DATA Investigation (LUCE Terminal)

In accordance with data presented in previous sub section, data from the bi-directional link with ARTEMIS and the LUCE terminal during September 2003 has also been provided. LUCE terminal transmits only one beam. The data are loaded with the same procedure as in previous subsection. For the downlink there are available measurements with both the ESA's OGS terminal and the LUCE terminal. The acquisition of the link between LUCE and OPALE in most of sessions is assisted by the ESA's OGS. Therefore, for the uplink transmission only the part that the LUCE terminal transmits alone (i.e. after the establishment of the link when the ESA's OGS transmitter is closed or if there was no assist of ESA's transmitter) can be used. Such information is stored in ANNEX B of [ANEX-ARTEMIS].

In Fig. 41   irradiance time series of downlink (LUCE) and uplink (OPALE) using the LUCE terminal as transmitter and receiver from the ARTEMIS campaign are exhibited.

117
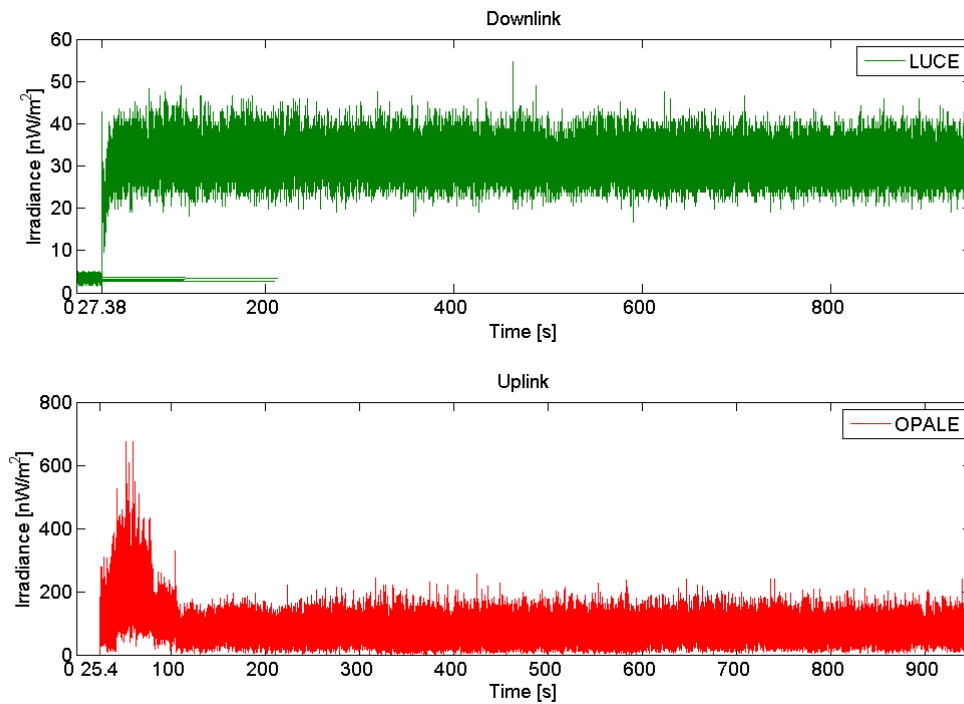
Fig. 41: Irradiance time series using LUCE terminal as transmitter and receiver- ARTEMIS Campaign

It can be commented here that when there are available downlink measurements from both LUCE and ESA's OGS terminals, the variance of the measurements of LUCE is higher because the antenna of LUCE is smaller than the one of the ESA's OGS and as a consequence the aperture averaging effect is also smaller. In Fig.42 the downlink measurements, acquired from LUCE and ESA's OGS terminal for a session on 09/09/2003 at 23:30, are exhibited.
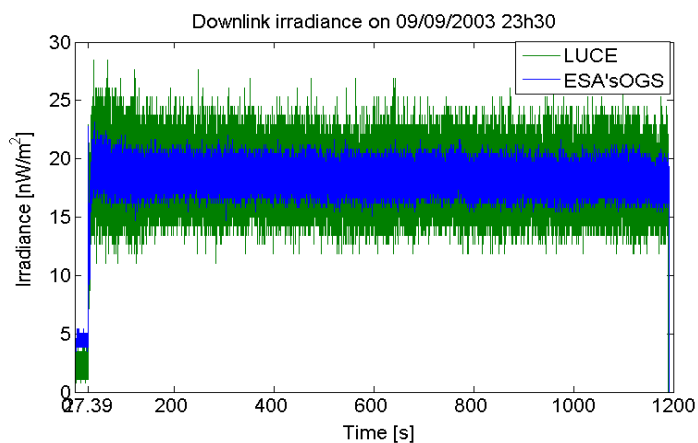
Fig. 42: Downlink time series (LUCE, ESA's OGS) – 09/09/2003 23:30-ARTEMIS Campaign

118

7.1.4 ARTEMIS DATA Cleaning

In this subsection, some important information about the use of the experimental data are reported. The part of measurements that should not be used are defined (Interaction with ESA -Dr. Zoran Sodnik).

The following information must be taken into account for every session:

- For the establishment of the link there is the point ahead angle (PAA) scanning. The PAA scanning takes place in the beginning of each session, but also it can be performed any time during the session if it was necessary. The PAA scan phases are reported in ANNEX B tables of [ANEX-ARTEMIS] and the time PAA scan starts and ends is noted. The measurements that correspond to the PAA scan phase must be removed from the analysis, in order not to bias the results.

- For downlink measurements, when there are bias points they must be removed, in order that the analysis is not biased. If there are bias points, they are reported in ANNEX A of [ANEX-ARTEMIS] under each table.

- The OPALE data session parts in which the measured irradiance reaches values close to or higher than 900 nW/m^2 shall be excluded, since these values come due to the overexposure of the tracking mechanism. Such an example is exhibited in Fig. 43.
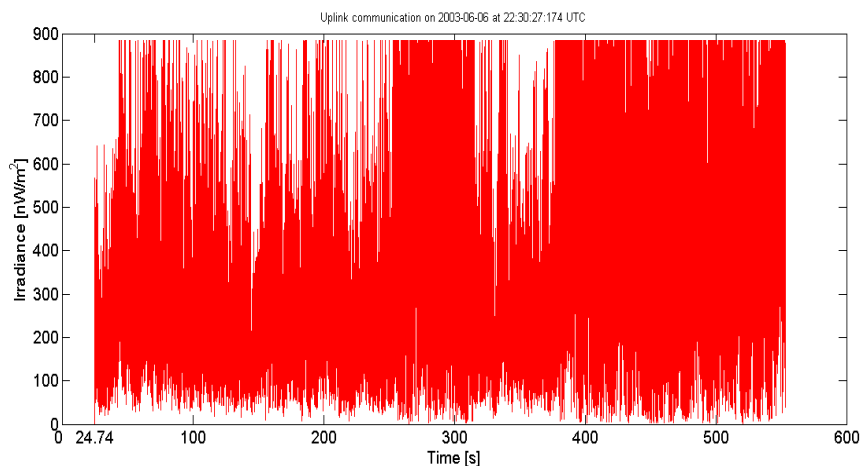
Fig. 43: Overexposed OPALE data-ARTEMIS campaign

Now some additional information for the analysis of the data is reported after the interaction with ESA-Dr Zoran Sodnik:

- The power recorded in the Table in Annex B of [ANEX-ARTEMIS] is the power out of the laser not the aperture, meaning that the optical losses and efficiencies are not included. In addition, this power is the total transmitted power, i.e. the sum of the power of the beams
- When there is no received irradiance for 2 secs, the recording stops.

7.1.5 Cleaning Process Summary

For the use of the data the following steps must be followed:

- Load Uplink and Downlink data.

- Transform the Irradiance records in nW/m^2 according to the recorded factors.

- Cleaning the downlink data from noisy spikes.

- Clean the uplink data in order that the results are not biased.

- Remove the bias points.

- Remove the overexposed sessions.

- Discard the first 100sec so as the bi-directional link is established and the Point Ahead Angle (PAA) scan part in order the results are not biased.

- Keep the part of the data is required.

7.2 Aperture Averaging Factor-Central Obscuration

In this sub section, a methodology for the estimation of aperture averaging factor for a central obscured telescope is presented. The proposed methodology is based on the analysis reported in NASA's report [Fried75] edited by Fried.

To begin with, it is assumed that the fluctuations of the averaged signal are not due to variation in the total optical signal power reaching the aperture, but rather are due to redistribution of the energy from one point in the aperture to another. That means that for an un-obscured circular aperture with diameter D, the variations of the averaged received signal are associated with the random relocation of energy between inside and outside of the circle. The variance of the received signal $\sigma^2{}_s(D)$ for an un-obscured aperture with diameter D can be written as:

$$\sigma^2{}_s(D) = \sigma_I^2(D) \cdot \langle S \rangle^2 \tag{67}$$

where $\sigma_I^2(D)$ is the scintillation index of an aperture with diameter D, $\langle S \rangle$ is the average received signal given as $\langle S \rangle = \dfrac{\pi}{4} D^2 I_0$, where I_0 is the mean intensity. Now using the expression (20) the variance of received signal is given as follows:

$$\sigma^2{}_s(D) = \sigma^2{}_I(0) \cdot A(D) \cdot \left(\frac{1}{4} \pi D^2 \right)^2 I^2{}_0 \tag{68}$$

where $\sigma_I^2(D)$ is the scintillation index (SI) for an aperture with diameter equal to D and $\sigma_I^2(0)$ is the SI for a point receiver.

Now, assuming a circular obscured aperture with diameter D and with central circular obscuration d, it can be assumed that the aperture is randomly exchanging optical power with its external surroundings with

an exchange variance equal to $\sigma^2_s(D)$, as given by the clear aperture formula for diameter D, and is randomly exchanging optical power with the internal "surroundings" (i.e. the obstruction region), with an exchange variance $\sigma^2_s(d)$, as given by the clear aperture formula for diameter d.

Therefore, the variance of the total received signal taking into account the obscuration is formulated as:

$$\sigma^2_{s,obscured} = \sigma^2_s(D) + \sigma^2_s(d) \tag{69}$$

Using expressions (69) and (68):

$$\sigma^2_{s,obscured} = \sigma^2_{I,point} \cdot A(D) \cdot \left(\frac{1}{4}\pi D^2\right)^2 I^2_0 + \sigma^2_{I,point} \cdot A(d) \cdot \left(\frac{1}{4}\pi d^2\right)^2 I^2_0$$

$$\sigma^2_{s,obscured} = \sigma^2_{I,point} I^2_0 \left(A(D) \cdot \left(\frac{1}{4}\pi D^2\right)^2 + A(d) \cdot \left(\frac{1}{4}\pi d^2\right)^2 \right) \tag{70}$$

Now according to (67) $\sigma^2_{I,obscured}$ assuming that average value of the received signal for an obscured aperture is $\langle S_{obscured} \rangle = \frac{\pi}{4} I_0 (D^2 - d^2)$ the SI for obscured telescope is:

$$\sigma^2_{I,obscured} = \sigma^2_{I,point} \cdot \left(\frac{D^4 \cdot A(D) + d^4 \cdot A(d)}{\left(D^2 - d^2\right)^2} \right) \tag{71}$$

Thus, aperture averaging factor is:

$$A_{obscured} = \left(\frac{D^4 \cdot A(D) + d^4 \cdot A(d)}{\left(D^2 - d^2\right)^2} \right) \tag{72}$$

while $\sigma^2_{I,point}$ can be estimated using the expression (15) and aperture averaging factors for D and d, respectively, are computed using expression (21).

7.2.1 Aperture Averaging Factor-Central Obscuration-Validation

The proposed methodology, for the estimation of obscured aperture averaging factor, will be tested with experimental results from the ARTEMIS campaign. Downlink data using as receiver the 1.016m central obscured (0.33m central obscuration) telescope of ESA is used.

The main steps of the validation procedure for each session used are summarized below:

- The SI from the experimental data $\sigma^2_{I,DATA}$ is computed.

121

- The SI for a point receiver $\sigma^2_{I,po\mathrm{int}}$ is estimated using the expression (15) and expression (10) for the $C_n{}^2(h)$.

- For $C_n{}^2(h)$ inputs:

- The RMS wind speed is estimated applying the Bufton methodology, using as input the wind speed on ground derived from concurrent meteorological data which are available.

- For A_0 a value close to 10^{-15} (m$^{-2/3}$) has be chosen for sessions taken place after 20:00 pm.

- Aperture Averaging factor is estimated from the experimental data $A_{DATA} = \dfrac{\sigma^2_{I,DATA}}{\sigma^2_{I,po\mathrm{int}}}$.

Aperture Averaging factor is computed assuming no obscuration using expression (21) and with the proposed methodology reported in previous section taking into account the central obscuration.

In Table 22, in the sixth column the aperture averaging factor from the experimental data (A_{DATA}) is estimated, while in the seventh column the aperture averaging factor is estimated assuming no obscuration ($A_{no-obsc}$), using expression (21) and assuming obscuration (A_{obsc}), using expression (72).

Table 22: Experimental Validation- Aperture Averaging Factor-Central Obscuration

DATE	Minutes	SI (DATA)	RMS Wind Speed (m/s)	SI (Point)	A_{DATA}	$A_{no-obsc} \mid A_{obsc}$
21/7/2003	21:20-21:25	0.00165	24	0.214	0.0078	0.0051/0.0073
22/7/2003	21:20-21:25	0.0013	19.8	0.152	0.0085	0.005/0.0072
22/7/2003	21:25-21:30	0.00133	20.2	0.158	0.0084	0.005/0.0072
24/7/2003	00:35-00:40	0.00151	21.9	0.182	0.0082	0.005/0.0072
24/7/2003	00:40-00:45	0.00154	22.4	0.189	0.0081	0.005/0.0072
24/7/2003	21:21-21:26	0.00125	21.8	0.18	0.007	0.005/0.0072
24/7/2003	21:26-21:31	0.0013	22	0.183	0.0071	0.005/0.0072
9/9/2003	21:17-21:22	0.002	22.2	0.186	0.01	0.005/0.0072
9/9/2003	21:22-21:27	0.00165	22	0.183	0.009	0.005/0.0072
9/9/2003	23:42-23:47	0.00155	21.7	0.179	0.0087	0.005/0.0072
10/9/2003	20:23-20:28	0.00216	26.8	0.262	0.0082	0.0051/0.0074

The average aperture averaging factor computed from the experimental data is close to 0.0083, while the average aperture averaging factor estimated using the un obscured expression is close to 0.005. The average aperture averaging factor estimated using the proposed methodology taking into account the central

obscuration, is close to 0.0072. It can be easily observed that the experimental results seem to fit better with the proposed methodology.

Here it must be noted that for the derivation of point scintillation index, the ground measurement of wind speed was used as input in Bufton model in order to obtain RMS wind speed and use it as input to the calculation of structure constant of refractive index. Therefore, the accuracy of the validation method can be further improved, employing concurrent measurements of vertical atmospheric profiles of humidity, pressure, temperature and wind speed and direction, in order to have a better estimation of C_n^2 on slant path. In addition, concurrent measurements of Fried parameters, measured by the respective instrumentation, can benefit such a validation process.

7.3   Received Irradiance/Power Time Series for Optical Uplink GEO Satellite Feeder Links

In this Section the proposed methodology for the generation of the received power/irradiance time series for an uplink GEO slant path are reported. Firstly the main assumptions of the proposed methodology are summarized:

- Uplink Transmission (The receiver is seen as a point).
- Ground to GEO satellite links.
- Rytov theory is assumed and the Kolmogorov spectrum of refractive index is used.
- Links with elevation angle greater than 20deg are assumed.
- Weak fluctuations are considered.
- One collimated Gaussian beam is considered.
- Adaptive optics are not considered.

For a satellite at distance SL(m) from the transmitter and in the general case that the received irradiance on the satellite aperture (which is seen as a point) is at a radial distance r from the beam center, the received irradiance $I_R(W/m^2)$ time series are given according to formula (73).

$$I_R(t) = n_T n_R n_{Atm} I(r, SL, t) \tag{73}$$

where n_T, n_R are the transmitter and receiver efficiencies, respectively. In receiver efficiency, the quantum efficiency of the detector is also included. n_{Atm} denotes the atmospheric losses incorporating the transmittance of the atmosphere depending on the wavelength (see Section 2.1.1) (Free space losses are not included in this factor) and the cirrus clouds transmittance (see Section 2.2.1). Cirrus transmittance is usually taken into account as a power margin in link budget analysis [Degnan93]. In I (W/m^2) the transmitter gain, the free space losses and the turbulence effects are incorporated (see Section 8 of [Hemmati09]). In case that there were no pointing errors, no turbulence effects and the tracking was perfect, the satellite would receive

the irradiance at the beam center, i.e. *r=0*. Since the receiver is seen as a point the received power P_R (W) is expressed as follows:

$$P_R(t) = I_R(t) \cdot \pi \cdot \frac{D_r^{\,2}}{4} \tag{74}$$

$D_r(m)$ is the diameter of the receiver aperture.

Now, inthe irradiance term $I(W/m^2)$ all the beam effects, the transmitter/receiver gains, the free space losses, turbulence etc. are incorporated.

To begin with, firstly *I* is expressed in case of free of turbulence propagation for collimated Gaussian beams [Andrews05], with no dependence on time but only on the propagation distance S*L (m)* (slant path) and the radial distance from the beam center *r,* at which the satellite receiver is finally illuminated:

$$I(r, SL) = \frac{2P_T}{\pi W(SL)^2} \exp\left(\frac{-2r^2}{W^2(SL)}\right) \tag{75}$$

P_T (W) is the total transmitted beam power, and *W(SL)* is the beam waist in meters after a propagation distance S*L*, given by the expression:

$$W^2(SL) = W_0^{\,2}\left[1 + \left(\frac{\lambda \cdot SL}{\pi \cdot W_0^{\,2}}\right)^2\right] \tag{76}$$

where W_0 (m) is the beam radius at the transmitter and λ is the wavelength in meters. For the incorporation of turbulence effects, the structure constant of refractive index $C_n^2(h)$ along the slant path is needed. In the proposed analysis the modified expression of Hufnagel-Valley (H-V) model reported in Section 2.3 expression (10) which depends on the altitude above the sea level (*h*) and takes into account the altitude of the ground station and the elevation angle among others, is employed. It must be noted that the turbulence is negligible above the troposphere layer. Thus, it is assumed that for altitude higher than 20km (turbulence max height H_{Turb}=20000m) $C_n^2(h > H_{Turb}) = 0$ [Andrews05] and [Hemmati09]. The expression (10) is reported again here for better clarity:

$$
\begin{aligned}
C_n^2(h) &= A_0 \exp(-H_{GS}/700)\exp(-(h-H_{GS})/100) + &&h \le H_{Turb} \\
&+ 5.94 \times 10^{-53} \times \left(\frac{w_{rms}}{27}\right)^2 h^{10} \exp(-h/1000) + \\
&+ 2.7 \times 10^{-16} \exp(-h/1500)
\end{aligned}
\tag{77}
$$

$$C_n^2(h) = 0 \qquad\qquad\qquad h > H_{Turb}$$

where w_{rms} is the RMS value of wind speed in m/s, h the height above mean sea level in meters and $A_0(m^{-2/3})$ is the nominal value of $C_n^2(h)$ at ground level. According to Bufton model [Andrews05] w_{rms} is given by:

$$w_{rms} = \frac{1}{15x10^3}\left[\int_{5\times10^3}^{20\times10^3} V^2(h)dh\right]^{\frac{1}{2}}$$

(78)

with

$$V(h) = \omega_s h + V_g + 30\exp\left[-\left(\frac{h-9400}{4800}\right)^2\right]$$

(79)

where ω_s is the slew rate of the satellite in rad/sec and V_g the wind speed at ground level in m/sec.

For uplink propagation turbulence causes the scintillation and the beam wander of the signal [Andrews05], [Hemmati09]. Assuming the Rytov theory and the Kolmogorov spectrum [Andrews05], expression (75) is modified in order the turbulence effects are incorporated:

$$I(r,SL) = \frac{2P_T}{\pi W_{LT}(SL)^2}\exp\left(\frac{-\beta^2}{W_{ST}^2(SL)}\right)\exp(2\chi_n)$$

(80)

where W_{LT} (m) is the effective beam spot size considering scintillation effects and it is computed using the Strehl ratio [Andrews05]:

$$W_{LT}(SL) = W(SL)[1+(2\sqrt{2}W_0/r_0)^{5/3}]^{3/5}$$

(81)

where $W(SL)$ is given according to expression (76) and r_0 (m) is the Fried parameter computed for uplink propagation according to the next expression [Andrews05]:

$$r_0 = \left[0.42\sec(\zeta)k^2\int_{H_{GS}}^{H_{Turb}} C_n^2(h)dh\right]^{-3/5}$$

(82)

where ζ is the zenith angle and k the wavenumber. The larger values of Fried parameter mean less severe turbulence effects.

In case of weak turbulence scintillation index is less than unity (SI<1). In the proposed approach SI is computed for fully tracked beams according to the expression proposed in [Andrews05] (expression (16) of this Thesis). For weak turbulence, log amplitude variance is given according to the formula $\sigma_\chi^2 = \frac{1}{4}\ln(\sigma_I^2+1)$.

The effect of scintillation is taken into account through the term $\exp(2\chi_n)$, where χ_n is the normalized log-amplitude [Andrews05]. Assuming weak fluctuations for the time series generation of χ_n a

zero mean-unity variance, low pass Gaussian process is assumed. Such processes can be modeled according to [Shao95] using Stochastic Differential Equations (SDEs) driven by fractional Brownian motion (fBm). This approach takes advantage of the use of SDEs and permits the definition of dynamic characteristics of the process. The underlined Gaussian process will be generated through:

$$d\chi_{t,1} = -\lambda_s \chi_{t,1} dt + \sigma dB_H \tag{83}$$

where dB_H is the increment of the fBm with Hurst index H. Since for a given variance χ_t can be considered as a Gaussian process with zero mean value, we use the Langevin equation with fBm (fractional Langevin equation) to model the time series of log-amplitude, giving that the variance is equal to 1 ($\chi_{t,1}$) with the following solution [Kourogiorgas13], [Shao95]:

$$\chi_{t,1} = e^{-\lambda_s t} \sigma \int_0^t e^{\lambda_s u} dB_u^H \tag{84}$$

The parameters λ_s and σ depend on the dynamic parameters of the stochastic process and its long-term statistics, more information can be found in [Kourogiorgas13] and in Appendix. Finally, time series for log- amplitude are computed through the expression:

$$\chi_n = \sigma_\chi \chi_{t,1} \tag{85}$$

β in equation (80) is the instantaneous value of beam wander where the effect of beam wander and other effects like the point errors and errors due to vibrations are included. β is a Rayleigh distributed variable parameter:

$$\sigma_\beta = \frac{\sqrt{\langle r_c^2 \rangle}}{H_{Turb} / \cos(\zeta)} + \sigma_{others} \tag{86}$$

where $\langle r_c^2 \rangle$ is given according to expression (18). W_{ST} (m) is the spot size due to the small scale spread (also called beam breathing) [Andrews05]:

$$W_{ST}^2 = W_{LT}^2 - \langle r_c^2 \rangle \tag{87}$$

In σ_{others} the standard deviation of pointing errors etc. are incorporated.

7.3.1   Turbulence Conditions Estimation

Before we continue to the validation results a methodology developed for the estimation of the atmospheric turbulence parameters using the downlink irradiance measurements, is reported.

Turbulence is of prominent importance for uplink laser beam propagation consequently, the atmospheric parameters causing turbulence on the whole uplink slant path should be estimated.

Since both uplink and downlink concurrent measurements from ARTEMIS campaign were available and in the downlink propagation scintillation contains the only source of variation, the parameters of $C_n^2(h)$ i.e. the RMS value of wind speed in m/s and the $A_0 (m^{-2/3})$ can be estimated using the downlink. This methodology will be used for the estimation of the $C_n^2(h)$ parameters from the downlink and then used as input in the received irradiance/power uplink synthesizer reported in Section 7.3.

The main steps of the methodology are summarized as follows:

- SI from the downlink measurements is computed $\sigma_{I,DATA}^2 = \dfrac{\langle I_{data}^2 \rangle - \langle I_{data} \rangle^2}{\langle I_{data} \rangle^2}$, where I_{data} is the downlink received irradiance and $\langle\rangle$ denotes the mean value.

- In the irradiance measurements the aperture averaging effect is incorporated.

- As described in Sections 2.3.5.1 and 7.2 the SI taking into account the aperture averaging effect, is expressed as $\sigma_{I,theory}^2 = A(D) \cdot \sigma_{I,point}^2$. $A(D)$ is the aperture averaging factor mainly dependent on the receiver's aperture diameter. $\sigma_{I,point}^2$ is the SI for a point receiver dependent on $C_n^2(h)$. Therefore $\sigma_{I,theor}^2$ depends on A_0 and w_{rms} .

- $C_n^2(h)$ parameters and consequently atmospheric conditions can be estimated from downlink data, minimizing the following expression:

$$\left(\left| \frac{\sigma_{I,theor}^2(A_0, w_{rms}) - \sigma_{I,DATA}^2}{\sigma_{I,DATA}^2} \right| \right) \tag{88}$$

7.3.2 Received Irradiance/Power Time Series Uplink Synthesiser Validation Results

In this section, the proposed methodology is validated with the experimental data from ARTEMIS campaign, in terms of first order statistics of the normalized uplink intensity. For the validation process measurements during both day and night (after 20:00) will be used, while results using both ESA's terminal and LUCE terminal will be reported.

For ESA's terminal it must be noted that it can transmit from one up to 4 beams. The proposed methodology will be tested only with the part of measurements with one beam transmission. Additionally, in the majority of the sessions the transmitted laser beam diameter is 40mm and detailed information about the ESA's terminal can be found in Table 19.

LUCE terminal transmits only one beam with 120mm diameter. In the majority of the sessions that LUCE terminal transmits, the phase of the initial acquisition and the establishment of the link is assisted by the ESA's terminal. Consequently, only the part of the measurements that LUCE terminal transmits alone will be used.

To begin with, for the validation process the definition of $C_n^2(h)$ (expression (77)) parameters is needed. For A_0 two different values are defined, one for sessions during night and another for sessions during day. For sessions during night, A_0 is set equal to $10^{-15}(m^{-2/3})$, while for sessions during day it is set equal to $3.5*10^{-13}$ $(m^{-2/3})$. For the estimation of the RMS wind speed the downlink irradiance measurements are used for each session separately, according to the methodology reported in Section 7.3.1. Additionally, analyzing the experimental data two different values for the pointing/vibration errors standard deviation, depending on the terminal which transmits, are utilized. The following values are assumed and inserted in model for σ_{others}: $1.3*10^{-6}$ for ESA's terminal and $1.8*10^{-7}$ for LUCE terminal.

For each session the performance of proposed channel model is tested with the experimental data. Two kinds of comparisons are employed:

a.   The SI of uplink experimental data is compared with the SI of time series produced by proposed methodology according to the inputs defined before.

b.   The Probability Density Function (PDF) of the synthesized normalized time series are compared with the normalized PDF of the experimental data.

It has been found that the proposed model reproduces the first order order statistics with an RMS error below 1% for all cases tested. In particular, we are presenting two sessions using as transmitter the ESA's terminal once during day and once during night (after 20:00) and once using LUCE terminal during night.

The first session used for validation was on 24/05/2003 17:00 (DAY) where ESA's Terminal transmits.

Table 23: Irradiance-Validation Inputs 24/5/2003 17:00

DATE	One Beam Transmission Duration	Beam Diameter (mm)	RMS Wind Speed (m/s)	A_0 $(m^{-2/3})$	r_0 (m)
24/5/2003 17:00	17:27–17:30 (3 min)	40	27	$3.5*10^{-13}$	0.098

The experimental PDF vs. the synthesized PDF is given in Fig. 44. The SI computed from the time series estimated from the proposed methodology is 0.328, which is very close to the one computed from the experimental data, which is 0.331.
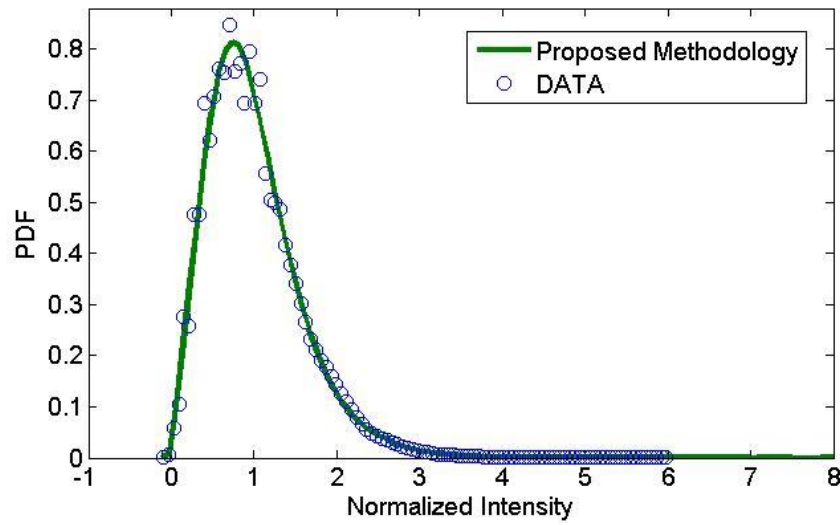
Fig. 44: Normalized Received Irradiance for Session on 24/05/2003 17:00 Experimental PDF vs Synthesized PDF

The second session used, is the one on 23/07/2003 24:15 (NIGHT) where ESA's terminal transmits.

Table 24: Irradiance-Validation Inputs 24/7/2003 00:15

DATE	One Beam Transmission Duration	Beam Diameter (mm)	RMS Wind Speed (m/s)	A_0 ($m^{-2/3}$)	r_0 (m)
24/07/2003 00:15	00:40 – 00:45 (5 min)	40	22.3	$1*10^{-15}$	0.4

The experimental PDF vs. the synthesized PDF is given in Fig. 45. The SI computed from the time series produced by the proposed methodology is 0.126, which is almost the same with the one computed from the experimental data, which is 0.122.
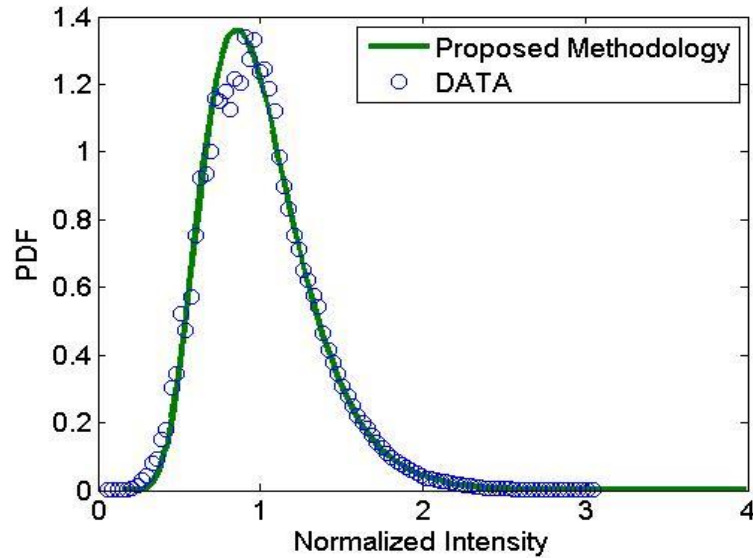
Fig. 45: Normalized Received Irradiance for Session on 24/07/2003 00:15 Experimental PDF vs Synthesized PDF

Moving on to a session where LUCE terminal transmits, the session on 16/09/2003 20:10 (NIGHT) is used.

Table 25: Irradiance-Validation Inputs 16/9/2003 20:10

DATE	One Beam Transmission Duration	Beam Diameter (mm)	RMS Wind Speed (m/s)	A_0 ($m^{-2/3}$)	r_0 (m)
16/09/2003 20:10	17:24–20:30 (6 min)	120	17	$1*10^{-15}$	0.45

The experimental PDF vs. the synthesized PDF is given in Fig. 46. The SI computed from the time series produced by the proposed methodology is 0.13, which is almost the same with the one computed from the experimental data, which is 0.127.

130
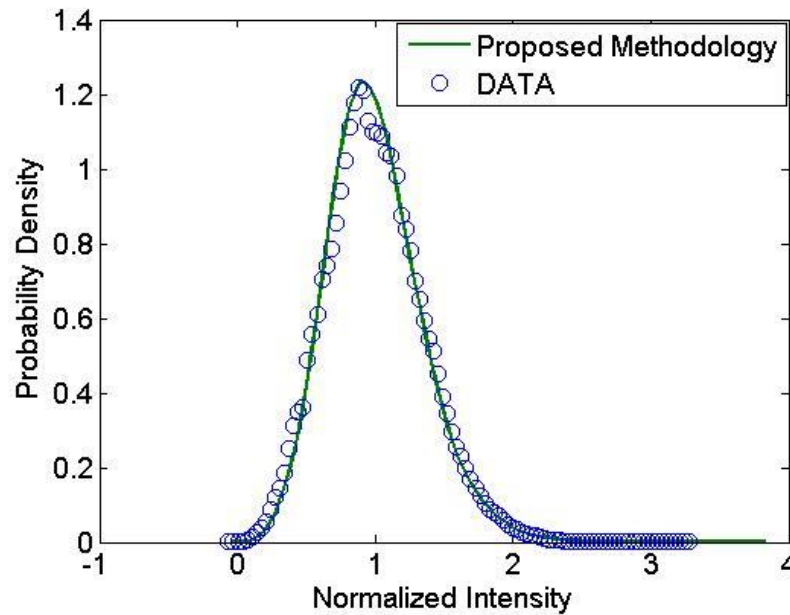
Fig. 46: Normalized Received Irradiance for Session on 16/09/2003 20:10 Experimental PDF vs Synthesized PDF

From Fig. 44-Fig. 46, it can be observed that the proposed synthesizer reproduces the first order statistics of the uplink received irradiance with very good accuracy during both day and night conditions.

7.3.3 Uplink Received Irradiance Numerical Results

The proposed methodology is employed for the generation of received power first order statistics in terms of Cumulative Distribution Function (CDF), for various atmospheric turbulence conditions. These curves are very important for the design of optical feeder links and show the sensitivity of the channel model to various inputs. The different atmospheric conditions are captured on different r_0 values. We consider the OGS in Tenerife and the ARTEMIS satellite. Since the methodology is general, for the simulated results different transmission parameters compared with ARTEMIS campaign are used. The transmitted power is 10W, the beam diameter is 80mm, the wavelength is 976nm, the pointing error/vibration standard deviation is $1.3*10^{-6}$, the transmitter's efficiency is 0.7, the receiver's efficiency is 0.28 (0.4 detector quantum efficiency is included), the atmospheric transmittance is considered 0.88 and the receiver's diameter is 0.25m. In Fig. 47 the CDF for $r_0 = 0.44$m, $r_0 = 0.3$m, $r_0 = 0:197$m and $r_0 = 0.116$m are presented. The corresponding scintillation indexes computed are 0.2627, 0.316, 0.4 and 0.5 respectively. Worst atmospheric turbulence conditions, as expected, lead to smaller received power values.
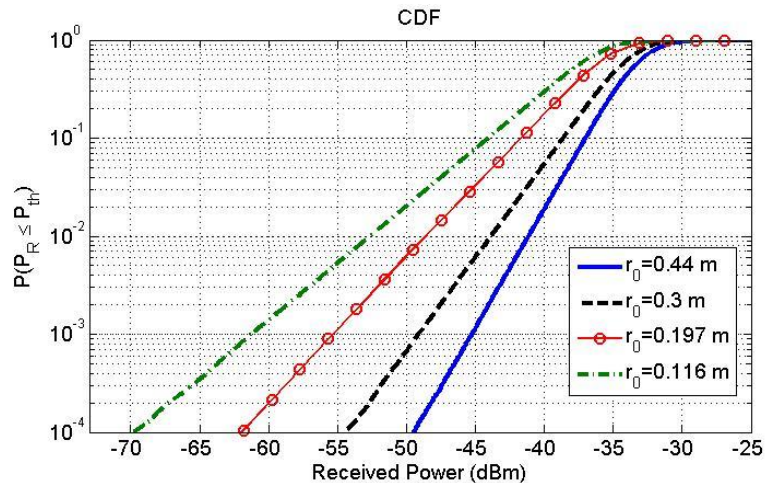
Fig. 47: Received Power CDFs for various atmospheric turbulence conditions

Now, the proposed synthesizer is employed for the generation of received power statistics for different beam diameters, the same atmospheric conditions and r_0=0.48m (Fig. 48). It is assumed that the transmitted power is 10W, the wavelength is 847nm (different from previous scenario), the pointing error/vibration standard deviation is $1.3*10^{-6}$, the transmitter's efficiency is 0.7, the receiver's efficiency is 0.28 (0.4 detector quantum efficiency is included), the atmospheric transmittance is considered 0.88 and the receiver's diameter is 0.25m. The transmitted beam diameters ($2W_0$) that are tested are 40mm, 120mm, 200mm and 400mm, respectively.
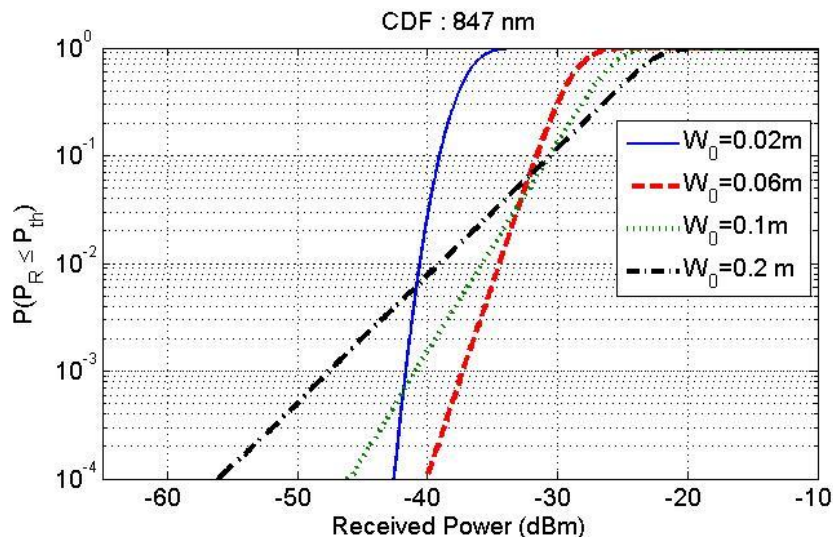
Fig. 48: Received Power CDFs for various beam radius

It can be observed that when the beam radius takes values close to Fried parameter, the received power is decreased, due to turbulence effects [Andrews06].

132

ACKNOWLEDGMENT

8   DEEP SPACE OPTICAL LINK DESIGN

This chapter is devoted in the design of a deep space optical link. Deep Space Communication links are considered for distances greater than Moon. For deep space optical communications, the space agencies in CCSDS (Consultative Committee for Space Data Systems) recently concluded on a standard for High Photon Efficiency (HPE). The standard comprises a specification on the coding and synchronization layer [CCSDS17b] and one on the physical layer [CCSDSc].

After specifying the standard, space agencies are now focused on planning In Orbit Demonstrations (IOD), although the waveform of [CCSDS17b] was already demonstrated to a large extent in the frame of the Lunar Laser Communication Demonstration [Boroson09]. From the European Space Agency (ESA) point of view, a Deep-space Optical Communication System IOD is proposed for the Space Safety Program, Space Weather mission to the Sun-Earth Lagrange point L5 [Sodnik17].

In order to assess the requirements and the performance of deep space optical links, an accurate link budget analysis must be firstly conducted. The main scope of this analysis is the estimation of signal and noise photon rates, in order that the maximum data rate depending on the link characteristics is achieved.

Therefore, in this chapter the elements required for the design of the optical deep space link are defined and an algorithm for the estimation of the maximum capacity and data rate of the link depending on the signal and noise photon rates is reported. Apart from performing a sensitivity analysis of various hypothetical deep space missions, the chapter presents a practical methodology that allows the link designer to select the main signaling parameters (modulation order, code rate, slot width), without resorting to lengthy coded Bit Error Rate (BER) evaluations that otherwise need to be run for a large parameter set. This allows faster link budget calculations e.g. for performing trade-off studies.

The main elements that must be taken into account in a deep space link budget analysis are summarized in Fig. 49.
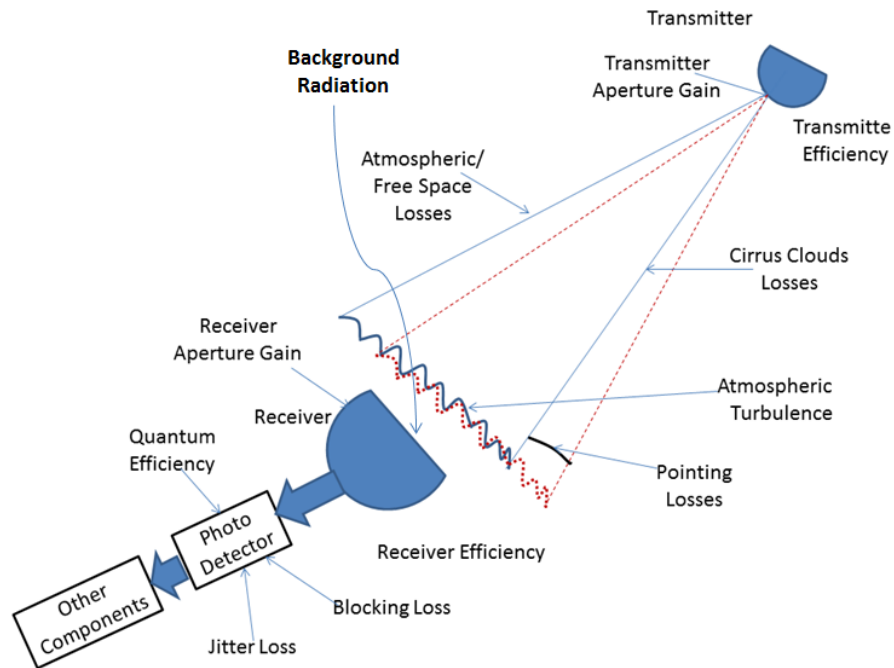
Fig. 49: Configuration of Deep Space-Link Budget Design elements

In the remainder of the chapter each element is presented. Some of the impairments have already been analyzed in this Thesis (mainly the propagation impairments), however for better clarity some information and expression are recalled.

The main assumptions of the deep space link are reported. To begin with, an optical downlink operating under cloud free line of sight conditions, between an optical terminal on board a deep space spacecraft and an optical ground station is assumed. As generally in deep space channel modeling a Poisson channel is assumed and intensity modulation (IM) and direct detection (DD) are considered [CCSDS17b]. Regarding the signaling, the Pulse Position Modulation (PPM) [ITU1742] and a Serially Concatenated-Pulsed Position Modulation (SC-PPM) [Moision05] are assumed. For the incorporation of noise contribution, single photon counting detectors are considered [Caplan07]. For competence, some information about other kind of detectors like the avalanche photodiode detectors (APD) and the PIN diode detectors, are presented [Caplan07].

It must be noted that this analysis is conducted under an ESA project for the future deep space missions and it is based on the new CCSDS High Photon Efficiency standards [CCSDS17b].

8.1 Deep Space Link Budget Analysis

8.1.1 Signaling-Optical Modulation and Coding

For the deep space scenario intensity modulation and direct detection method is considered. Optical direct detection effectively measures the energy in the optical signal impinging on the detector and is capable of distinguishing only between different intensity levels that does not depend on the phase of the signal, thus intensity modulation is required. The principal digital intensity modulation form is used is the pulse-position modulation (PPM). In each time slot the laser is either "on" or "off".

In Pulse-position modulation (PPM), $\log_2 M$ bits are modulated by transmitting a single pulse in one of the M possible time slots of a symbol (Fig. 50). A part of the total symbol time is devoted for laser recharging and does not contain any pulse [ITU1742], [Biswas03]. One of the main advantages of PPM is that it can be implemented non-coherently, i.e. the receiver does not need to track the phase of the carrier signal. As a result, PPM is suitable for optical communications and especially for deep space communications [ITU1742], [Biswas03], [Hemmati06], where coherent phase modulation and detection are quite difficult and expensive. However, in PPM the receiver has to be properly synchronized to align the local clock with the beginning of each word, in order to achieve high throughput and low BER.
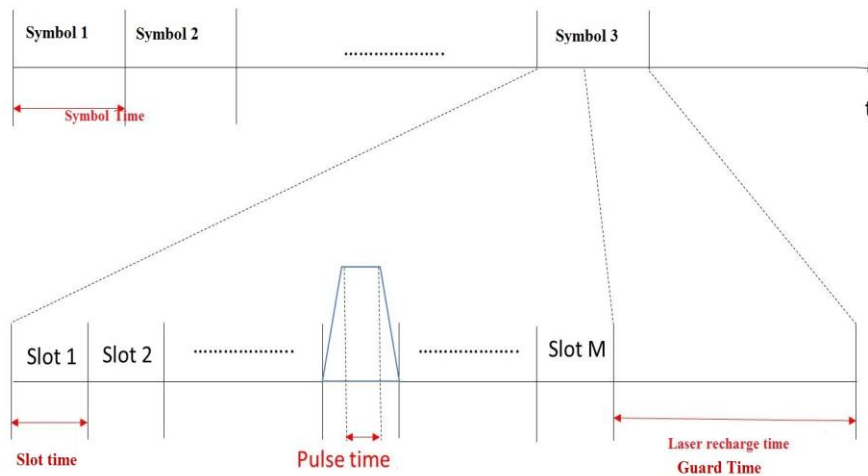
Fig. 50: M-PPM configuration

T_s (s) is the symbol duration, T_{slot} (s) is the slot duration and T_{LR} (s) is the laser recharge time duration or defined also as guard time. These durations are related as $T_s = M*T_{slot} + T_{LR}$. According to [CCSDS17b] the guard time is defined as $T_{LR} = M*T_{slot}/4$, meaning that the symbol duration is $T_s = 5*M*T_{slot}/4$.

For the reliable delivery of data Error Correction Codes (ECC) are employed. An ECC adds redundant information to the user bits to enable error correction at the receiving end and results in more

efficient use of power and bandwidth. An *(n, k)* binary ECC maps each *k* information bits to *n* coded bits, and introduces the rate of the code as $R_{ECC} = k/n$ [Hemmati06], [Hemmati09]. In return for this added redundancy, the ECC provides large gains over an uncoded system. In communication systems convolutional codes are commonly used. Convolutional codes are linear codes whose code words may be produced with (typically short) shift registers, allowing an efficient representation of the code words as paths on a trellis. In deep space communication serial concatenated convolutional codes (SCs) are employed. SCs typically include an inner code, an outer code, and probably a linking interleaver. A distinguishing feature of SCs is the use of a recursive convolutional code as the inner code. The recursive inner code provides the 'interleaver gain' for the SC, which is the source of the excellent performance of these codes. For Deep Space communications SCs are commonly used with PPM modulation (SC PPM). The code rates of 1/3, 1/2 and 2/3 are the most commonly used. A thorough analysis for SC PPM is reported in [Moision05]. In [Moision05] SC-PPM is introduced for deep space communications, while it is tested against other coding technique, proving that Deep Space Optical Systems are benefited using the SC-PPM.

Now, in every symbol with duration T_s , $R_{ECC} \log_2(M)$ bits are sent. In every symbol, *M* slots are used with total duration $M*T_{slot}$. Therefore, the data rate for an ECC codded PPM signal can be computed with the next formula:

$$R_b(bits/\mathrm{s}) = \frac{R_{ECC} \log_2(M)}{M \cdot T_{slot} + T_{LR}} \tag{89}$$

8.1.2 Deep Space Link Losses-Before the photo detector

In this subsection the received power on the aperture is given and the factors that impair the link are exhibited. In this stage only the losses which are not dependent on the detector are reported.

To begin with, the received power after the receiver telescope and before the photo detector $P_{r,ap}$ (W) can be computed as:

$$P_{r,ap} = P_t \cdot G_t \cdot G_r \cdot L_{fs} \cdot L_a \cdot L_c \cdot L_s \cdot L_{pt} \cdot \eta_t \cdot \eta_r \tag{90}$$

Where:

- P_t : transmitted power (W)

- G_t, G_r : transmitter/ ground-receiver aperture gains

- L_{fs} :free-space losses,

- L_α : atmospheric losses

- L_c : cirrus cloud losses

138

- L_s : scintillation loss

- L_{pt} : pointing losses

- η_t, η_r : transmitter/ receiver efficiencies

8.1.2.1 Free Space Loss

Free space loss of the optical signal is due to the physical separation distance between the transmitter and receiver, computed according to the formula [Hemmati06], [Hemmati09], [ITU1742], [Manning]:

$$L_{fs} = \left(\frac{\lambda}{4\pi R} \right)^2 \tag{91}$$

where R= distance, called as range, between transmitter and receiver (m).

8.1.2.2 Transmitter/Receiver Gains

To start with, the majority of telescopes used for optical satellite communications have central obscurations, such as the secondary mirror of the Cassegrain telescopes [Biswas10] [Degnan74], [Hemmati06], [Hemmati09], [ITU1742], [Klein74], [Manning], [Moision12]. This type of telescopes consists of two mirrors, a primary and a secondary. The primary mirror has grater diameter than the secondary one, while the secondary obscures the primary one.

The transmitter aperture gain G_t is calculated based on the assumptions that the transmitter has a laser source characterized as single mode Gaussian emission, the antenna gain patterns are measured in the far field and its aperture is circular [ITU1742], [Klein74]. Consequently, for a Gaussian profile laser amplitude beam projected through a circular, centrally obscured aperture, in the direction of optical axis (on-axis gain) assuming far-field and plane wave approximations, the transmitter aperture gain is given by [Moision12], [ITU1742]:

$$G_t = \left(\frac{\pi D_t}{\lambda} \right)^2 \frac{2}{a_t^2} \left(e^{-a_t^2} - e^{-a_t^2 \gamma_t^2} \right)^2 \tag{92}$$

where D_t : transmitter primary aperture diameter (m), a_t : aperture to beam-width ratio and

$$a_t = \frac{D_t}{2W_0}$$

W_0 is the $1/e^2$ width of transmitted beam (m) ($1/e^2$ point corresponds to the point at which the beam amplitude falls off to 13% of the amplitude on axis), γ_t : transmitter obscuration ratio, $\gamma_t = \dfrac{b_t}{D_t}$, and b_t : is the transmitter secondary aperture (obscuration) diameter (m).

In case of no obscuration i.e. a system without secondary mirrors (b_t=0, $\gamma_t = 0$) $a_t^{optimal} \approx 1.12$

In [Manning] transmitter gain is given according to the next expression (no obscuration is assumed for the transmitter). In our approach this expression is used in case of no obscuration:

$$G_t = \frac{8}{w_{0,rad}^2} \tag{93}$$

$W_{0,rad}$ (rad) is the $1/e^2$ half-width divergence angle of the beam:

$$w_{0,rad} = \sqrt{8}\,\frac{\lambda}{\pi D_T} \tag{94}$$

If Gaussian beams are used then $w_{0,rad} = \dfrac{2\lambda}{\pi D_T}$. In the case of receiver gain we assume that the signal source is sufficiently far away so that plane waves arrive on the receiver aperture [Degnan74]. Afterwards, the receiver gain is expressed as [Biswas03], [ITU1742], [Manning], [Moision12]:

$$G_r = \left(\frac{\pi D_r}{\lambda}\right)^2 \left(1 - \gamma_r^2\right) \tag{95}$$

where D_r : receiver's primary aperture diameter (m), b_r : receiver's secondary aperture diameter(m), λ: wavelength of incoming signal. γ_r : receiver's obscuration ratio, $\gamma_r = \dfrac{b_r}{D_r}$.

In case of no obscuration i.e. a system without secondary mirrors (b_r=0, $\gamma_r = 0$).

8.1.2.3   Atmospheric Losses

The atmospheric loss (transmittance) L_α includes the effects of atmosphere in the laser communication beams. Atmospheric losses explained in detail in Section 2.1.1. Additionally, if the atmospheric transmittance of the vertical link is known then the atmospheric transmittance depending on the elevation angle of the link can be expressed as [Hemmati09]:

$$L_a = L_{a,zenith}^{(1/\cos(\zeta))} \tag{96}$$

where ζ is the zenith angle of the link and $L_{a,zenith}$ is the atmospheric transmittance of the vertical link.

8.1.2.4   Cirrus Clouds Loss

For establishing the deep space link, cloud free line of sight (CFLOS) transmission is assumed. However, even when the sky appears relatively clear (no water clouds), sub-visible ice clouds i.e. cirrus clouds can be present along the slant path. Cirrus clouds loss can be estimated according to [Degnan74], however in deep space analysis cirrus clouds loss is taken into account as an extra power margin of some (0.5-4) dBs.

8.1.2.5   Scintillation Loss

The turbulence effects are discussed in detail in Section 2.3. In downlink deep space optical communications large apertures are assumed (more than 4meters). Therefore the aperture averaging effect is really large and as a consequence the scintillation effects are minimized. Scintillation loss is less than 0.1dB. Scintillation loss can be given for a specific probability level according to the next formula [Giggenbach15]:

$$L_s = \left(3.3 - 5.77\sqrt{\ln(1/p_o)}\right)\sigma_I^{4/5}(dB) \tag{97}$$

where p_o is a certain probability level. Scintillation index is computed taking into account the aperture averaging effect Section 2.3.

8.1.2.6   Pointing Efficiency

The necessity for narrow beam width subject to the long range of a deep-space link makes the accurate pointing acquisition critical. The inaccurate point acquisition of the laser beam renders the receiver to be located off-axis from the far-field irradiance profile, resulting in a pointing loss. Pointing errors cause time-varying fading in the received signal power.

Pointing error loss can be estimated for a specific probability level from the Probability Density Function (PDF) of normalized received intensity taking into account the pointing error according to [Hemmati09]:

$$p(I_{pp}) = \beta_p I_{pp}^{\beta_p - 1}, 0 \le I_{pp} \le 1$$

$$\bar{I}_{pp} = \frac{\beta_p}{\beta_p + 1} \tag{98}$$

$$\beta_p = \frac{w_{0,rad}^2}{4\sigma_p^2}$$

where σ_p is the variance of pointing errors . Thus, for this given PDF and a probability level of p_0, pointing Loss is computed according to the expression:

$$p_0 = \int_{-\infty}^{x} p(I_{pp}) dI_{pp} \Rightarrow$$
$$L_{pt} = p_0^{1/\beta_p}$$

(99)

In [Barron06] the effect of FEC codes and interleaving technique for the mitigation of pointing and tracking errors is exhibited.

8.1.2.7   Transmitter/Receiver efficiencies

The transmitter/receiver optical efficiencies that capture the losses due to coupling of the laser beam to the optical system and losses in propagation through the optical system at the transmitter/receiver, are modeled with the factors η_t, η_r respectively. The laser beam is coupled to optical elements like mirrors, single mode fibers and optical amplifiers based on single mode fibers.

In case of transmitter efficiency (electrical to optical), transmission and reflection losses are considered and especially scattering and polarization losses. The transmitter efficiencies have been reported on the order of 1.4 to 2.3 dB [Biswas03], [Manning], [Moisson12]. On the other hand, the receiver efficiency incorporates the transmission losses through a narrow band pass optical filter, primary and secondary mirror losses, transmission losses through polarizing optics truncation losses and, if present, coupling losses to a fiber. Finally, the receiver efficiencies have been reported on the order of 3 to 5 dB [Biswas03], [Manning], [Moisson12].

8.1.2.8   Power Link Margin

A common technique in deep space link budget analysis is the consideration of a power link margin of some dBs, for improved reliability. Since there are inherent uncertainties regarding the signal and noise power this additional loss (margin) is incorporated in order the designed system to be able to cope with these uncertainties. In this case the received power before the photon detector is given as:

$$P_{r,ap} = P_t \cdot G_t \cdot G_r \cdot L_{fs} \cdot L_a \cdot L_c \cdot L_s \cdot L_{pt} \cdot \eta_t \cdot \eta_r \cdot n_{link\_margin}$$

(100)

where n_{link_margin} is the extra loss included as factor(n_{link_margin}<=1).

8.1.3   Detector Dependent Losses - Signaling Dependent

Now the detected power i.e. after the photo detector $P_{r,\det}$ (W) is reported:

$$P_{r,\det} = P_{r,ap} \cdot \eta_{\det} \cdot n_{coding} \cdot L_b \cdot L_j \qquad (101)$$

where:

- $P_{r,ap}$: the received power before the photo detector

- $\eta_{\det}$: detector quantum efficiency

- n_{coding} : coding efficiency

- L_b : blocking loss

- L_j : jitter loss

As discussed in the introduction of this chapter, for deep space communications single photon counting detectors have been proposed. Photon counting detectors can be assumed as an ideal extension of APD detectors with infinite gain, in which a digital output signal is generated for each detected photon [Caplan07]. For this kind of detectors the blocking and jitter detector losses are introduced [Caplan07], [Moision12].

8.1.3.1   Blocking Detector Loss

Photon-counting photo-detectors become inoperative (blocked) for some time after detection event. This blocking leads to losses (blocking losses: L_b) relative to an ideal detector, which have to be measured (see Fig. 51). Photo detector blocking can be modeled as the extra power which is needed in contrast to the ideal one, to support the same communication rate.
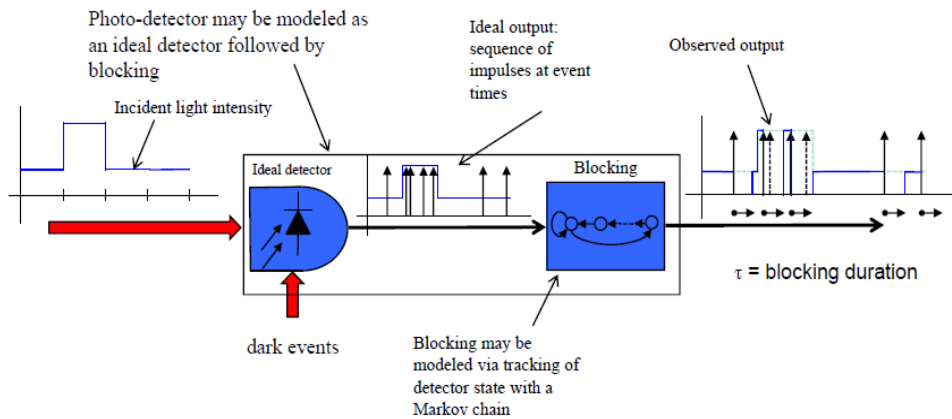
Fig. 51: Blocking Loss Explanation (source [Dolinar])

In [Moision11] the blocking loss for a single receiver is computed in terms of capacity loss, symbol error rate loss (SER) and count rate. In addition, in [Moision11], for single detectors the performance of the maximum likelihood (ML) receiver in blocking, as well as a maximum count (MC) receiver is reported. It is

143

important to pinpoint that blocking is a signal dependent loss. Two different cases are examined in literature, one for single detectors and another for arrays of detectors.

Based on the analysis presented in [Dolinar] and [Moision11] an approximation for blocking loss, termed as capacity loss, for a single detector is exhibited. Firstly, a Markov model for the detector state (blocked/ unblocked) with μ the probability that the detector is unblocked, is assumed. To this end, the signal power loss i.e. the increase in power to achieve a fixed capacity, is $sqrt(\mu)$. For the computation of μ the next expressions may be used:

$$\mu = \frac{1}{1 + \tau l}$$

(102)

$$l = l_n + l_s$$
$$l_s = P_{r,ap} \cdot n_{det} / E_{photon}$$
$$l_n = P_n / E_{photon}$$

where l_n, l_s is the noise and signal photon flux on the detector, respectively, T_{slot} is slot duration (s) and τ denotes the blocking duration (s). P_n is the noise power and E_{photon} is the energy per photon ($h*c/\lambda$), h is the Planck's constant, c is the speed of light and λ is the wavelength used.

For low SNR (deep space case) blocking loss equals to $sqrt(\mu)$, while for high SNR blocking loss equals to μ.

Blocking loss is computed in Fig. 52, for a hypothetical scenario with M=16, T_{slot}= 2ns $l_n=10^8$ photons/s and τ=1ns, τ=10ns, τ=20ns and τ=50ns (dead time) as a function of signal dB photons/sec is reported.
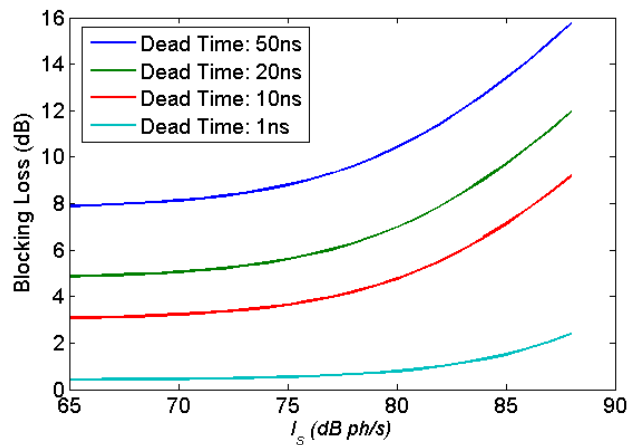
Fig. 52: Blocking Loss using the approximated method

It can be easily observed that when dead time is a lot longer than the slot duration, then blocking loss is extremely high. To this end, detector array technology can be employed to mitigate this loss among others

144

[Moision11], [Moision12]. The blocking loss for array of detectors is investigated in [Moision11], [Moision12]. For the computation of μ in array detector case, where $\tau > T_{slot}$, the following expression can be used:

$$\mu = \frac{1}{1 + \dfrac{\tau}{T_{slot}}\left(1 - \dfrac{M-1}{M}e^{-l_n \cdot T_{slot}/K_{array}} - \dfrac{1}{M}e^{-l_n \cdot T_{slot}/K_{array} - l_s \cdot T_{slot} \cdot M/K_{array}}\right)} \tag{103}$$

In this case blocking loss equals with μ while K_{array} is the size of the detector array. It is assumed that each detector of the array detects the same amount of signal and noise photon rates i.e. l_s/K_{array} and l_n/K_{array}, respectively. Now, the blocking loss is estimated in Fig. 53 for different array sizes $K_{array}=8, 32, 64, 128$. Slot duration is set 0.5ns, dead time is 50ns and noise photon rate per detector (l_n/K_{array}) is 8e4 ph/s.
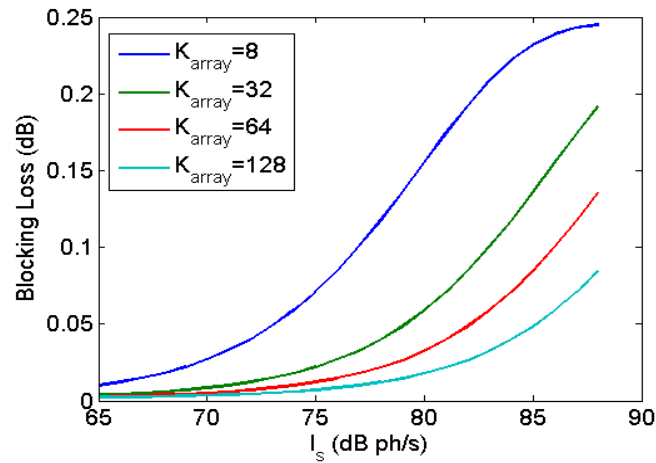
Fig. 53: Blocking Loss, detector array

8.1.3.2 Jitter Detector Loss

In photon counting detectors there will be a random delay, from the time a photon is incident on the detector to the time an electrical output pulse is produced, in response to that photon. This random delay, is called detector jitter and it produces losses (L_j) (see next subfigures in Fig. 54)
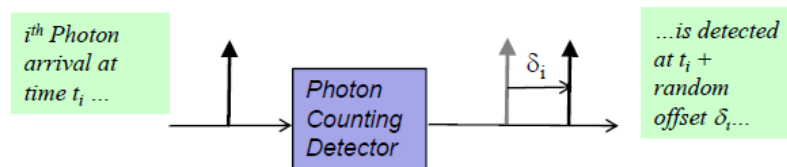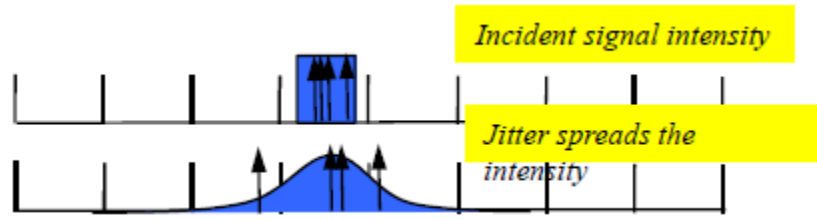
Fig. 54: Detector Jitter Explanation (source [Dolinar])

In [Moision08] analytical expressions for the computation of jitter loss and interesting plots of jitter detector loss, as a function of the normalized jitter variance (σ_j/T_{slot}), for different input parameters are reported. Now, the expression of the approximated method of [Moision08], which is reported in [Moision08] and [Moision12] for the computation of jitter detector loss, is reported bellow:

$$L_j = 10\log_{10}(5\Psi^2 + 2\Psi + 1)$$

(104)

$$\Psi = \frac{\sigma_j}{T_{slot}} \frac{\left(1 + \tanh(R_{ECC} - 1/2)\right)}{1.25^{\log_2(M)}}$$

L_j is jitter detector loss, σ_j is standard deviation of jitter (sec), M is the order of PPM modulation and R_{ECC} is the ECC rate. It is assumed that jitter is Gaussian distributed with standard deviation σ_j. In Fig. 55 Jitter detector loss as a function of Ψ is reported.
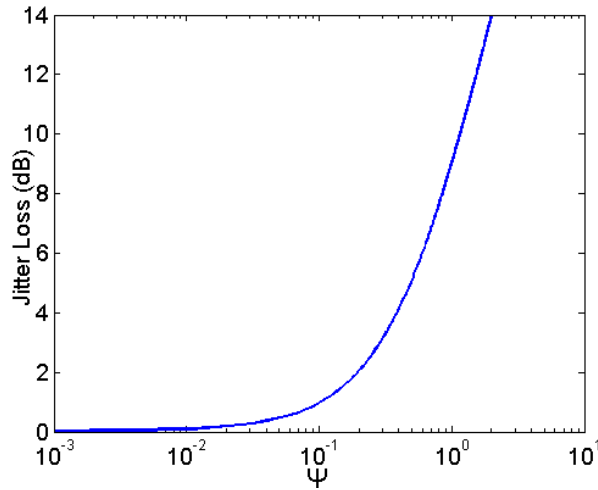
Fig. 55: Jitter detector loss

For moderate M and $\sigma_j/T_{slot} > 0.1$ jitter results in a significant loss. For $\sigma_j/T_{slot} > 1$ jitter results in high losses [Moision08], [Moision12].

146

8.1.3.3   Code Efficiency

As reported in [Moision12] implementation efficiency or losses are related to the receivers missed or false detections of photons from the noisy electrical output, errors in recovering the clock and other issues. These losses vary from 0.2 to 2, dBs depending on the complexity of the receiver and decoder implementation [Moision12].

In practice, codes (ECC) only approach the ideal performance. With the term ideal performance it is assumed the requirement that $C=R_b$, where C is the capacity and R_b is the data rate. To this end, code efficiency is the extra power is need to achieve the ideal performance for a specified bit error rate, on the order of 0.5-2 dBs. Examples of coding efficiencies according to the ECCs are used are reported in [Moision05] [Hemmati09]. For uncoded systems the 'code' efficiency is assumed as 5dB [Moision05].

8.1.4   Noise Contribution

The performance of deep space optical communication links and the link budget calculations are highly dependent on the contribution of noise. To this end, an accurate estimation of all the noise sources which are present in the deep space communication down link, is needed. In this paragraph the noise components that should be considered for the evaluation of the deep space optical link budget system, using intensity modulation (IM) and direct detection (DD) with single photon counting detectors. As discussed in the beginning of this Chapter, this is the kind of detector currently planned to be used for the deep space missions. Therefore this section is focused on the single photon counting detector. However, some information about the noise contribution for APD and PIN detectors will also be exhibited.

8.1.4.1   Noise Contribution on Photo Counting Detectors

As explained in the beginning of this Chapter the photon counting detectors can be assumed as an ideal extension of APD detectors with infinite gain in which, a digital output signal is generated for each detected photon. Due to the binary nature of the detection output, noise in the detection process appears in the form of dark counts or varying detection efficiency. In this case, as main noise sources, the background photons and the dark counts can be assumed [Caplan07]. Additionally, another noise source introduced in [Dolinar] is the leakage power from the transmitter. Total noise power is given as:

$$P_n = n_{\text{det}} P_b K_{array} + d^2_{\text{det}ector} \iota_d E_{photon} K_{array} + P_{leakage} \tag{105}$$

where $\iota_d \, (e/s/m^2)$ is the detector dark rate, $P_{leakage}$ (W) is the leakage power (W), P_b (W) is the background power, $d_{\text{det}ector}$ (m) is the diameter of each detector. If only one detector is assumed $K_{array}=1$.

Leakage Power is given as:

$$P_{leakage} = n_{leakage} \cdot P_{r,ap} \cdot n_{det} \tag{106}$$

where $n_{leakage}$ is the leakage ratio.

8.1.4.2 Background Power

The power of the background signal at the detector comes from diffuse energy from sky, and planets or stars which are in the field of view of the receiver [ITU1742], [Manning], [Moision12],[Biswas03], [Lambert96].

Background power P_b can be computed according to the next expression for radiant targets whose angular subtense is larger than the receiver field of view (diffuse energy from sky, planets and the stray light that scatters into the detector's field of view) [Biswas03], [Biswas10], [ITU1742], [Lambert96], [Manning], [Moision12]:

$$P_{b,sky} = H_{b,sky} \Omega_{fov} n_r A_r B_f$$
$$P_{b,planets,stray} = H_{b,planets,stray} \Omega_{fov} n_r A_r B_f \tag{107}$$

and when the background source can be represented as a point source (Stars) according to [ITU1742], [Manning], [Lambert96]:

$$P_{b,stars} = N_{b,stars} n_r A_r B_f \tag{108}$$

where n_r is the efficiency of the receiver, H_b (W/m²/Sr/μm), N_b (W/m²/μm) are the background radiance and irradiance energy densities of large angular sources and point sources respectively, which depend on the wavelength (atmospheric losses are included in these factors) [ITU1742], [Manning], [Moision12],[Biswas03], [Lambert96], B_f is the receiver band pass optical filter width (μm), Ω_{fov} is the field of view of the receiver's aperture (sr) and A_r is the receiver area (m²). Ω_{fov} (sr) can be derived from [ITU1742], [Lambert96], [Manning]:

$$\Omega_{fov} = 2\pi \left(1 - \cos\left(\frac{d_{det ector}}{2 * F_{Length}} \right) \right) \tag{109}$$

where $d_{det ector}$ (m) is the diameter of the detector and F_{Length} (m) is the focal length of the telescope.

Total background power is expressed as:

$$P_b = P_{b,sky} + P_{b,planets,stray} + P_{b,stars} \tag{110}$$

At this point it must be noted that several methodologies have been proposed and studied for the reduction of background noise, like the polarization rejection (if the signal is polarized i.e. circular

polarization a polarization filter can be employed in the receiver in order that the received background light is reduced [Hemmati11]), the spectral filtering, adaptive optics etc. [Hemmati11], [Ortiz00]. In this case total background power is expressed as

$$P_b = (P_{b,sky} + P_{b,planets,stray} + P_{b,stars}) \cdot n_{reduction} \qquad (111)$$

where $n_{reduction}$ is the background reduction factor.

The detected background power is:

$$P_{b,\det} = P_b \cdot n_{\det} \qquad (112)$$

8.1.4.3   Noise Contribution APD-PIN Detectors

In this paragraph the noise components that should be considered for the evaluation of the deep space optical link budget system, using intensity modulation (IM) and direct detection (DD) with either an APD or a PIN diode, are briefly presented. In a block diagram of a direct detection receiver, along with the main noise contributors exhibited for simplicity.
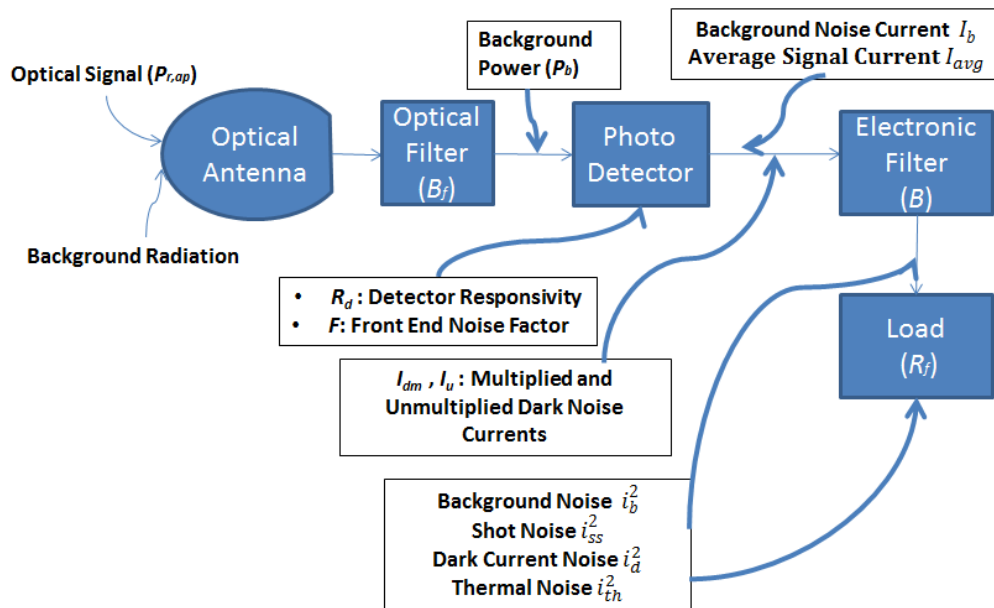
Fig. 56: Block Diagram of Direct Detection Receiver showing the noise contributions for APD-PIN detectors

In this case all the noise terms will be expressed in form of the square of noise current ($i_{n,generic}^2$) following the next generic form:

$$i^2_{n,generic} = 2q \cdot I_{n,generic} \cdot B \qquad (113)$$

where B is the bandwidth of the electrical filter (Hz), q is the quantum charge ($1.6*10^{-19}$ coulombs) , $I_{n,generic}$ is the average noise current computed according to the noise power ($P_{n,generic}$) and given as:

$$I_{n,generic} = P_{n,generic} \cdot R_d \qquad (114)$$

where R_d is the detector responsitivity.

The first noise source as in the case of the photon counting detectors is the background noise. Background noise can be computed with the same way as in Section 8.1.4.2. Then the background noise power can be expressed in terms of the square of noise current (A^2) as follows:

$$i^2_b = 2q \cdot F \cdot I_b \cdot B \qquad (115)$$

where F is the front end noise factor of the receiver computed for the different types of diodes [Lambert96], [Manning] and can be expressed as [Lambert96]:

$$F = M_a \cdot k_{eff} \cdot (1 - k_{eff}) \cdot (2 - 1 / M_a) \qquad (116)$$

where k_{eff} is the ionization coefficient of the photo detector and M_a is the avalanche gain of the detector. For case of PIN F=1.

where I_b is the average background current (A) computed according to the received background power (P_b) and given by:

$$I_b = P_b \cdot R_d \qquad (117)$$

The dominant noise source for the optical deep space communication systems is the signal self-generated noise called shot noise. This kind of noise is proportional to the whole received power that is incident on the photo detector. In [Lambert96], [Toyoshima07a] analytical expressions for the estimation of shot noise can be found. The shot noise in terms of square of noise current (A^2) is given by:

$$i^2_{ss} = 2q \cdot F \cdot I_{avg} \cdot B \qquad (118)$$

where I_{avg} is computed from the next expression while more information can be found in[Lambert96], [Toyoshima07a]:

$$I_{avg} = P_{r,ap} R_d \qquad (119)$$

150

The detector dark noise, also known as bulk detector noise power, concerns the amount of noise which is present when the detector is in dark. Dark noise depends on the operating temperature of the photo diode and its physical volume. As reported in [Lambert96], [Toyoshima07a] it can be distinguished into 2 different noise sources, the multiplied and the non-multiplied (surface leakage) dark current noise. For the case of PIN only the non-multiplied dark current noise is taken into account:

$$i_d^2 = 2q \cdot F \cdot I_{dm} \cdot B + 2q \cdot I_u \cdot B \tag{120}$$

where I_{dm} and I_u are the multiplied and unmultiplied dark noise currents computed according to [Lambert96], [Toyoshima07a].

The last major noise contributor is the thermal or Johnson noise. This kind of noise is dependent on the electric circuit of the receiver. Expressions for the estimation of this kind of noise can be found in [Lambert96], [Toyoshima07a]. Expression for thermal noise in terms of the square of noise current (A^2) is reported as:

$$i_{th}^2 = \frac{4k \cdot T \cdot B}{R_f \cdot M_a^2} \tag{121}$$

where k is the Boltzman's constant, T is the effective noise temperature of the feedback resistor (K) and R_f is the value of the feedback resistor (Ω).

Finally, the total noise is the sum of all squares of noise currents and is given as:

$$N_0 B = i_{ss}^2 + i_d^2 + i_b^2 + i_{th}^2 \tag{122}$$

The direct detection SNR for APD and PIN detectors is computed according to the formula [Lambert96]:

$$SNR = \frac{\langle i_s \rangle^2}{N_0 B} = \frac{\left(P_{r,ap} \cdot R_d\right)^2}{N_0 B} \tag{123}$$

8.2 Estimation of Capacity, Symbol Error Rate and Bit Error Rate

In this section firstly the expression for the estimation of the capacity under the assumption of a Poisson PPM channel will be reported. Capacity as defined in [Hemmati06] can be divided into two categories, depending on the type of information provided to the decoder by the receiver. In one case the receiver makes estimates of each PPM symbol, passing these estimates, or hard decisions, on to the decoder. In this case, the (hard-decision) capacity may be expressed as a function of the probability of symbol error. In the second case, the receiver makes no explicit symbol decision, but passes on slot counts (integrals of the

received signal in each slot), or soft decisions, directly to the decoder. In this case the (soft-decision) capacity may be expressed as a function of the channel statistics [Hemmati06]. The soft-decision capacity is at least as large as the hard decision capacity, because the slot counts provide additional information to the decoder.

According to the methodology described in [Moision12], [Moision14] the channel capacity can be given in closed form for the case of nonzero noise (our case), according to the next expression for soft decision capacity:

$$C = \frac{1}{\ln 2 \cdot E_{photon}} \left(\frac{P^2_{r,det}}{P_{r,det} \cdot 1/\ln(M) + P_{b\_det} \cdot \frac{2}{M-1} + P^2_{r,det} \cdot \frac{M \cdot T_{slot}}{\ln(M) \cdot E_{photon}}} \right) \quad (124)$$

where C is the capacity in bits/sec, M is the order of PPM modulation, P_{b_det} is the detected background noise power (W), $P_{r,det}$ (W) is the detected power and T_{slot} (sec) is the slot duration.

For hard decision, capacity can be given according to the formula [Hemmati06]:

$$C_{bits/channel} = \log_2(M) + (1 - SER)\log_2(1 - SER) + SER \cdot \log_2\left(\frac{SER}{M-1}\right) \quad (125)$$

where SER is the probability of symbol error. $C_{bits/channel}$ is expressed as the capacity in bits per channel use and according to [Hemmati06] capacity C, in bits per second is computed as $C_{bits/channel}/(MT_{slot})$, neglecting the guard time, or $C_{bits/channel}/(MT_{slot} + T_{LR})$, incorporating the dead time.

Now, the expression for the computation of Bit Error Rate (BER) for uncoded Poisson PPM channel for single photon counting detector and Symbol Error Rate (SER) for the same kind of detectors will be expressed.

The SER for a single photo counting detector is given as [Hemmati06]

$$SER = \sum_{k=0}^{N}\left(1 + \frac{K_s}{K_n}\right)^k \frac{e^{-K_s}}{M}\left(\frac{M \cdot K^k_n e^{-K_n}}{k!} - F_{Y|X}(k|0)^M + F_{Y|X}(k-1|0)^M\right) +$$
$$+ \sum_{k=N+1}^{\infty} \frac{(K_s + K_n)^k}{k!} e^{-(K_s+K_n)}(M-1)\sum_{m=k}^{\infty}\frac{K^k_n e^{-K_n}}{k!} + +O\left(\frac{K^k_n e^{-K_n}}{k!} + \left(\sum_{m=k}^{\infty}\frac{K^k_n e^{-K_n}}{k!}\right)^2\right) \quad (126)$$

K_s are the number of signal photons per symbol duration K_n are the noise photons per slot (see next Section) and $F_{Y|X}(k|0)$ is given according to the formula:

$$F_{Y|X}(k \mid 0) = \sum_{m=0}^{k} K_n^m e^{-K_n} / m! \tag{127}$$

Finally, the uncoded Bit Error Rate is estimated according to the expression:

$$BER = \frac{M}{2(M-1)} SER \tag{128}$$

8.2.1 Estimation of Capacity, Symbol Error Rate and Bit Error Rate for APD detectors

In this section, just for the competence of the chapter the formulas for the estimation of capacity, uncoded BER and SER for APD detectors are exhibited.

Firstly, Hard Capacity and BER can computed with the same formulas as in previous sections, but by using the expression for SER for the APD/PIN detectors. For APD/PIN detectors assuming a Gaussian approximation the uncoded SER is given according to the formula [Meera98]:

$$SER = \frac{M-1}{2} erfc \left(\frac{q \cdot M_a \cdot K_s}{\sqrt{2\left(q^2 \cdot M_a^2 \cdot F_{SER} \cdot (2K_b + K_s) + 2q \cdot T_{slot} \cdot I_{dm} + \frac{4k \cdot T \cdot T_{slot}}{R_f}\right)}} \right) \tag{129}$$

$$F_{SER} = k_{eff} \cdot M_a + (2 - 1/M_a) \cdot (1 - k_{eff})$$

8.3 Units Conversion

In this section the formulas for the conversion of power in photons/slot, photon/bit, photons/sec will be reported.

To begin with according to [Alexander97] [Manning] average power can be transformed in photons per second for a specific wavelength employing the expression:

$$K(photons/\sec) = \frac{P(W)}{E_{photon}} \tag{130}$$

For the computation of photons per slot:

$$K(photons \, / \, slot) = \frac{P(W) \cdot T_{slot}}{E_{photon}} \tag{131}$$

For the computation of photons per symbol:

$$K(photons \, / \, symbol) = \frac{P(W) \cdot (MT_{slot} + T_{LR})}{E_{photon}} \tag{132}$$

Now for the calculation of photons per bit from bits/sec, let's say for capacity C (bits/sec) the next formula is used [Alexander97] [Manning]:

$$C(photons \, / \, bit) = \frac{P(W)}{E_{photon} \cdot C(bits \, / \, \sec)} \tag{133}$$

8.4   Determination of PPM order Slot width coding rate

In this Section a methodology for the determination of the most suitable combination of PPM order, ECC rate and slot width depending on the received signal and noise power (single photon counting detector) is presented, in order that the maximum capacity and data rate is achieved.

It is assumed a Serially Concatenated-Pulsed Position Modulation (SC-PPM) with managed parameters as in the CCSDS High Photon Efficiency standard [CCSDS17b] with PPM Order M, allowed values 4, 8, 16, 32, 64, 128, 256, with code rate allowed values 1/3, ½, 2/3 and with slot widths allowed values 0.125ns, 0.25ns 0.5ns, 1ns, 2ns, 4ns, 8ns and 512ns.

The main steps of the methodology are:

- Firstly, we consider all the available combinations of coding rates R_{ECC} , PPM order M, T_{slot} , $(R^i_{ECC}, M^j, T^k_{slot})$. We compute the data rate of an ECC coded PPM signal (but without taking into account the guard slot duration):

$$R^{i,j,k}_{\;b} = \frac{R^i_{ECC} \log_2(M^j)}{M^j \cdot T^k_{slot}} \tag{134}$$

- All the combinations are sorted beginning from the one with the resulting higher data rate.
- The received power before the photo detector is computed according to the procedure described in Section 8.1.2.
- The total detected noise power is estimated according to the procedure described in Section 8.1.4.1.
- For all $\left(R^i_{ECC}, M^j, T^k_{slot}\right)$ combinations assuming the received noise/signal power computed above the blocking /jitter/coding losses (as factors $\left(L^{i,j,k}_{blocking}, L^{i,j,k}_{jitter}, n^{i,j,k}_{coding}\right)$) are

154

computed respectively (see Section 8.1.3). In this analysis it is assumed that the coding efficiency is the same for all code rates (so n_{coding} takes the same value for all combinations).

- For all $\left(R^i_{ECC}, M^j, T^k_{slot} \right)$ combinations the detected power is defined as

$$P^{i,j,k}_{r,\det} = P_{r,ap} \cdot L^{i,j,k}_{jitter} \cdot L^{i,j,k}_{blocking} \cdot n^{i,j,k}_{coding} \cdot n_{\det} \qquad (135)$$

- Now assuming the noise power computed in step 3, for each $P^{i,j,k}_{r,\det}$ the soft capacity is computed $C^{i,j,k}(P^{i,j,k}_{r,\det})$ (see Section 8.2).

- The combination of $\left(R^i_{ECC}, M^j, T^k_{slot} \right)$ with the highest data rate is selected given that

$$C^{i,j,k}(P^{i,j,k}_{r,\det}) > R^{i,j,k}_b \qquad (136)$$

Next, assuming the selected combination of $\left(R_{ECC}, M, T_{slot} \right)$ all the required metrics like data rate, detected power, uncoded BER, uncoded SER, hard capacity, soft capacity etc. are computed according to the formulas presented in this chapter so far.

With this approach we keep all the non-signalling dependent losses while the signalling/detector dependent (blocking/jitter/coding) losses are taken into account so as the most appropriate pair of PPM ECC is used, depending on the channel conditions. The chart of the methodology is exhibited in Fig. 57.
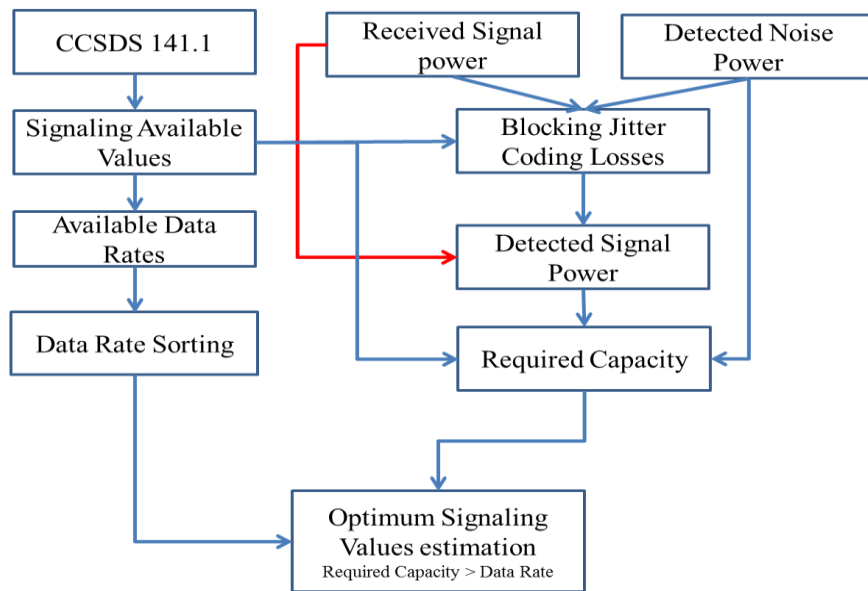
Fig. 57: Signalling Values Estimation

8.5 Capacity vs Distance - single photon counting detector

In this section the capacity is expressed as a function of distance R, i.e. the analogy between capacity and range R is investigated. A single photon counting detector is assumed.

To begin with soft capacity is given as described in this section according to the following formula:

$$C = \frac{1}{\ln 2 \cdot E_{photon}} \left(\frac{P^2_{r,\det}}{P_{r,\det} \cdot 1/\ln(M) + P_{b\_\det} \cdot \frac{2}{M-1} + P^2_{r,\det} \cdot \frac{M \cdot T_s}{\ln(M) \cdot E_{photon}}} \right) \quad (137)$$

In small distances detected signal power is a lot higher than the detected noise power (it will be figured out in the following section where numerical results will be reported). Therefore, in the denominator $P_{r,det}$ is a lot higher than the noise power P_{b_det}. Additionally $P_{r,det}$ is a lot higher than $P^2_{r,det}$. Thus, keeping in mind that in $P_{r,det}$ free space losses are included ($L_{fs} = \left(\frac{\lambda}{4\pi R} \right)^2$) it can be seen that:

$$C = \frac{1}{\ln 2 \cdot E_{photon}} \left(\frac{P^2_{r,\det}}{P_{r,\det} \cdot 1/\ln(M)} \right) = a\left(\frac{P^2_{r,\det}}{P_{r,\det}} \right) = aP_{r,\det} = g*(1/R^2) \quad (138)$$

where a, g denote the analogy. Therefore, for small distances where detected signal power is higher than the detected noise power the capacity and as a result the data rate (since in the proposed analysis $C=R_b$) is proportional to R^{-2}.

Now, in case of large distances detected noise power is a lot higher than the detected signal power. Therefore in the denominator P_{b_det} is a lot higher than the $P_{r,det}$ and $P^2_{r,det}$. Thus:

$$C = \frac{1}{\ln 2 \cdot E_{photon}} \left(\frac{P^2_{r,\det}}{P_{b,\det} \cdot 2/(M-1)} \right) = d*P^2_{r,\det} = m*(1/R^4) \quad (139)$$

where d, m denote the analogy. Therefore, for large distances where detected noise power is a lot higher than the detected signal power, the capacity and as a result the data rate is proportional to R^{-4}.

8.5.1 SNR vs Distance-APD detector

In this subsection the same analysis performed before for the dependence of capacity with distance for the single photon counting detectors, will be executed for the APD/PIN detectors for the dependence of SNR with distance.

As described in [Toyoshima07a] in small distances the dominant noise source is the shot noise. Thus, SNR can be expressed as follows (keeping in mind that in received power the free space losses are included):

$$SNR = \frac{\langle i_s \rangle^2}{N_0 B} = \frac{\langle i_s \rangle^2}{i^2_{ss}} = \frac{\left(P_{r,ap} \cdot R_d\right)^2}{2q \cdot P_{r,ap} \cdot R_d \cdot B} = \frac{\left(P_{r,ap} \cdot R_d\right)}{2q_d \cdot B} = a \cdot \left(\frac{1}{R^2}\right) \tag{140}$$

where a denotes the analogy. Therefore for small distances where shot noise is the dominant noise source SNR is proportional to R^{-2}.

In large distances the other noises dominate. Therefore:

$$SNR = \frac{\langle i_s \rangle^2}{N_0 B} = \frac{\langle i_s \rangle^2}{i^2_b + i^2_{th} + i^2_d} =$$

$$= \frac{\left(P_{r,ap} \cdot R_d\right)^2}{2q \cdot F \cdot I_b \cdot B + \dfrac{4k \cdot T \cdot B}{R_f \cdot M_a^2} + 2q \cdot F \cdot I_{dm} \cdot B + 2q \cdot I_u \cdot B} = p \cdot \left(\frac{1}{R^4}\right) \tag{141}$$

where p denotes the analogy. Thus for large distances SNR is proportional to R^{-4}.

8.6   Numerical Results

In this section numerical results using the proposed methodology are presented assuming single photon counting detectors. Results assuming both only one detector and a detector array are reported.

To begin with, assuming a single photon counting detector (no Array) the maximum achieved data rate is investigated for different link ranges in Astronomical Units (AU)[1], different receiver aperture diameters 4/6/8/10 m and different background radiance 15/85 W/m^2/µm/sr. The values for background radiance may be interpreted as low and high that could represent day/night time conditions or large/small Sun-Earth-Probe angles. The inputs to the link budget tool are listed in Table 26. In Table 27 detailed outputs for the case of the 4m receiver in 0.3/07/1.3 AU range assuming 15W/m^2/µm/sr radiance of planets and sky are presented. For the other cases the resulting data rates are reported in the following figures (Fig. 58-Fig. 64). For all the numerical results a power link margin of 4dBs is assumed.

---

[1] Distances include Venus and Mars orbits.

Table 26: Deep Space Link Inputs-One single detector (No array)

Variables	INPUTS
Wavelength (nm)	1550nm
Range link	0.3/0.5/0.7/1/1.3/2 AU
Elevation angle (deg)	20 deg
Transmit Power (W)	4W
Transmitter Diameter (m)	0.22m
Transmitter Secondary Diameter (m)	0m
Transmitter Efficiency	0.6
Receiver Aperture diameter	4/6/8/10m
Receiver secondary aperture	0
Receiver efficiency	0.4
Receiver quantum efficiency	0.5
Focal length of receiver	16m
Detector diameter	30e-6 m
Optical filter	0.2e-3μm
Atmospheric efficiency Vertical	0.98
Scintillation Loss	0.01 dB
Cirrus Loss	0.5dB
Link Margin	4 dB
Pointing RMS Error Value	$0.7\mu rad$
Probability Level	10^{-4}
Modulation	M-PPM
Guard Slots	M/4
Back ground noise reduction factor	0.5
Coding efficiency	0.8
Radiance of planets + Sky	15/85 $W/m^2/\mu m/sr$
Leakage Ratio	0
Detector Array size	1
Detector Dark Rate	$10^{12}e/s/m^2$
Blocking time	50ns
Jitter time	240ps

Table 27: Deep Space Link Budget Outputs-4m receiver, 0.3 /0.7/1.3 AU range, 15W/m^2/µm/sr radiance.

Variables	OUTPUTS
Transmitter Gain (dB)	112.985
Receiver Gain (dB)	138.178
Free Space Losses (dB)	-351.29 / -358.58 / -363.96
Atmospheric Transmittance	0.943
Scintillation Loss (dB)	0.01
Pointing Loss (dB)	1.95
Cirrus Loss (dB)	0.5
Signalling	
PPM order	128 / 64 / 256
Slot duration (ns)	0.25 / 2 / 1
ECC code rate	1/3 - ½ - 1/3
Symbol duration (ns)	40 / 160 / 320
Blocking/Jitter Losses	
Blocking Loss (dB)	3.9 / 1.25 / 0.54
Jitter Loss (dB)	1.7 / 0.285 / 0.31
Received Signal Power	
Received Signal Power (W)	2.02e-11 / 3.7e-12 / 1e-12
Received Signal flux (Ph/sec)	1.57e+8 / 2.9e+7 / 8.38e+6
Received Photons/symbol	6.29 / 4.6 / 2.68
Detected Signal Power	
Detected Signal Power (W)	2.2e-12 / 1e-12 / 3.54e-13
Detected Signal flux (Ph/sec)	1.7e+7 / 8e+6 / 2.76e+6
Detected Photons/symbol	0.692 / 1.3/ 0.88
Received Background Power	
Received Background Power (W)	2.1e-14
Received Background flux (Ph/sec)	162227
Received Background Photons/slot	4e-5 / 3e-4 / 1.6e-4
Detected Noise Power	
Detected Noise Power (W)	1.05e-14
Detected Noise flux (Ph/sec)	82013.6
Detected Photons/slot	2.05e-5 / 1.6e-4 / 8.2e-5
Capacity/Data Rate /BER/SER	
Soft Capacity(Mbits/sec)	78.33 / 23.87 / 12.9
Hard Capacity(Mbits/sec)	63.7 / 20.7 / 11.3
Data Rate (Mbits/sec)	58.33 / 18.75 / 8.33

SER	0.49 / 0.3 / 0.43
BER	0.248 / 0.15 / 0.21

In Fig. 58 the data rates for the low noise conditions, i.e. $H_b=15(W/m^2/\mu m/sr)$ versus the distance are reported for each aperture, assuming only one single detector (no detector array).
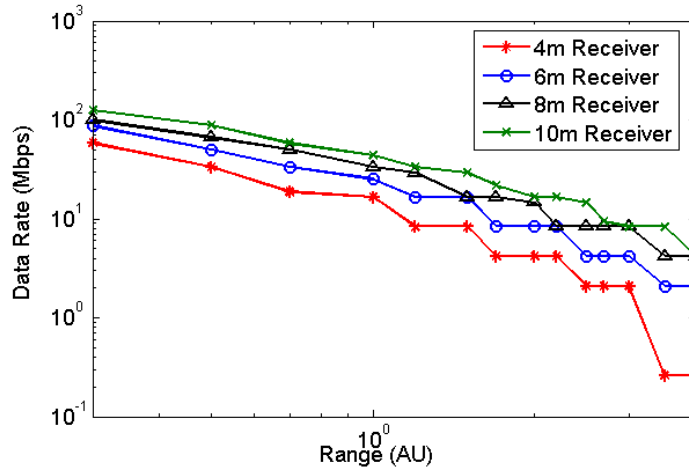
Fig. 58: Data Rate vs Range, $H_b=15\ W/m^2/\mu m/sr$, Different Receivers, No Array

In Fig. 59 the data rates for the high noise conditions, i.e. $H_b=85(W/m^2/\mu m/sr)$ versus the distance are reported for each aperture, assuming only one single detector (no detector array).
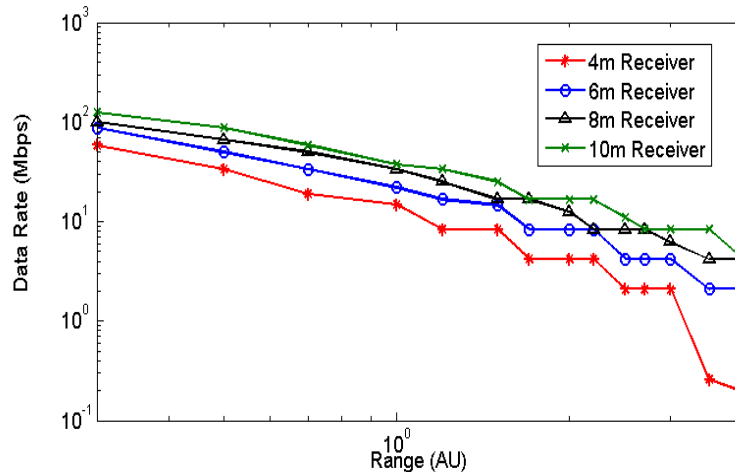
Fig. 59: Data Rate vs Range, $H_b=85\ W/m^2/\mu m/sr$, Different Receivers, No Array

Now, assuming a single photon counting detector array with size 32, the maximum achieved data rate is investigated for different ranges, different receiver aperture diameters 4/6/8/10 m and different background radiance 15/85 W/m^2/μm/sr. The same inputs as before are assumed instead of the detector array size which is 32. In Table 28 detailed outputs for the case of the 4m receiver in 0.3/07/1.3 AU range assuming 15W/m^2/μm/sr radiance of planets and sky are presented.

160

Table 28: Deep Space Link Budget Outputs-4m receiver, 0.3/0.7/1.3 AU range, 15W/m^2/µm/sr radiance.- Detector Array 32

Variables	OUTPUTS
Transmitter Gain (dB)	112.985
Receiver Gain (dB)	138.178
Free Space Losses (dB)	-351.29 / -358.58 / -363.96
Atmospheric Transmittance	0.943
Scintillation Loss (dB)	0.01
Pointing Loss (dB)	1.95
Cirrus Loss (dB)	0.5
Signalling	
PPM order	64 / 256 / 256
Slot duration (ns)	0.25 / 0.25 / 1
ECC code rate	1/3 – 1/3 – 1/3
Symbol duration (ns)	20 / 80 / 320
Blocking/Jitter Losses	
Blocking Loss (dB)	0.5 / 0.11 / 0.04
Jitter Loss (dB)	2.15 / 1.33 / 0.3
Received Signal Power	
Received Signal Power (W)	2.02e-11 / 3.7e-12 / 1e-12
Received Signal flux (Ph/sec)	1.57e+8 / 2.9e+7 / 8.38e+6
Received Photons/symbol	3.15 / 2.32 / 2.68
Detected Signal Power	
Detected Signal Power (W)	4.38e-12 / 1e-12 / 3.97e-13
Detected Signal flux (Ph/sec)	3.4e+7 / 8.3e+6 / 3.1e+6
Detected Photons/symbol	0.68 / 0.66 / 0.99
Received Background Power	
Received Background Power (W)	6.66e-13
Received Background flux (Ph/sec)	5.2e+6
Received Background Photons/slot	0.0013 / 0.0013 / 0.0052
Detected Noise Power	
Detected Noise Power (W)	3.37e-13
Detected Noise flux (Ph/sec)	2.63e+6
Detected Photons/slot	6.6e-4 / 6.6e-4 / 0.0026
Capacity/Data Rate /BER/SER	
Soft Capacity(Mbits/sec)	131.5 / 43 / 13.52
Hard Capacity(Mbits/sec)	98.84 / 33.5 / 10.12

Data Rate (Mbits/sec)	100 / 33.3 / 8.33
SER	0.5 / 0.54 / 0.47
BER	0.256 / 0.27 / 0.236

In Fig. 60 the data rates for the low noise conditions, i.e. $H_b=15$ (W/m²/μm/sr) versus the distance are reported for each aperture, assuming a detector array with size 32.
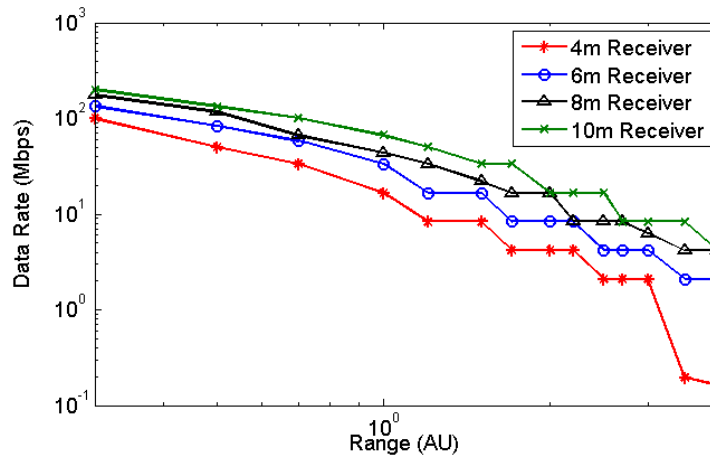
Fig. 60: Data Rate vs Range, $H_b=15$ W/m²/μm/sr , Different Receivers, Detector Array size 32

In Fig. 61 the data rates for the high noise conditions, i.e. $H_b=85$ (W/m²/μm/sr) versus the distance for each aperture are presented, assuming a detector array with size 32.
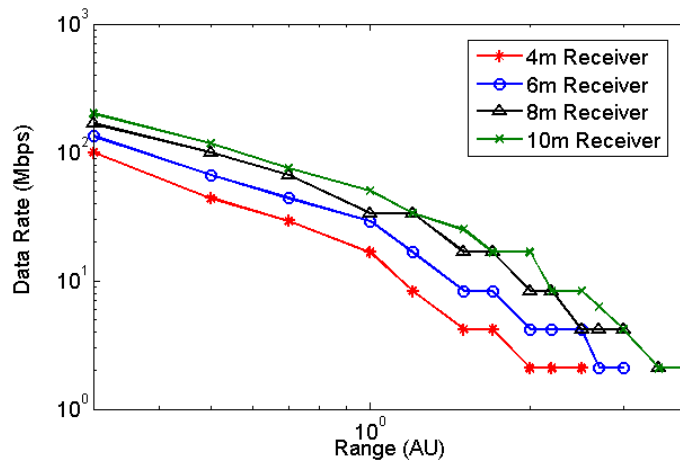
Fig. 61: Data Rate vs Range, $H_b=85$ W/m²/μm/sr , Different Receivers, Detector Array size 32

Comparing these first numerical results, it can be observed that for the given system considerations the achieved data rates with the detector array are higher for distances up to 1 AU. For large distances, since the received power is extremely low and in case of the detector array the noise photon rate is higher than the signal photon rate, it can be seen that slightly the same data rate or even higher can be achieved with only

one detector. When multiple detectors are used, on the one hand the blocking loss is minimized, but on the other hand the noise increases.

In Fig. 62 we illustrate the change in the slope of the achieved data rate versus the distance assuming a detector array with size 32 and a 10m aperture receiver. The transition from $1\backslash R^2$ to $1\backslash R^4$ can be observed around to 2 AU and 10Mbps.
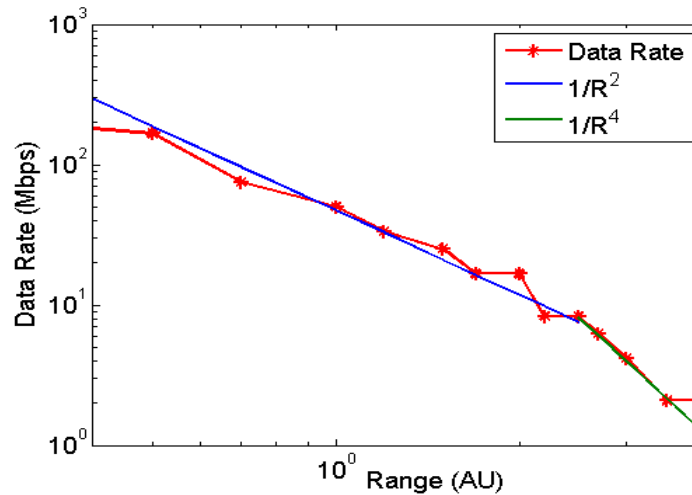
Fig. 62: Data Rate Slope versus Distance, Detector Array size 32, 10m Receiver

Finally, in order that the sensitivity of achieved data rate with the transmitter diameter is being investigated in the next Figures the achieved data rate for 3 different transmitter diameters i.e. 0.135m, 0.22m and 0.4m versus distance, for two receiver aperture diameters (6m and 10m) is reported. A detector array with size 32 is assumed and high noise conditions $H_b=85(W/m^2/\mu m/sr)$.
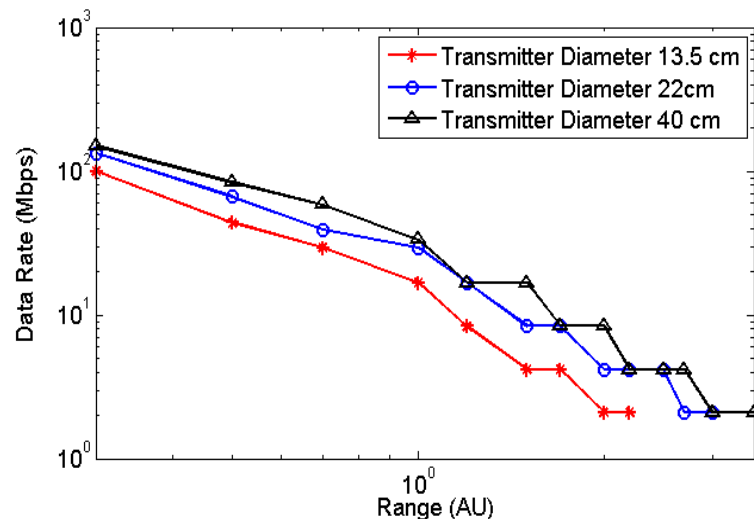
Fig. 63: Data Rate Slope versus Distance, Different transmitters, Detector Array size 32, 6m Receiver

163
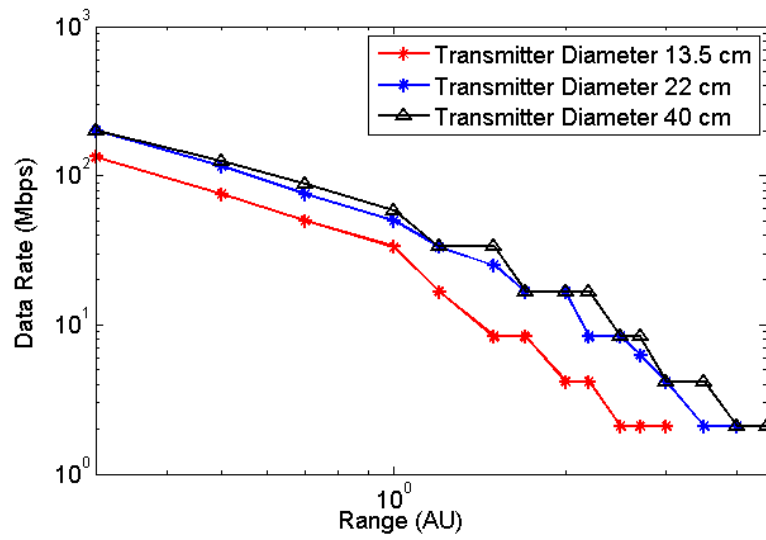
Fig. 64: Data Rate Slope versus Distance, Different transmitters, Detector Array size 32, 10m Receiver

9   CONCLUSIONS AND FUTURE WORK

In this Chapter the work carried out and presented in this PhD thesis is concluded and a few directions for future work are given.

9.1   General Conclusions

The Chapter 3 of the PhD thesis, is devoted on the modeling of Integrated Liquid Water Content (ILWC) time series. The main contributions of this chapter are:

- Methodologies based on stochastic differential equations for the generation of 2 and 3 dimensions ILWC time series, correlated on temporal and on spatial domains, are presented. Using the proposed methodology, ILWC statistics can be extracted. The performance of the ILWC synthesizers are tested in terms of first order statistics.

- The proposed synthesizers are used for the generation of cloud coverage statistics. Spatial and temporal variability of clouds is captured, while different cloud types (stratus, cumulus, etc.) can be simulated.

The topic of Chapter 4, is focused on the cloud attenuation and Cloud Free Line of Sight (CFLOS) statistics, for single and joint slant paths. The main contributions of this chapter are:

- Two synthesizers for the generation of cloud attenuation and CFLOS time series based on the 3D synthesizer reported in Chapter 3 are proposed. The synthesizers can be used for the generation of first and second order statistics of cloud attenuation and CFLOS for GEO and Non-GEO satellite communication systems. Both synthesizers take into account the elevation angle and the altitude of the stations, for high altitude stations for the estimation of cloud attenuation and CFLOS probability, respectively. Additionally, the spatial correlation of clouds along the slant path and between different locations (spatial diversity), is taken into account.

- Regarding the cloud attenuation synthesizer, clouds are classified based on their vertical extent and using their microphysical properties and the well-known Mie scattering theory, a unified space-time model for the prediction of induced attenuation due to clouds, for frequencies above Ka band [26.5-40 GHz] and up to optical range is presented. The proposed methodology is tested with data obtained from literature, showing encouraging results. Finally, single and joint cloud attenuation statistics from Ka to optical band are reported.

- Regarding the CFLOS synthesizer, on/off channel with cloud occurrence, a methodology for the generation of Cloud Free Line of Sight (CFLOS) time series correlated on temporal and

spatial domain, is presented. The vertical extent of clouds is used for the estimation of CFLOS time series.

- The spatial diversity technique for the mitigation of cloud coverage is investigated. Valuable statistics using the proposed synthesizers are presented.
- The proposed synthesizers can be used for the design of an optical satellite communication system.

Chapter 5 is devoted to the modeling of CFLOS probability for a given location or a spatial diversity scenario, without employing the difficulties of the implementation of the mathematical framework of stochastic differential equations, as in Chapter 4. The main contributions of this chapter are:

- A simple physical and mathematical theoretical model for the prediction of CFLOS probability along a single slant path and for separated on spatial domain multiple optical satellite links, is presented. For the accurate evaluation of CFLOS the elevation angle of the slant path, the altitude of ground stations and the spatial variability of clouds are considered.
- CFLOS probability for a given number of simultaneously available links for spatial multiplexing transmission technique is reported.

The topic of Chapter 6 of this thesis is mainly focused on the monthly variability of cloud coverage, the differences of cloud coverage between the north and south hemisphere and the optimum design of an optical ground station network. More specifically, the main contributions of this chapter are:

- The need of employing monthly-based statistics for the estimation of CFLOS is highlighted. Cloud coverage exhibits remarkable monthly variations, which cannot be observed when yearly averages are used. There are also great differences in the monthly cloud coverage probabilities (maximums and minimums) between the two hemispheres.
- It is firstly shown that ILWC monthly statistics can be sufficiently described by lognormal distribution.
- The synthesizers reported in Chapter 4 are modified in order that the monthly variability and hemisphere differences are captured.
- Analytical formulas based on the methodology presented in Chapter 5 are proposed, for the estimation of single and joint monthly CFLOS availability.
- Two novel optimization algorithms for the optimum selection of OGS, for mitigation of cloud coverage are reported. These algorithms are aware of the clouds monthly variability and take advantage of the two hemisphere differences. The main contribution of these algorithms is that they guarantee a minimum availability per month which is not necessarily

the same for each month. The benefits of using optical stations in different hemispheres are highlighted.

- An optimization algorithm for the identification of active stations per month, is also reported.

Chapter 7 is focused on the propagation of the optical signal under CFLOS conditions for an optical satellite communication link. In this chapter the methodologies for the estimation of received power under CFLOS condition, taking into account the phenomena that affect the propagation of the optical signal, are proposed. More specifically, the main contributions of this chapter are:

- Methodologies for the uplink and downlink propagation of the optical signal are reported.
- For the validation of the proposed methodologies, real experimental irradiance measurements from the ARTEMIS GEO optical satellite campaign are employed.
- Regarding the downlink propagation, a methodology for the estimation of aperture averaging factor for a central obscured aperture is presented and it is validated with actual measurements from the ARTEMIS campaign.
- Regarding the uplink propagation, a unified methodology for the generation of received irradiance/power time series, for an optical uplink GEO satellite feeder link is presented. The proposed methodology takes into account the turbulence and miss-pointing effects among others, while it benefits of the use of Stochastic Differential Equations (SDEs), driven by fractional Brownian motion, for the incorporation of the scintillation effects. The methodology is validated with actual measurements from the ARTEMIS optical satellite measurement campaign. The proposed methodology can be used for system level simulations and valuable results for the feasibility of the optical satellite links can be extracted.
- A methodology for the estimation of the atmospheric conditions using downlink irradiance measurements, is presented.

The topic of Chapter 8 is focused on the design of the Deep Space Satellite communication links. The main contributions of this chapter are:

- The estimation of signal and noise photon rates in order that the maximum data rate depending on the link characteristics, is achieved.
- A tool based on the CCSDS (Consultative Committee for Space Data Systems) for High Photon Efficiency (HPE), for the estimation of the link budget for an optical deep space mission, is proposed.
- The elements that must be taken into account for the accurate estimation of signal and noise photon rates, are analyzed.

- A practical methodology that allows the link designer to select the main signaling parameters (modulation order, code rate, slot width), without resorting to lengthy coded Bit Error Rate (BER) evaluations, that otherwise need to be run for a large parameter set, is presented. This allows faster link budget calculations, e.g. for performing trade-off studies.

- A sensitivity analysis of various hypothetical deep space missions is performed.

9.2   Future Work

Based on the results and the limitations of the models developed under the framework of this thesis, a number of actions can be identified.

To begin with, regarding the ILWC time series generator proposed in the third chapter for the incorporation of the temporal correlation of ILWC, the annual parameters from the ITU-R P. 1853 [ITU1853-1] are employed. Inspired from the sixth chapter which is focused on the monthly variability of ILWC, a research for the temporal evolution of ILWC for each month, or depending on the probability of ILWC higher than zero (probability of cloud coverage), can be conducted.

Additionally, in the 3D ILWC generator the expressions used for the vertical extent of clouds and the cloud base height are general. Since high altitude stations are of prominent importance for optical satellite communications systems, studies about the height of cloud base and the vertical extent of clouds especially for high altitude stations, can be proved beneficial.

Moving on to the OGSN dimensioning, methodologies for GEO and MEO constellation satellite communication systems have been proposed. However, in the proposed analysis the Earth is separated in specific regions. An interesting extension would be the OGSN dimensioning without separating the Earth in specific regions, using the whole Earth as input.

Finally, since optical communications are attractive for MEO and LEO satellite communication systems methodologies, for the estimation of received power taking into account the turbulence effects, must be developed. It must be noted that turbulence effects are different in case of MEO/LEO satellite communication systems, from the GEO case.

10   APPENDIX

More information about the use of Stochastic Differential Equations (SDE) driven by fractional Brownian motion (fBm) for the generation of a zero-mean unity-variance Gaussian process with a power spectral density of low-pass shape, will be reported. The procedure exhibited in this APPENDIX is based on [Kourogiorgas13].

To begin with the underlined Gaussian process will be generated through [Shao95]:

$$d\chi_t = f(t, \chi_t)dt + g(t, \chi_t)dB_H \tag{142}$$

Since for a given variance, χ_t can be considered as a Gaussian process with zero mean, we use the Langevin equation with fBm (fractional Langevin equation), to model the time series of log-amplitude, given that the variance is equal to 1 ($\chi_{t,1}$) [Kourogiorgas13], [Shao95]:

$$d\chi_{t,1} = -\lambda_s \chi_{t,1}dt + \sigma dB_H \tag{143}$$

The solution of the above equation with zero initial value is [Shao95]:

$$\chi_{t,1} = e^{-\lambda_s t}\sigma \int_0^t e^{\lambda_s u} dB_u^H \tag{144}$$

The above process is called fractional Ornstein-Uhlenbeck process and it is a Gaussian process with zero mean. The co-variance of χ_t and χ_{t+s} is [Shao95]:

$$Cov(\chi_{t,1}, \chi_{t+s,1}) = \sigma^2 \frac{\Gamma(2H+1)\sin(\pi H)}{2\pi} \int_{-\infty}^{+\infty} e^{isy} \frac{|y|^{1-2H}}{\lambda_s^2 + y^2} dy \tag{145}$$

where H is Hurst index. Therefore, the variance of the Ornstein-Uhlenbeck process is :

$$\sigma_{\chi_{t,1}}^2 = \sigma^2 \frac{\Gamma(2H+1)\sin(\pi H)}{2\pi} \int_{-\infty}^{+\infty} \frac{|y|^{1-2H}}{\lambda_s^2 + y^2} dy \tag{146}$$

Since, firstly we want to have a unitary variance process we set:

$$\sigma = \frac{1}{\sqrt{\dfrac{\Gamma(2H+1)\sin(\pi H)}{2\pi} \displaystyle\int_{-\infty}^{+\infty} \dfrac{|y|^{1-2H}}{\lambda_s^2 + y^2} dy}} \tag{147}$$

For the energy spectrum of fractional Ornstein-Uhlenbeck process it holds that [Shao95]:

$$F_{\chi_{t,1}}(f) = \sigma^2 \frac{F_{\omega_b}(f)}{\lambda_s^2 + (2\pi f)^2} \tag{148}$$

where $F_{\omega_b}(f)$ is the energy spectrum of fractional Gaussian noise and it also holds that:

$$F_{\omega_b}(f) \sim f^{-(2H-1)} \qquad (149)$$

From (148) and (149), here results for high frequencies that:

$$F_{\chi_{t,1}}(f) \sim f^{-(2H+1)} \qquad (150)$$

with corner frequency $\omega_c = \lambda_s^{\frac{1}{H+1/2}}$. Corner frequency can be modelled from the temporal spectrum of turbulence.

To sum up, from the slope of the power spectral density, the Hurst index is calculated using (150). Then, λ_s parameter is computed from corner frequency and next the parameter σ from (147).

11 REFERENCES

[AGI] "AGI STK." [Online]. Available: https://www.agi.com/products/byproduct-type/applications/stk/.

[Alexander97] S.B. Alexander "Optical communication receiver design", 1997, SPIE

[ANEX-ARTEMIS] ARTEMIS-OGS Laser Link Experiments Results (ESA), CFI document provided by ESA, Filename: ARTEMIS-OGS results.pdf Includes: Annex A - ARTEMIS-OGS Laser Link Experiments Results, Annex B - Summary Table of ARTEMIS-OGS Laser Link Experiments.

[Andrews05] L. Andrews, R. Phillips, "Laser Beam Propagation through Random Media" SPIE Press , 2005.

[Andrews06] L. C. Andrews, R. L. Phillips,R. J. Sasiela,R. R. Parenti: "Strehl ratio and scintillation theory for uplink Gaussian-beam waves: beam wander effects",Optical Engineering, vol. 45, 2006.

[Alonso04]A. Alonso, M. Reyes, Z. Sodnik "Performance of satellite-to-ground communications link between ARTEMIS and the Optical Ground Station". Proc. SPIE 5572, Optics in Atmospheric Propagation and Adaptive Systems, VII, 372 November 2004.

[Barron06] R. J. Barron and D. M. Boroson, "Analysis of capacity and probability of outage for free-space optical channels with fading due to pointing and tracking error," in Proceedings of SPIE, vol. 6105. Proceedings of the SPIE, March 2006.

[Biswas03] A. Biswas, & S. Piazzolla, "Deep-space optical communications downlink budget from Mars: System parameters. IPN Progress Report, 42(154), 0-1, 2003.

[Biswas10] A. Biswas, H. Hemmati, S. Piazzolla, B. Moision, K. Birnbaum, K. Quirk, "Deep-Space Optical Terminals (DOT) Systems Engineering", IPN Progress Report 42–183, Jet Propulsion Laboratory, November 2010.

[Bohren83] C. F. Bohren, D. R. Huffman, "Absorption and scattering by a sphere." Absorption and Scattering of Light by Small Particles (1983): 82-129.

[Boroson09] D. M. Boroson et al.," The Lunar Laser Communications Demonstration (LLCD)," Third IEEE International Conference on Space Mission Challenges for Information Technology.

[Boroson14]D. M. Boroson, B. S. Robinson, "The Lunar Laser Communication Demonstration: NASA's First Step Toward Very High Data Rate Support of Science and Exploration Missions", Space Sci Rev (2014) 185:115–128.

[Brumley16] R. H. Brumley II, et al., "Optical Communication System", Laser Light Communications (LLC), US Patent 9,438,341, 2016.

[Calvo14] R. Mata Calvo, P. Becker, D. Giggenbach, F. Moll, M. Schwarzer, M. Hinz, Z. Sodnik; "Transmitter diversity verification on ARTEMIS geostationary satellite" Proc. SPIE 8971, Free-Space Laser Communication and Atmospheric Propagation XXVI, 897104, March 2014.

[Caplan07] D. O. Caplan, "Laser communication transmitter and receiver design", Journal of Optical and Fiber Communication Reports 4, 225-362, 2007 Springer

[CCSDS17a] CCSDS Green Book, "Real-Time Weather and Atmospheric Characterization data", Informational Report, CCSDS 140.1-G-1, May 2017.

[CCSDS17b] CCSDS Red Book, Draft Recommendation for Space Data System Standards "Optical Communications Coding & Synchronization Sub layer.2017

[CCSDSc] HIGH PHOTON EFFICIENCY OPTICAL COMMUNICATIONS PHYSICAL LAYER

[Comeron05] A. Comeron, F. Dios, A. Rodriguez, J. A. Rubio, M. Reyes, A. Alonso "Modeling of power fluctuations induced by refractive turbulence in a multiple-beam ground-to-satellite optical uplink" Proc. SPIE 5892, Free-Space Laser Communications V, 58920 August, 2005.

[Degnan74] J. J. Degnan, and B. J. Klein, (1974). Optical antenna gain. 2: Receiving antennas. Applied optics, 13(10), 2397-2401.

[Degnan93] J.J Degnan "Millimeter Accuracy Satellite Laser Ranging: A Review", in Contributions of Space Geodesy to Geodynamics: Technology, D. E. Smith and D. L. Turcotte (Eds.), AGU Geodynamics Series Vol.25, pp. 133-162, 1993.

[Dimitrov15] S. Dimitrov, et al., Digital modulation and coding for satellite optical feeder links with pre-distortion adaptive optics. Int. J. Satell. Commun. Network., 34: 625– 644. doi: 10.1002/sat.1163.

[Dios04] F. Dios et al., "Scintillation and beam-wander analysis in an optical ground station–satellite uplink", Applied Optics, vol 43 no.19, 2004.

[Dolinar] S. Dolinar et.al. "Fundamentals of Free-Space Optical Communications", JPL, https://ntrs.nasa.gov/search.jsp?R=20130003283

[Fields09] R. Fields, et al. "NFIRE-to-TerraSAR-X laser communication results: satellite pointing, disturbances, and other attributes consistent with successful performance," Proc. SPIE 7330, Sensors and Systems for Space Applications III, 73300Q, 2009.

[Fried75] D. L. Fried, "Analysis of aperture averaging measurements", NASA Report, 1975 https://ntrs.nasa.gov/search.jsp?R=19750014049.

[EUBroadband] http://publications.europa.eu/webpub/eca/special-eports/broadband-12-2018/en/

[Fields11] R. Fields et al., "5.625 Gbps bidirectional laser communications measurements between the NFIRE satellite and an Optical Ground Station," International Conference on Space Optical Systems and Applications (ICSOS), Santa Monica, CA pp. 44-53, 2011.

[Fuchs15] C. Fuchs and F. Moll, "Ground station network optimization for space-to ground optical communication links," in IEEE/OSA J. of Opt. Comm. and Net., vol. 7, no. 12, pp. 1148-1159, Dec.2015.

[Giggenbach12] D. Giggenbach, F. Moll, and N. Perlot "Optical Communication Experiments at DLR." Journal of the National Institute of Information and Communications Technology 59, 125-134, 2012.

[Giggenbach15] D. Giggenbach, H. Henniger "Fading-loss assessment in atmospheric free space optical communication links with on-off keying", Opt. Eng. 2008, 47(4):046001, 1–6.

[Hemmati06]H. Hemmati, Ed., "Deep Space OpticalCommunications". New York: Wiley, 2006.

[Hemmati09] H. Hemmati, "Near-Earth Laser Communications". Boca Raton: CRC Press, 2009.

[Hemmati11] H. Hemmati, A. Biswas and I. B. Djordjevic, "Deep-Space Optical Communications: Future Perspectives and Applications," in Proceedings of the IEEE, vol. 99, no. 11, pp. 2020-2039, Nov. 2011.

[Horwath06] Joachim Horwath, Markus Knapek, Bernhard Epple, Martin Brechtelsbauer, Brandon Wilkerson, "Broadband backhaul communication for stratospheric platforms: the stratospheric optical payload experiment (STROPEX)," Proc. SPIE 6304, Free-Space Laser Communications VI, 63041N (1 September 2006).

[Ishimaru78] A. Ishimaru, "Wave propagation and scattering in random media", Academic Press, 1978.

[ITU1622] ITU-R recommendation P.1622 Prediction methods required for the design of Earth-space systems operating between 20 THz and 375 THz 2003.

[ITU1853-1] ITU- Recommendation P.1853-1 "Tropospheric attenuation time series synthesis," ITU-R P.1853-1, vol. ITU-R P Series Recommendations Radio wave Propagation, 2012.

[ITU840-6] ITU-R Recommendation P.840-6, "Attenuation due to clouds and fog." Geneva, Switzerland, 2013.

[ITU1742] ITU-R Recommendation SA.1742, "Technical and operational characteristics of interplanetary and deep-space systems operating in the space-to-Earth direction around 283 THz," Geneva, 2006.

[Jeannin08] Jeannin, L. Feral, H. Sauvageot and L. Castanet, "Statistical Distribution of Integrated Liquid Water and Water Vapor Content From Meteorological Reanalysis , IEEE Transactions on Antennas and Propagation, vol. 56, pp. 3350-3355, 2008.

[Karagiannis12] G. A. Karagiannis, A. D. Panagopoulos, J. D. Kanellopoulos, "Multidimensional Rain Attenuation Stochastic Dynamic Modeling: Application to Earth–Space Diversity Systems," IEEE Transactions on Antennas and Propagation, vol. 60, no.11, pp.5400-5411, Nov. 2012.

[Karatzas91] I. Karatzas and S. E. Shreve, Brownian Motion and Stochastic Calculus.New York: Springer-Verlag, 1991.

[Karlin75] S. Karlin and H. M. Taylor, A First Course in Stochastic Processes. New York: Academic, 1975.

[Kaushal17] H. Kaushal and G. Kaddoum, "Optical Communication in Space: Challenges and Mitigation Techniques," in IEEE Communications Surveys & Tutorials, vol. 19, no. 1, pp. 57-96, Firstquarter 2017.

[Klein74] B. J. Klein, and J. J. Degnan, (1974). "Optical antenna gain. 1: Transmitting antennas". Applied optics, 13(9), 2134-2141.

[Kourogiorgas13] C. Kourogiorgas., A.D. Panagopoulos "A Tropospheric Scintillation Time Series Synthesizer based on Stochastic Differential Equations", 19th Ka and Broadband Communications, Navigation and Earth Observation Conference   2013.

[Lambert96] S. G. Lambert, W. L. Casey and J. R. Lesh, "Laser Communications in Space", Opt. Eng. 35(5), 1513-1514 (May 01, 1996).

[Lee14] P. Lee, et al, "Phobos And Deimos & Mars Environment (PADME): A LADEE-Derived Mission to Explore Mars's Moons and the Martian Orbital Environment", 45th Lunar and Planetary Science Conference (2014), paper 2288.

[Leonard16] N. Leonhard, et al., "Real-time adaptive optics testbed to investigate point-ahead angle in pre-compensation of Earth-to-GEO optical communication," Opt. Express 24, 13157-13172 (2016).

[Liao17] S. K. Liao, et al. Satellite-to-ground quantum key distribution. Nature 2017; 549: 43–47.

[Luini14] L. Luini and C. Capsoni, "Modeling High-Resolution 3-D Cloud Fields for Earth-Space Communication Systems," IEEE Transactions on Antennas and Propagation, vol.62, no.10, pp.5190,5199, Oct. 2014.

[Luini16] L. Luini, R. Nebuloni, "Impact of Clouds from Ka Band to Optical Frequencies", Chapter 8, Radio Wave Propagation and Channel Modeling for Earth–Space SystemsTaylor and Francis Group, CRC Press, 2016.

[Manning]R. M. Manning, "The SCaN Optical Satellite link assessment tool- Part 2, the physical basis of the calculations-optical satellite link budget component", NASA Internal Report.

[Meera98] S. Meera, and V. Vilnrotter. "Symbol-error probabilities for pulse-position modulation signaling with an avalanche photodiode receiver and Gaussian thermal noise." The Telecommunications and Mission Operations Progress Report 42-134, April–June 1998 (1998): 1-11.

[Moision05] B. Moision and J. Hamkins, "Coded modulation for the deep space optical channel: serially concatenated PPM," IPN Progress Report, vol. 42-161, 2005.

[Moision08] B. Moision and W. Farr, "Communication limits due to photon detector jitter," IEEE Photonics Technology Letters, vol. 20, no. 9, pp. 715–717, May 2008.

[Moision11] B. Moision and S. Piazzolla, "Blocking losses on an optical communications link," in Space Optical Systems and Applications (ICSOS), 2011 International Conference on, May 2011, pp. 368 – 377.

[Moision12] B. Moision, J. Wu, & S. Shambayati, "An optical communications link design tool for long-term mission planning for deep-space missions. In Aerospace Conference, March, 2012 IEEE (pp. 1-12).

[Moision14] B. Moision and Hua Xie. "An approximate link equation for the direct-detected optical PPM link." Interplanet. Netw. Prog. Rep 199.27 (2014): 1.

[Moll11] F. Moll and M. Knapel "Free-space laser communications for satellite downlinks: Measurements of the atmospheric channel". Proceedings of IAC2011. IAC 2011, Cape Town., 03.-07.Oct. 2011.

[Net16] M. S. Net et al., "Approximation methods for estimating the availability of optical ground networks," J. Opt. Commun. Netw., vol. 8, no. 10, pp. 800–812, 2016.

[NSR15] Global Satellite Capacity Supply and Demand Study, 12th Edition, A Region-Specific Supply and Demand Analysis of the Commercial Satellite Transponder Market for 2014 – 2024, 2015, NSR

[Ortiz00] G. G. Ortiz, J. V. Sandusky and A. Biswas "Design of the optoelectronic receiver for deep-space optical communications", Proc. SPIE 3932, Free-Space Laser Communication Technologies XII, 127 (May 2, 2000); doi:10.1117/12.384304.

[O3b] O3b satellite networks. [Online]. Available: http://www.o3bnetworks.com/o3b-advantage/our-technology

[Panagopoulos04] A. D. Panagopoulos, P.-D. M. Arapoglou, P. G. Cottis "Satellite Communications at Ku, Ka and V bands, Propagation Impairments and Mitigation Techniques", IEEE Communication Surveys and Tutorials, 3rd Quarter, pp.1-13, October 2004.

[Papoulis02] A. Papoulis., Pillai, Probability, "Random Variables and Stochastic Processes" NY, USA: McGraw-Hill, 2002.

[Perlot07] N. Perlot et al. "Results of the optical downlink experiment KIODO from OICETS satellite to optical ground station Oberpfaffenhofen (OGS-OP)" Proc. SPIE 6457, Free-Space Laser Communication Technologies XIX and Atmospheric Propagation of Electromagnetic Waves, 645704 XIX February 2007.

[Perlot12] N. Perlot and J. Perdigues-Armengol, "Model-oriented availability analysis of optical GEO-ground links," Proc. SPIE, vol. 8246, p. 82460P, Feb. 2012.

[Petit16] C. Petit, et. al. "Investigation of adaptive optics performance through propagation channel characterization with the Small Optical TrAnsponder SOTA" Optical Engineering, SPIE, 55 (11), pp.111611. 2016.

[Portillo17] I. del Portillo, M. Sanchez, B. Cameron and E. Crawley, "Optimal location of optical ground stations to serve LEO Spacecraft" 2017 IEEE Aerospace Conf. Big Sky, MT, 2017, pp. 1-16.

[Report1] Politecnico di Milano, ONERA, Joanneum Research, ''CHARACTERISATION AND MODELING OF PROPAGATION EFFECTS IN 20-50 GHz BAND'', Final Report for the European Space Agency, ESA/ESTEC Contract N. 17760/03/NL/JA. Noordwijk, The Netherlands: ESA Publication Division, ch. 3.2.4

[Reyes04a] M. Reyes, A. Comeron, A. Alonso, A. Rodriguez, J. A. Rubio, V. F. Dios, S. Chueca, Zoran Sodnik; "Ground-to-satellite bidirectional laser links for validation of atmospheric turbulence model". Proc. SPIE 5160, Free-Space Laser Communication and Active Laser Illumination III, 44, January 2004.

[Reyes04b] M. Reyes, A. Alonso, S. Chueca, J. s J. Fuensalida, A. Comeron, V. F. Dios, A. Rodriguez, J. A. Rubio, Zoran Sodnik "Propagation statistics of ground-satellite optical links with different turbulence conditions" Proc. SPIE 5572, Optics in Atmospheric Propagation and Adaptive Systems VII, 211, November 2004.

[Romba04] J. Romba, Z. Sodnik, M. Reyes, A. Alonso, A. Bird "ESA's bidirectional space-to-ground laser communication experiments" Proc. SPIE 5550, Free-Space Laser Communications IV, 287, October 2004.

[Sandalidis11] H. G. Sandalidis, "Performance of a laser Earth-to-satellite link over turbulence and beam wander using the modulated gamma–gamma irradiance distribution," Appl. Opt. 50, 952-961 (2011).

[Sandalidis10] H. G. Sandalidis, "Performance Analysis of a Laser Ground-Station-to-Satellite Link With Modulated Gamma-Distributed Irradiance Fluctuations," J. Opt. Commun. Netw. 2, 938-943 (2010).

[scattport] The Light Scattering Information Portal website. http://www.scattport.org/, accessed July 2014.

[Shao95] Y. Shao, "The Fractional Ornstein-Uhlenbeck Process as a Representation of Homogeneous Eulerian Velocity Turbulence", Physica D 1995 83, pp. 461-477, 1995.

[SenGupta09]A. SenGupta "Advances in Multivariate Statistical Methods", World Scientific Vol. 4, 2009.

[Sodnik17] Z. Sodnik, C. Heese, P.-D. Arapoglou, K.-J. Schulz, I. Zayer, R. Daddato, "Deep-space Optical Communication System (DOCS) for ESA's Space Weather Mission to Lagrange Point L5," IEEE ICSOS 2017 IEEE International Conference on Space Optical Systems and Applications, 2017.

[Stubenrauch13] C. J. Stubenrauch, et al. "Assessment of Global Cloud Datasets from Satellites: Project and Database Initiated by the GEWEX Radiation Panel." Bulletin of the Am. Meteor.Soc. 94.7 (2013): 1031-1049.

[Takenaka17] H. Takenaka, et al. "Satellite-to-ground quantum-limited communication using a 50-kg-class microsatellite" Nature Photonics volume 11, pages 502–508, 2017.

[Tolker02]T. Tolker-Nielsen and G. Oppenhauser, "In-orbit test result of an op-erational intersatellite link between ARTEMIS and SPOT 4," inProc.SPIE, Free-Space Laser Commun. Technol. XIV, San Jose, CA, USA,Jan. 2002, vol. 4639, pp. 1–15.

[Toyoda97] M. Toyoda "Measurement of laser-link-scintillation between ETS-VI and a ground optical station" Proc. SPIE 2990, Free-Space Laser Communication Technologies IX, 287 April 1997.

[Toyoshima96] M. Toyoshima et al "Measurements of background noise from the earth surface using the ETS-VIILCE" Proc. SPIE 2699, Free-Space Laser Communication Technologies VIII, 93, April 1996.

[Toyoshima98] M. Toyoshima and K. Araki, "Far-field pattern measurement of an onboard laser transmitter by use of a space-to-ground optical link," Appl. Opt. 37, 1720-1730, 1998.

[Toyoshima00] M. Toyoshima and Kenichi Araki "Effects of time averaging on optical scintillation in a ground-to-satellite atmospheric propagation," Appl. Opt. 39, 1911-1919, 2000.

[Toyoshima05] M. Toyoshima et al. "Long-term statistics of laser beam propagation in an optical ground-to-geostationary satellite communications link," in IEEE Transactions on Antennas and Propagation vol. 53, no. 2, pp. 842-850 February 2005.

[Toyoshima06] M. Toyoshima "Trends in satellite communications and the role of optical free-space communications [Invited]," J. Opt. Netw. 4, 300-311, 2005.

[Toyoshima07a] M. Toyoshima, et.al, "Comparison of microwave and light wave communication systems in space applications". Opt. Eng. 0001;46(1):015003-015003-7.

[Toyoshima07b] M. Toyoshima et al. "Laser beam propagation in ground-to-OICETS laser communication experiments. Proc. SPIE 6551, Atmospheric Propagation IV, 65510A May 2007.

[Toyoshima08] M. Toyoshima et al. "Ground-to-satellite laser communication experiments," in IEEE Aerospace and Electronic Systems Magazine, vol. 23, no. 8, pp. 10-18, Aug. 2008.

[Tyson96] R. K. Tyson, "Adaptive optics and ground-to-space laser communications", Appl. Opt. 1996; 35(19):3640–3646.

[Yura83] H.T. Yura, W.G. McKinley "Aperture averaging of scintillation for space-to-ground optical communications", Applied Optics, Vol. 22, no. 11, 1983.

[Vetelino07] F. S. Vetelino, C. Young, and L.Andrews, "Fade statistics and aperture averaging for Gaussian beam waves in moderate-to-strong turbulence," Appl. Opt.   46, 3780-3789 2007

[Wilson97a] K. Wilson et al. "Overview of the Ground-to-Orbit Lasercom Demonstration (GOLD). Proc. SPIE 2990, Free-Space Laser Communication Technologies" IX, 23 April 1997

[Wilson97b] K. Wilson et al. "Results from Phase-1 and Phase-2 GOLD experiments." 1997.

12 PUBLICATIONS LIST

Publications in IEEE/International journals:

[J1] **Lyras N.K.**, Kourogiorgas C.I., Panagopoulos A.D., "Cloud Attenuation Statistics Prediction From Ka-Band to Optical Frequencies: Integrated Liquid Water Content Field Synthesizer," in IEEE Transactions on Antennas and Propagation, vol. 65, no. 1, pp. 319-328, Jan. 2017.

[J2] **Lyras N.K**, Kourogiorgas C.I, Panagopoulos A. D "Cloud Free Line of Sight Prediction Modeling for Optical Satellite Communication Networks", in IEEE Communications Letters , vol.21 , no.7 , pp.1537-1540, July 2017.

[J3] Charilaos I. Kourogiorgas, Daniele Tarchi, Alessandro Ugolini, **Nikolaos K. Lyras**, Pantelis-Daniel Arapoglou, Athanasios D. Panagopoulos ,Giulio Colavolpe Alessandro Vanelli-Coralli "Capacity Statistics Evaluation for Next Generation Broadband MEO Satellite Systems", in IEEE Transactions on Aerospace and Electronic Systems , vol.53, no.5, pp.2344-2358, Oct.2017.

[J4] Alberto Mengali, Charilaos I. Kourogiorgas, **Nikolaos K. Lyras**, Bhavani Shankar M.R, Farbod Kayhan, Athanasios D. Panagopoulos, Thomas Baumer, Konstantinos Liolis "Ground-to-GEO Optical Feeder Links for Very High Throughput Satellite Networks: Accent on Diversity Techniques", in International Journal of Satellite Communications and Networking., 2017.

[J5] **Lyras N.K.**, Efrem C.N., Kourogiorgas C.I., Panagopoulos A.D. "Optimum Monthly-Based Selection of Ground Stations for Optical Satellite Networks" in IEEE Communications Letters vol. 22, no. 6, pp.1192-1195, June 2018.

[J6]**Lyras N.K.,** Efrem C.N., Kourogiorgas C.I., Panagopoulos A.D. "Medium earth orbit optical satellite communication networks: Ground terminals selection optimization based on the cloud-free line-of-sight statistics" in International Journal of Satellite Communications and Networking. 2018, 1–15. https://doi.org/10.1002/sat.1289.

[J7] Kapsis T., **Lyras N. K.** and Panagopoulos A. D. "Long Term Irradiance Statistics for GEO Downlinks: Validation with ARTEMIS Experimental Measurements" PIERL, Vol. 82, page 89-94, 2019.

[J8] **Lyras N. K.**, Kapsis T. , and Panagopoulos A. D "Monthly Cloud Free LOS Time Series Generator for Optical Satellite Links", in PIERL, vol.85, 25-30, 2019.

[J9] Kapsis T., **Lyras N. K.,** Kourogiorgas C.I. and Panagopoulos A. D. "Time Series Irradiance Synthesizer for Optical GEO Satellite Downlinks in 5G Networks" in Future Internet, Special Issuer on Satellite Communications in 5G Era, 2019.

[J10] **Lyras N. K.**, Panagopoulos A. D. and Arapoglou P.-D. M. "Deep Space Optical Communication Link Engineering: Sensitivity Analysis", IEEE Aerospace & Electronics Systems Magazine, 2019 (minor Revision).

[J11] **Lyras N. K.**, Efrem C.N., Kourogiorgas C.I., Panagopoulos A. D. and Arapoglou P.-D. M. "Optimizing the Ground Network of MEO Optical Satellite Communication Systems", IEEE Systems Journal, 2019 (under Review).

[J12] **Lyras N. K.**, Kourogiorgas C.I, Panagopoulos A. D., et al., "Long Term Irradiance Statistics for Optical GEO Satellite Feeder Links" , Wireless Personal Communications, Springer, 2019 (under Review).

Publications in International Conferences:

[C1] **Lyras N.K.**, Kourogiorgas C.I., Panagopoulos A.D., "Cloud attenuation time series synthesizer for earth-space links operating at optical frequencies," in Antennas and Propagation in Wireless Communications (APWC), 2015 IEEE-APS Topical Conference on , vol., no., pp.638-641, 7-11 Sept. 2015.

[C2] Papafragkakis A.Z., **Lyras N.K.**, Kourogiorgas C.I., Panagopoulos A.D., "Propagation measurements campaign in Athens with ALPHASAT at Ka-band using Software Defined Radio technologies," in Electromagnetics in Advanced Applications (ICEAA), 2015 International Conference on , vol., no., pp.634-637, 7-11 Sept. 2015.

 [C3] **Lyras N.K**., Kourogiorgas C.I., Panagopoulos A. D., "Joint Statistics of Cloud Attenuation induced on Multiple Optical Satellite Links", 21th Ka band Conference, Bologna, Italy Oct 2015.

[C4] Papafragkakis, A.Z., **Lyras N.K**., Kourogiorgas C.I., Panagopoulos, A.D., " Deploying a Ka-band SDR beacon receiver targeting ALPHASAT: challenges, implementation and propagation measurements," 21th Ka band Conference, Bologna, Italy Oct 2015.

[C5] **Lyras N.K**., Kourogiorgas C.I, Panagopoulos A. D.," Energy Efficient Broadband Satellite Communication Systems Design at Frequencies Above 10GHz", 11th International Conference on Communications, Electromagnetics and Medical Applications, Athens, Greece 2016.

[C6] **Lyras N.K.**, Kourogiorgas C.I, Panagopoulos A. D and Ventouras S., "Rain Attenuation Statistics At Ka and Q Band in Athens Using SST and Short Scale Dynamic Diversity Gain Evaluation", 2016 Loughborough Antennas & Propagation Conference (LAPC), Loughborough**,** 2016, pp. 1-5.

[C7] **Lyras N.K.**, Kourogiorgas C.I, Panagopoulos A.D., "Optical Satellite Links Channel Modeling: Time Series Generator and Mitigation Techniques Evaluation", 2017 11th European Conference on Antennas and Propagation (EUCAP), Paris, 2017, pp. 50-53.

[C8] **Lyras N.K**., C. I. Kourogiorgas, Panagopoulos A. D. and Liolis K. P., "Monthly and Seasonal CFLOS Statistics for Optical GEO Feeder Links Design", accepted for publication in 9th EAI International Conference on Wireless and Satellite Systems (WiSATS), 24-25 July, 2017, Oxford, Great Britain.

[C9] **Lyras N. K.,** et.al., **"**Optical Feeder Links Study towards Future Generation MEO VHTS Systems" 35th AIAA International Communications Satellite Systems Conference, 2017**,** Trieste, Italy.

[C10] **Lyras N.K.**, Kourogiorgas C.I, Panagopoulos A. D. "Cloud Attenuation Prediction Statistics for GEO and NGSO Satellite Communication Systems Operating at Q/V Band and Above", IET Conference Proceedings, 2018, p. 830 (5 pp.)-830 (5 pp.) EUCAP 2018 London.

[C11] **Lyras N.K.**, Kourogiorgas C.I, Panagopoulos A. D., K. Liolis, Z. Sodnik "Experimental Optical Satellite Downlink Irradiance Statistics and Turbulence Conditions Estimation" IET Conference Proceedings , 2018, p. 903 (5 pp.)-903 (5 pp.), EUCAP 2018 London.

[C12] **Lyras N.K.**, Kourogiorgas C.I, Panagopoulos A. D., Liolis K. and Sodnik Z. "On Aperture Averaging Effects for Central Obscured Telescopes: Experimental Validation with ARTEMIS Experimental Downlink Measurements" ICSO 2018 Chania.

[C13] **Lyras N.K.**, Kourogiorgas C.I, Panagopoulos A. D., "Cloud Free Line of Sight Prediction for Low Earth Orbit Optical Satellite", ICSO 2018 Chania.

[C14] **Lyras N.K.**, Kourogiorgas C.I, Kapsis T. and Panagopoulos A. D., "Ground-to-Satellite Optical Link Turbulence Effects: Propagation Modeling & Transmit Diversity Performance", 13th European Conference on Antennas and Propagation (EUCAP), Krakow,2019.

[C15] **Lyras N.K.**, Kourogiorgas C.I, Kapsis T. and Panagopoulos A. D., "On Optical Satellite Communication Systems Design: CFLOS Calculation and OGS Selection", 13th European Conference on Antennas and Propagation (EUCAP), Krakow, 2019.

[C16] **Lyras N.K.,** Panagopoulos A. D. and Arapoglou P.-D. M., "Deep Space Optical Communication Links Design: Link Budget Tool for Data Rate Estimations", TTC, Darmstadt 2019.